CAPITAL UNIVERSITY OF SCIENCE AND TECHNOLOGY, ISLAMABAD

Synthesis and Biological Assessment of Structurally Modified Amantadine Derivatives against Alzheimer's Disease

by

Sobia Fazal

A thesis submitted in partial fulfillment for the degree of Master of Philosophy

in the

Faculty of Pharmacy
Department of Pharmaceutical Chemistry

2026

CERTIFICATE OF APPROVAL

Synthesis and Biological Assessment of Structurally Modified Amantadine Derivatives against Alzheimer's Disease

by

Sobia Fazal

(Registration No: MPH243017)

THESIS EXAMINING COMMITTEE

S. No.	Examiner	Name	Organization
(a)	External Examiner	Dr. Muhammad Ijaz Khan	UOSWABI, KPK
(b)	Internal Examiner	Dr. Muhammad Saalim	CUST, Islamabad

Dr. Siraj Khan
Thesis Supervisor
September, 2026

Dr. Reem
Head
Dept. of Pharmacy
September, 2026

Dr. Muzaffar Abbas
Dean
Faculty of Pharmacy
September, 2026

Author's Declaration

I, **Sobia Fazal** hereby state that my M.Phil thesis titled "**Synthesis and Biological Assessment of Structurally Modified Amantadine Derivatives against Alzheimer's Disease** " is my own work and has not been submitted previously by me for taking any degree from Capital University of Science and Technology, Islamabad or anywhere else in the country/abroad.

At any time if my statement is found to be incorrect even after my graduation, the University has the right to withdraw my M.Phil Degree.

(Sobia Fazal)

Registration No: MPH243017

Plagiarism Undertaking

I solemnly declare that research work presented in this thesis titled **"Synthesis and Biological Assessment of Structurally Modified Amantadine Derivatives against Alzheimer's Disease** " is solely my research work with no significant contribution from any other person. Small contribution/help wherever taken has been duly acknowledged and that complete thesis has been written by me.

I understand the zero tolerance policy of the HEC and Capital University of Science and Technology towards plagiarism. Therefore, I as an author of the above titled thesis declare that no portion of my thesis has been plagiarized and any material used as reference is properly referred/cited.

I undertake that if I am found guilty of any formal plagiarism in the above titled thesis even after award of M.Phil Degree, the University reserves the right to withdraw/revoke my M.Phil degree and that HEC and the University have the right to publish my name on the HEC/University website on which names of students are placed who submitted plagiarized work.

(Sobia Fazal)

Registration No: MPH243017

Acknowledgement

In the name of Allah, the most gracious and the most merciful and prayers and peace be upon Muhammad, His servant and messenger. First and foremost, I would like to acknowledge my limitless thanks to Allah Almighty and to his last Prophet Muhammad (PBUH).

I am sincerely grateful to all my respected teachers for their invaluable knowledge, guidance, and encouragement, which have played a vital role in shaping my academic and professional growth. I extend my sincere appreciation to the Dean Dr. Muzaffar Abbas, Faculty of Pharmacy, for providing a supportive academic environment and the facilities necessary to carry out this research.

I would like to express my heartfelt gratitude and profound respect to my Supervisor, Dr. Siraj Khan, for his invaluable guidance, insightful suggestions, continuous encouragement, constructive criticism, and unwavering support throughout every stage of this research. His expertise, mentorship, and dedication have been instrumental in the successful completion of this thesis.

Finally, I express my deepest gratitude to my beloved parents for their unconditional love, prayers, sacrifices, and constant encouragement throughout my academic journey. Their faith in me has been the greatest source of motivation and strength. I extend my sincere thanks to everyone who, directly or indirectly, contributed to the successful completion of this research.

(Sobia Fazal)

Abstract

Drug discovery is a multidisciplinary process that involves the identification, design, synthesis, and evaluation of new chemical entities for the treatment of human diseases. Advances in medicinal chemistry and computational techniques have accelerated the development of novel therapeutic compounds with improved pharmacological properties. Amantadine, a synthetic adamantane derivative, is an established N-methyl-D-aspartate (NMDA) receptor antagonist with proven central nervous system activity. However, its therapeutic potential against Alzheimer's disease remains limited, creating the need for structural modifications that may increase its biological activity and therapeutic profile.

The present study is designed to synthesize and evaluate novel amantadine derivatives as potential anti-Alzheimer's agents. A series of schiff base and acetylated amantadine derivatives were synthesized using established synthetic methods. The synthesized compounds were purified by recrystallization and characterized through melting point determination, solubility testing, and Fourier Transform Infrared (FTIR) spectroscopy. Molecular docking studies were performed against acetylcholinesterase (AChE), butyrylcholinesterase (BChE), and β-secretase (BACE-1) to investigate ligand-protein interactions and predict binding affinities. In addition, drug-likeness, pharmacokinetic properties, and toxicity profiles were assessed using SwissADME and ProTox-3.0.

The biological activity of the selected compound was evaluated in a scopolamine-induced mouse model of Alzheimer's disease. Cognitive performance was assessed using the Morris Water Maze and Y-maze tests. Hippocampal cyclooxygenase-2 (COX-2) levels were determined by enzyme-linked immunosorbent assay (ELISA), while histopathological examination of hippocampal tissue was carried out using hematoxylin and eosin staining to assess neuronal integrity and tissue architecture.

The synthesized derivatives demonstrated satisfactory physicochemical characteristics and favorable interactions with the selected molecular targets during molecular docking. Biological evaluation indicated that the selected derivative improved

learning and memory performance, reduced neuroinflammatory changes, and preserved hippocampal morphology compared with the disease control group. These findings suggest that structural modification of amantadine represents a promising approach for developing new therapeutic candidates against Alzheimer's disease. Further pharmacological and mechanistic investigations are warranted to establish the clinical potential of these compounds.

Keywords: Drug discovery, amantadine, Alzheimer's disease, Schiff base, molecular docking, acetylcholinesterase, β-secretase, drug-likeness, Morris Water Maze, Y-maze, COX-2.

Contents

List of Figures

List of Tables

Abbreviations

Aβ	Amyloid beta
AChE	Acetylcholinesterase
AD	Alzheimer's Disease
ADMET	Absorption, Distribution, Metabolism, Excretion and Toxicity
ALP	Alkaline phosphatase
AMPA	α-Amino-3-hydroxy-5-methyl-4-isoxazolepropionic acid
ANOVA	Analysis of Variance
APOE	Apolipoprotein E
BBB	Blood–Brain Barrier
CNS	Central Nervous System
ELISA	Enzyme-Linked Immunosorbent Assay
FTIR	Fourier Transform Infrared Spectroscopy
H&E	Hematoxylin and Eosin
MWM	Morris Water Maze
NMR	Nuclear Magnetic Resonance
PDB	Protein Data Bank

Chapter 1

Introduction

1.1 Background

1.1.1 Drug Discovery and Development

Drug discovery is a multidisciplinary process to identify a small synthetic or large biomolecule as a potential therapeutic candidate [1]. Drug discovery and drug development are fundamental processes in pharmaceutical sciences for identifying new therapeutic agents to clinical use. In the drug discovery, first biological target is identified, then through the screening of chemical or biological compounds potential hits are identified. These hits are then optimized into lead compounds with improved pharmacokinetic properties, potency and selectivity. In order to ensure the safety, efficacy and quality of these compounds, preclinical evaluation is done after which they are approved for clinical trials [2, 3]. The entire drug development process is complex, costly and time consuming, and can take a minimum of more than 10–15 years and financial investment. Despite significant advancements in technology the success of drug candidates remains low, a limited number of compounds reach the market due to the issues of toxicity, lack of therapeutic efficacy and poor bioavailability [4].

The advances in drug discovery process have accelerated the process of hit identification and facilitating the discovery of new therapeutic targets.

The process of identifying lead compounds has increased the efficiency of drug discovery and streamlined the lead identification process through different computational methods such as molecular dynamics, computer aided drug designs (CADD) [5, 6]. Recent advancements in the computational technologies have transformed the drug discovery process through emerging tools such as machine learning for predicting drug-target interactions and optimizing pharmacokinetic properties [7, 8].

The recent advancements in the biomedical technologies have broadened the field of drug discovery from its traditional focus on small molecules to include gene based therapies, biologics and novel therapeutic approaches such as antibody drug conjugates (ADCs), molecular glues etc. These approaches have shown significant results against previously undruggable targets, especially in cancer and neurodegenerative diseases [9, 10].

These approaches allow prediction of drug-target interactions, binding affinities, and pharmacokinetic properties before synthesis and biological testing, therefore reducing time and cost associated with the drug discovery [11].

Alzheimer's disease (AD) is the most common cause of dementia globally, marked by a gradual loss of memory and cognitive abilities driven by amyloid-β plaque buildup, neurofibrillary tangle formation, and degeneration of cholinergic neurons. Although this disease has been studied extensively, the drugs currently in clinical use including donepezil, rivastigmine, and memantine only manage symptoms and slow down the underlying progression [12]. This gap has pushed researchers toward designing new therapeutic candidates with stronger neuroprotective effects, making it a central goal in AD drug development. Among emerging strategies, engineering novel amantadine-based derivatives has shown considerable potential for identifying new AD therapeutics. Using techniques such as structure activity relationship (SAR) analysis alongside molecular docking simulations and pharmacological testing, researchers can systematically refine these structural modifications

to identify compounds with greater biological activity and stronger therapeutic promise.

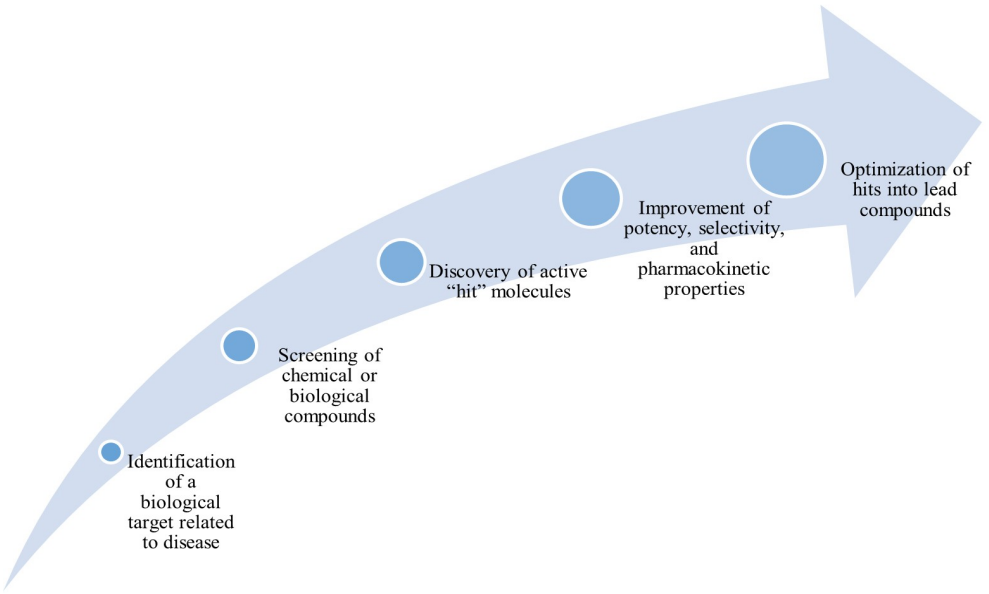

FIGURE 1.1: General Overview of Drug Discovery and Development. This schematic shows the sequential stages of early drug discovery, progressing from biological target identification through compound screening, hit discovery, and lead optimization.

1.1.2 Origin, Structure, and Physicochemical Properties

Amantadine, a synthetic compound from the adamantane class, was unexpectedly found to have its therapeutic role in Parkinson's disease. Initially approved in 1966 as a prophylactic agent against Asian Influenza, its antiparkinsonian properties were recognized when a patient with Parkinson's disease showed clinical improvement while receiving amantadine for influenza treatment.

Structurally, amantadine is described as a small synthetic tricyclic amine of the adamantane family and has a characteristic cage-like molecular framework and contributes to its pharmacological profile [13].

The broad pharmacological activity of amantadine is due to its ability to regulate the neurotransmitters involved in motor control and cognitive processes [14].

1.1.3 Chemical Structure and Physicochemical Properties of Amantadine

Amantadine is a cage-like alicyclic amine belonging to the adamantane family. The preferred chemical name of free base is commonly referred to as 1-aminoadamantane and the molecular weight of amantadine hydrochloride is reported as 151.25 g/mol. n terms of physical properties, amantadine is typically a white crystalline solid with good thermal stability due to its rigid cage structure. This distinct arrangement results in a strain-free, tetrahedral geometry, with carbon-carbon bond angles close to 109.5°. The molecule contains a primary amino group (–NH_2) attached at the bridgehead carbon at C-1 position. The molecule has high symmetry which leads to simplified spectroscopic behavior and the absence of chirality results in no optical activity. [15].

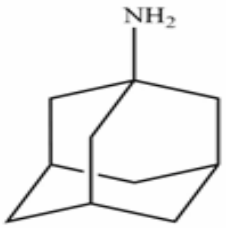

FIGURE 1.2: Chemical Structure of Amantadine. Amantadine (1-aminoadamantane) consists of a rigid, cage-like adamantane skeleton with a primary amino group at the bridgehead (C-1) position, conferring its characteristic lipophilicity and CNS penetration.

1.2 Pharmacological Profile of Amantadine

1.2.1 Mechanism of Action and Neuroprotective Effects

Amantadine exerts its pharmacological effects by modulating several neurotransmitter systems in the central nervous system. It acts primarily as a weak, non-competitive (NMDA) receptor antagonist, reducing excessive glutamatergic activity associated with neurodegeneration [14]. It also enhances dopaminergic neurotransmission by promoting dopamine release and inhibiting its reuptake, contributing to its therapeutic efficacy in neurological disorders. In addition, amantadine has been shown to promote neurogenesis, improve hippocampal plasticity

and regulate neuroinflammatory responses [16, 17].

1.2.2 Pharmacokinetic and Structural Characteristics

Amantadine readily penetrates the blood–brain barrier because of its low molecular weight and lipophilic adamantane structure. Despite being predominantly ionized at physiological pH, it accumulates effectively in the brain, indicating the involvement of both passive diffusion and active transport mechanisms. The rigid and symmetrical adamantane scaffold facilitates stable interactions with ion channels, enabling amantadine to block both the influenza A viral M2 proton channel and NMDA receptor-associated ion channels [18].

1.2.3 Dopaminergic and Neurogenic Effects

In addition to its effects on glutamatergic transmission, amantadine also modulates dopaminergic signaling in the brain. Studies have demonstrated that amantadine enhances dopamine release and inhibits its reuptake thereby increasing dopaminergic neurotransmission in the striatum. This dopaminergic modulation contributes to its therapeutic effects in Parkinson's disease and other neurological conditions characterized by impaired dopamine signaling. Furthermore, experimental studies have indicated that amantadine may stimulate neurogenesis and influence hippocampal neuronal plasticity, which might have potential benefits for cognitive function and mood regulation [16].

1.2.4 Blood–Brain Barrier Penetration and Pharmacokinetic Characteristics

The rigid hydrophobic amantadine structure facilitates the permeation across the brain, this process is not facilitated only by passive diffusion but also by an active transport system.

Although amantadine is a low molecular weight compound with moderate lipophilicity, however due to its weakly basic primary amine it remains in a positively ionized state under physiological state.

Despite this high degree of ionization, amantadine accumulates efficiently in the brain, indicating that passive membrane permeation alone cannot fully explain its CNS distribution [18].

1.2.5 Structural Rigidity and Ion Channel Interaction

The important physicochemical characteristic of amantadine includes is its structural symmetry and steric bulk.

The adamantane cage possesses a highly symmetrical three-dimensional structure that minimizes conformational flexibility.

This rigidity allows the molecule to maintain a stable orientation when interacting with protein targets such as ion channels or receptors.

As a result, the structural features of amantadine allows it to block ion channels, including the viral M2 proton channel of influenza A virus as well as NMDA receptor-associated channels in neuronal membranes [14].

1.2.6 Structure Activity Relationship of Amantadine

Amantadine contains a primary amino group ($–NH_2$) attached to the bridgehead carbon (C-1 position). This functional group provides basic character to the molecule and allows it to form salts such as amantadine hydrochloride, which is the commonly used pharmaceutical form. The coexistence of a hydrophobic adamantane core and a polar amino group makes amantadine an amphipathic compound which facilitates it to interact with both lipid membranes and aqueous biological environments [15]. The hydrophobic nature of the adamantane cage facilitates interaction with hydrophobic regions NMDA receptor channel pore. This property

allows amino-adamantane derivatives to act as channel blockers and preventing excessive calcium influx associated with excitotoxic neuronal damage [19].

The chemical reactivity of amantadine is associated with its primary amino group, which serves as the key site for structural modification. This amino group participates in various reactions such as Schiff base formation with aldehydes or ketones, acylation forming amide derivatives, and alkylation producing secondary or tertiary amines, all of which can affect pharmacokinetic and biological properties.

The most common modifications are to the amino group, while limited reactions like halogenation and nitration of the adamantane core have also been studied. However, due to the inherent stability of the adamantane cage, most derivatization occurs at the amino group rather than the hydrocarbon framework [15].

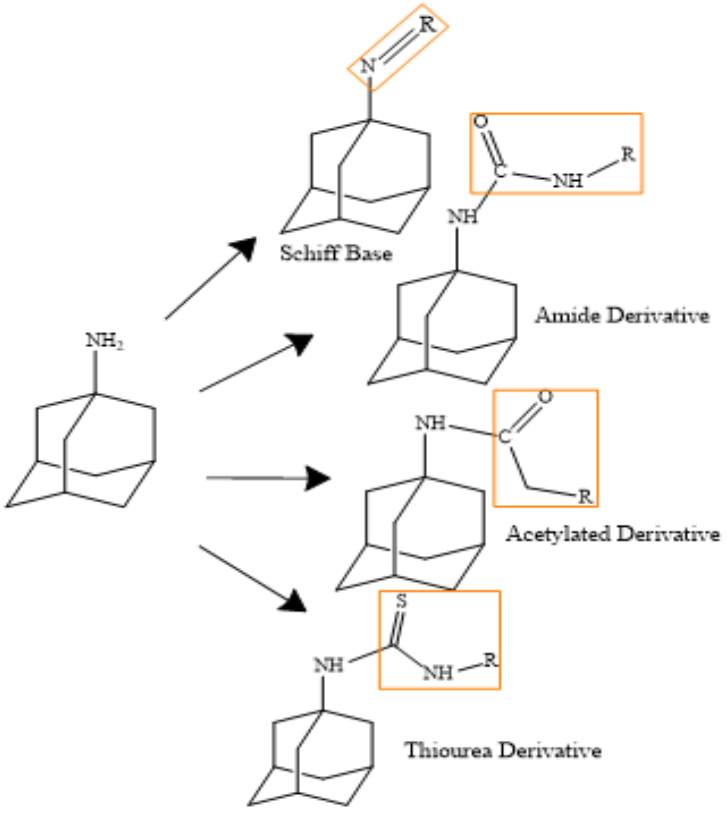

FIGURE 1.3: Pictorial representation of SAR of Amantadine. Structure–activity relationship of amantadine, highlighting key functional groups and modifications.

The modification of amine functionality through conjugation with other pharmacophores ae the important features of SAR. Various amantadine derivatives have been synthesized by attaching aromatic, benzyl, or phenylethyl groups to the amine moiety [20]. Also, hybrid molecules containing thiourea or amide linkages have shown improved inhibitory activity against different enzyme targets. These findings indicate that introducing additional functional groups can improve receptor interactions, increase potency and expand therapeutic applications of amantadine derivatives [21].

1.3 Overview and Clinical Features of Alzheimer's Disease

AD is a chronic, progressive neurodegenerative disorder and is includes gradual decline of cognitive function and neuronal damage in hippocampus, entorhinal cortex, and cerebral cortex [22–24]. The principal neuropathological features of AD include amyloid-β plaque accumulation, neurofibrillary tangles and neuroinflammation which leads to neuronal death [25, 26]. These pathological alterations begin many years before the appearance of clinical symptoms, suggesting a prolonged preclinical stage during which molecular and cellular changes progressively accumulate [24, 27].

Clinically, AD is characterized by widespread neurodegeneration and synaptic dysfunction within the hippocampus and cerebral cortex [28]. As the disease progresses, there is decline in executive functioning, language, attention, and visuospatial processing, ultimately resulting in widespread cognitive dysfunction and dementia. Behavioral and neuropsychiatric symptoms include depression, anxiety, apathy, agitation, hallucinations, and psychotic symptoms, frequently develop during disease progression which contributes to functional impairment. In the later stages of AD patients develop abnormalities in gait, balance, sleep patterns and mood in the advanced stages of disease which leads to decline in cognitive functional and quality of life. [29].

1.3.1 Epidemiology and Global Disease Burden

AD constitutes approximately 60–70% of all dementia cases worldwide [30]. The Global Disease Burden (GBD) study reported that in 2019, an estimated 57.4 million people have dementia, and this number can increase to rise to 152.8 million by 2050, which indicates the rapidly growing global burden of neurodegenerative disorders [31].

Epidemiological analyses indicate that the prevalence of AD increases significantly after the age of 65 years and doubles approximately every five years thereafter [23]. In the epidemiology sex differences have also been reported, with women showing a higher prevalence than men, which might be due to longer life expectancy [23]. In addition, geographical variations in prevalence have been observed, with higher rates reported in high-income regions such as North America and Western Europe, while the fastest growth in disease burden is expected in low- and middle-income countries due to population aging and demographic transitions [31].

1.3.2 Etiology and Risk Factors

AD has a multifactorial etiology involving genetic, environmental, and age-related factors that collectively contribute to progressive neurodegeneration [32].

The abnormal accumulation of amyloid-β (Aβ) peptides and the formation of hyperphosphorylated tau neurofibrillary tangles are considered the principal pathological events responsible for synaptic dysfunction and neuronal loss [33, 34].

Chronic neuroinflammation, mediated by activated microglia and astrocytes, along with oxidative stress and mitochondrial dysfunction, further accelerates disease progression [35]. Lifestyle and environmental factors also significantly impact the disease development while cognitive stimulation and healthy lifestyle behaviors may help delay disease onset [36, 37].

Additionally the recent studies indicate that chronic stress, traumatic brain injury, and neuroinflammation may contribute to disease pathogenesis by promoting amyloid deposition and neuronal damage [38].

1.3.3 Molecular Pathology of Alzheimer's Disease

1.3.3.1 Amyloid-β and Tau Pathology

AD is characterized by two major pathological features that includes deposition of Aβ plaques and accumulation of neurofibrillary tangles (NFTs). These abnormalities affect neuronal communication, synaptic function, and contribute to progressive neuronal loss [39].

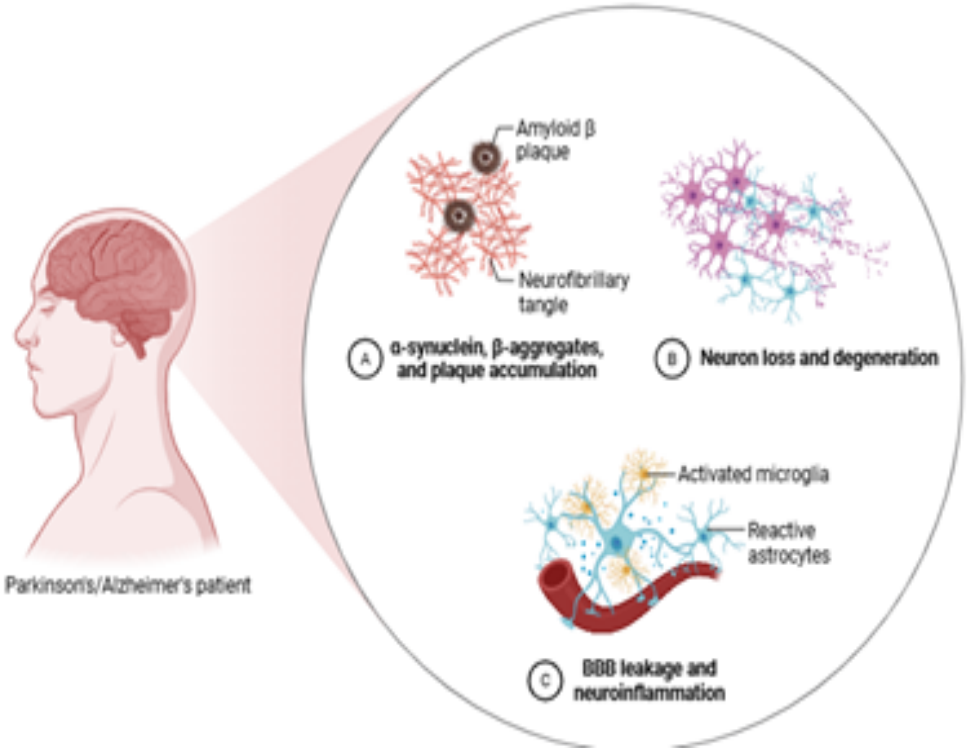

FIGURE 1.4: Pathogenesis of Alzheimer's disease, illustrating the interlinked hallmarks driving neurodegeneration: (A) accumulation of amyloid-β plaques, neurofibrillary tangles, and -synuclein/β-aggregates; (B) progressive neuronal loss and degeneration; and (C) BBB leakage accompanied by neuroinflammation, marked by activated microglia

According to the amyloid cascade hypothesis, excessive production or impaired clearance of Aβ promotes the formation of toxic oligomers and plaques, triggering oxidative stress, mitochondrial dysfunction, neuroinflammation, and neuronal death [40, 41]. Also, the abnormal hyperphosphorylation of tau destabilizes microtubules and leads to the formation of neurofibrillary tangles, ultimately resulting in synaptic dysfunction, cognitive decline, and brain atrophy [28, 42, 43].

1.3.3.2 Neuroinflammation and Immune Dysregulation

Neuroinflammation is another important mechanism involved in the progression of Alzheimer's disease. Under normal conditions, microglia maintain brain homeostasis by clearing amyloid-β and tau aggregates.

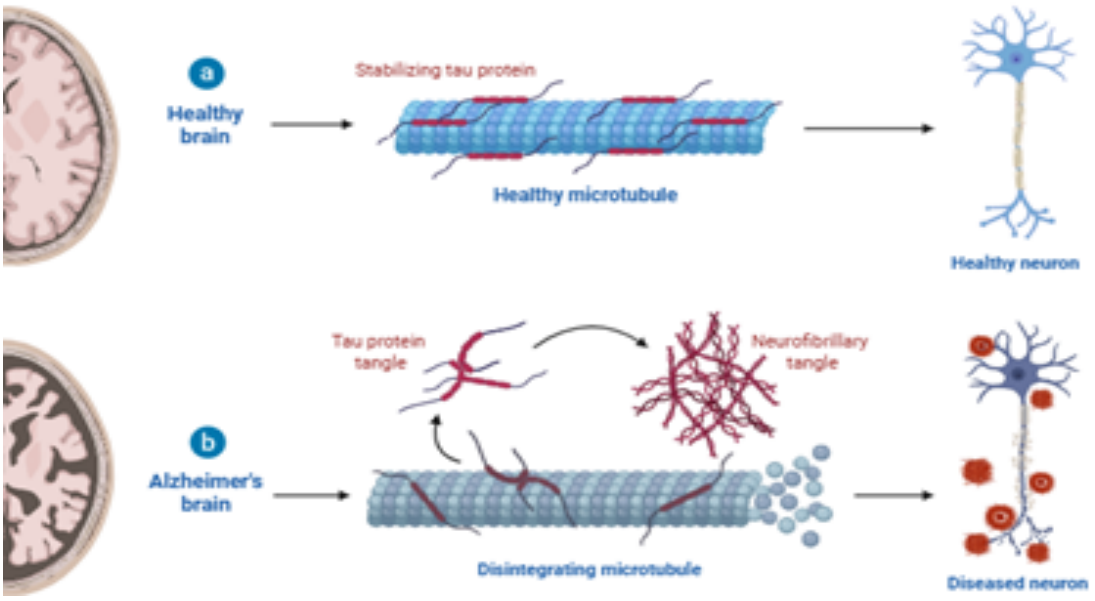

FIGURE 1.5: Pathogenesis of Alzheimer's disease at the microtubule level, contrasting (a) a healthy brain, where tau protein stabilizes microtubules to maintain normal microtubule structure and a healthy neuron, with (b) an Alzheimer's brain, where tau protein detaches and hyperphosphorylates into tau tangles, causing microtubule disintegration and subsequent aggregation into neurofibrillary tangles, ultimately leading to neuronal degeneration and disease.

However, persistent activation of microglia results in excessive release of pro-inflammatory mediators, promoting neuronal damage and cognitive decline [44].

Increasing evidence suggests that neuroinflammation interacts closely with amyloid and tau pathology, forming an interconnected pathogenic network that accelerates disease progression.

Consequently, current research considers Alzheimer's disease a multifactorial disorder involving multiple overlapping molecular pathways rather than solely an amyloid-driven disease [39].

1.3.4 Neurotransmitter Dysregulation and Synaptic Degeneration

1.3.4.1 Cholinergic Dysfunction

Neurotransmitter dysregulation and synaptic degeneration are key pathological features of AD that contribute significantly to cognitive decline. Degeneration of basal forebrain cholinergic neurons reduces acetylcholine synthesis and cholinergic neurotransmission, leading to impaired learning, memory, and synaptic plasticity, while amyloid-β further disrupts cholinergic function and acetylcholinesterase activity [45, 46]. Synaptic dysfunction occurs early in AD, preceding extensive neuronal loss, and is associated with alterations in cholinergic, glutamatergic, and GABAergic signaling pathways that are essential for neuronal communication and cognitive function [47]. Excessive glutamate accumulation causes overactivation of NMDA receptors, resulting in calcium dysregulation, oxidative stress, mitochondrial dysfunction, excitotoxicity, and neuronal apoptosis, whereas amyloid-β-mediated disruption of glutamate transport further amplifies these pathological processes [45, 47]. In addition, abnormalities in AMPA receptor expression and function impair synaptic plasticity and excitatory neurotransmission, contributing to reduced neuronal connectivity, memory impairment, and progressive neurodegeneration [48]. Although currently available cholinesterase inhibitors, NMDA receptor antagonists, and recently developed anti-amyloid monoclonal antibodies provide symptomatic or modest disease-modifying benefits, their limited efficacy

is the limiting factor needing strategies targeting multiple mechanisms involved in neurotransmitter dysfunction and synaptic degeneration [39, 41].

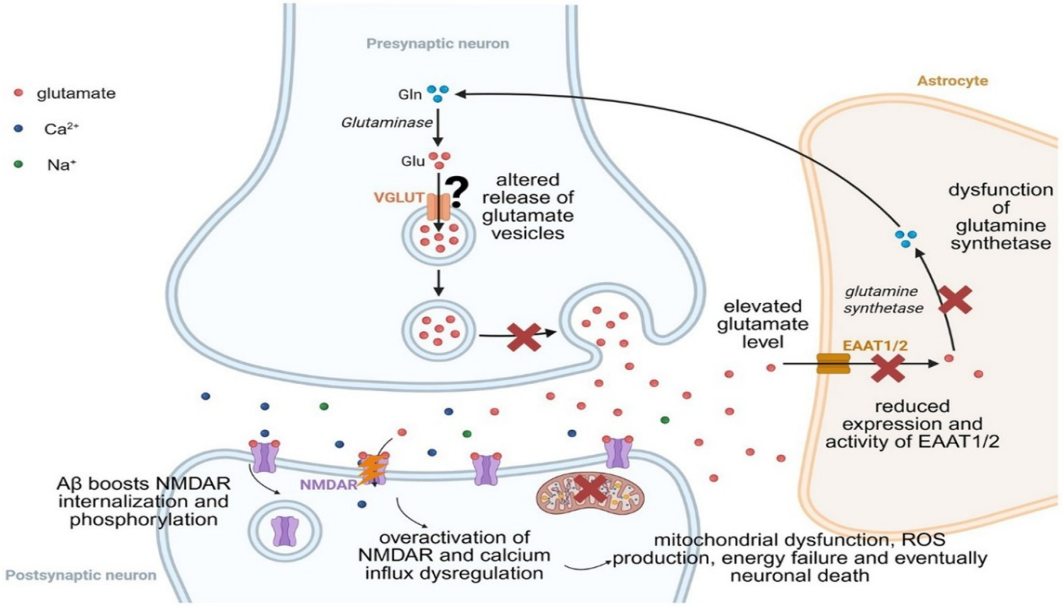

FIGURE 1.6: Mechanism of glutamate-induced neurotoxicity in Alzheimer's disease. Elevated synaptic glutamate, resulting from dysregulated presynaptic release and impaired astrocytic reuptake, over activates postsynaptic NMDA receptors. This triggers calcium influx dysregulation, mitochondrial dysfunction, and eventual neuronal death [Figure adopted by Keyi Zhang et al. (2025)] [49].

1.3.4.2 Therapeutic Strategies for Alzheimer's Disease

The therapeutic options for AD are limited and mainly include cholinesterase inhibitors such as donepezil, rivastigmine, NMDA receptor antagonist including memantine amyloid targeting monoclonal therapies such as aducanumab and BACE inhibitors [50]. Pharmacological agents that modulate NMDA receptor activity can reduce excitotoxic neuronal damage while maintaining normal synaptic signaling required for cognitive function. Memantine is used for moderate to severe AD, it selectively blocks NMDA receptor activation while allowing physiological synaptic transmission to continue. Although this drug provides symptomatic improvement in some patients, its therapeutic benefits remain limited and do not completely stop disease progression. Therefore, there is a growing need to identify additional compounds which can modulate glutamatergic neurotransmission and providing enhanced neuroprotective effects [51].

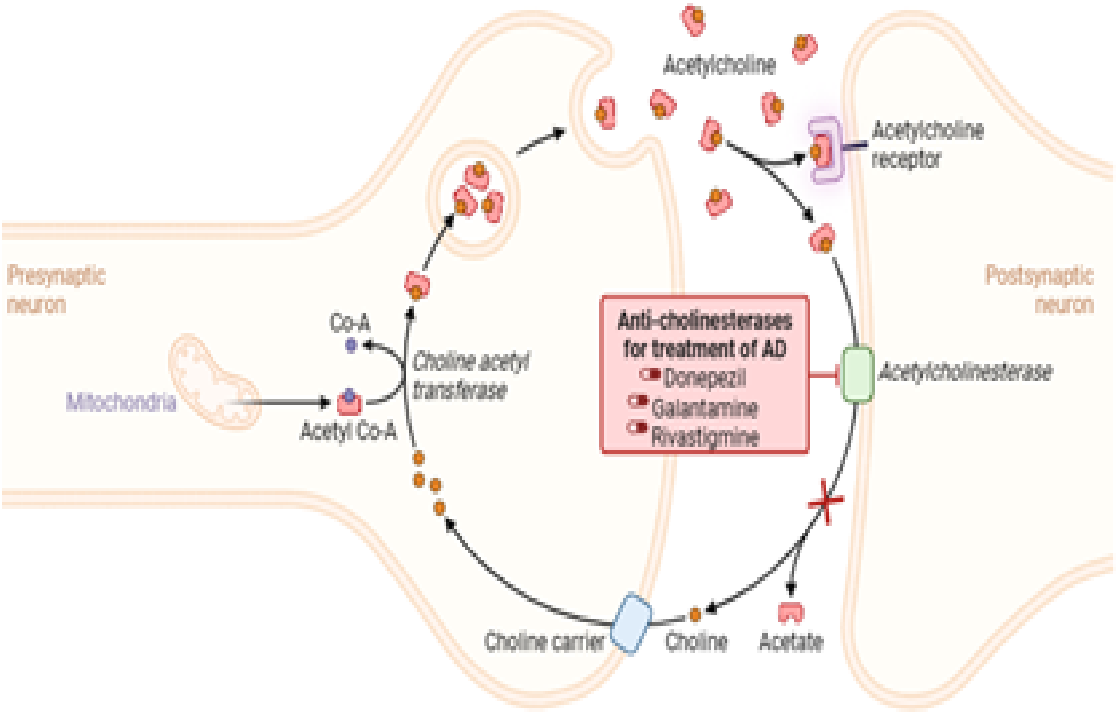

FIGURE 1.7: Mechanism of action of anti-cholinesterases in Alzheimer's disease. Acetylcholine is synthesized presynaptically, released into the synapse, and normally degraded by acetylcholinesterase to terminate signaling. Anti-cholinesterase drugs (donepezil, galantamine, rivastigmine) inhibit this enzyme, prolonging cholinergic neurotransmission.

1.4 Rationale of Study

The rationale of the study is to modify the amantadine by synthesizing its derivatives that might be good lead candidate.

1.5 Problem Statement

The therapeutic potential of amantadine in Alzheimer's disease remains largely unexplored. This gap highlights the need to design and evaluate novel amantadine derivatives as a potential lead compounds for Alzheimer's disease.

1.6 Aim and Objectives

1.6.1 Aim

The aim of the study is to design and synthesize the pharmacologically active amantadine derivatives.

1.6.2 Objectives

i. To check the ADMET profile of derivatives by different databases.

ii. To perform molecular docking for evaluating drug binding interactions.

iii. To synthesize new amantadine derivatives.

iv. To identify, purify and characterize the amantadine derivative by different spectroscopic techniques.

v. To evaluate their anti-Alzheimer's, potential.

Chapter 2

Literature Review

2.1 Synthesis of Schiff Base Derivatives of Amantadine

Schiff bases are an important class of organic compounds that were first reported by Hugo Schiff, an Italian-German chemist in 1864. They are formed through the reaction between primary amine with an aldehyde or ketone under suitable reaction conditions [52]. Schiff bases contain a characteristic azomethine or imine (–C=N–) linkage, which is responsible for their chemical and biological properties.

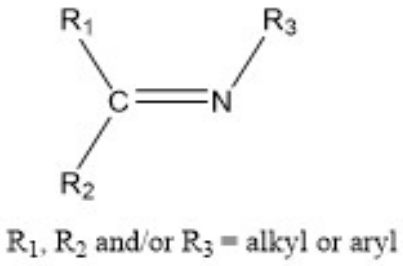

FIGURE 2.1: Figure adopted by Cleiton M. da Silva et al. (2011)] [52] showing the characteristic C=N (imine) linkage, where R and R are substituents derived from the parent aldehyde/ketone, and R is the substituent from the primary amine; R , R , and/or R may be alkyl or aryl groups.

Schiff base derivatives have been studied for their pharmacological activities and their potential applications in drug discovery [53]. A summary of selected studies relevant to the Schiff's bases is presented below.

Jin et al. (2013) synthesized a Schiff base ligand derived from amantadine by reacting adamantan-1-amine with 4-methoxysalicylaldehyde through a condensation reaction. In this synthetic approach, the primary amine group of amantadine reacted with the aldehyde group of the salicylaldehyde derivative under reflux conditions to form an azomethine linkage (–C=N–) Schiff base ligand. The synthesized ligand was used to prepare zinc (II) complexes which were further characterized [54].

Similarly, Jin et al. (2019) reported the ligands from the condensation of amantadine with substituted salicylaldehydes i.e., 3,5-dihalosalicylaldehydes. The synthesis was carried out using equimolar quantities of amantadine and the aldehyde derivative were reacted in an alcoholic solvent under reflux conditions. The resulting Schiff base ligands were isolated and further used to synthesize copper(II) coordination complexes. [55].

Recent work by Majumdar et al. (2023) also explored the synthesis of adamantan-1-amine-based derivatives including Schiff base type compounds. In this study, adamantan-1-amine was reacted with suitable aldehyde precursors to produce imine derivatives through condensation reactions. The synthesis involved mixing the amine and aldehyde components in a suitable solvent system followed by reflux to facilitate imine formation. The study further used density functional theory (DFT) calculations to investigate electronic properties of the compounds [56].

Ajaz et al., 2023 synthesized a novel amantadine-based Schiff base ligand, formed by condensation of amantadine with 3-allyl-2-hydroxybenzaldehyde. The synthesized Schiff base ligand was further utilized as a chelating ligand for the preparation of several transition-metal complexes including metal complexes. The azomethine group of the Schiff base played a key role in coordination with metal ions, leading to the formation of stable complexes with different geometrical arrangements [57].

Channar et al., 2019 reported the synthesis oof amantadine-derived phenolic azo Schiff bases. In their study, the amantadine moiety was incorporated into phenolic azo aldehyde derivatives through the formation of an azomethine linkage, resulting in hybrid molecules containing both azo and Schiff base functional groups. The author further reported that the synthesized Schiff base derivatives showed significant carbonic anhydrase II inhibitory activity [58].

Kostić and Leovac et al. 2024, presented a comprehensive overview of adamantane derived Schiff bases and their metal complexes. Their analysis of structural data from the Cambridge Structural Database revealed 224 reported structures of Schiff bases containing the adamantane moiety, among which 131 were metal complexes formed through coordination of these Schiff bases with various metal ions.

The authors further reported that these adamantane-derived ligands form complexes with numerous transition metals including Cu (II), Ti (IV), Zn (II).

Additionally, they also reported that adamantane-containing Schiff bases are also used in Schiff base condensation reactions between adamantane derivatives and nitrogen containing compounds [59].

Yasmeen et al. 2024 synthesized a series of novel amantadine Schiff base derivatives. In the study, amantadine derivatives were formed with different aromatic aldehydes and ketones and the synthesized compounds were then characterized using spectroscopic techniques to confirm the formation of Schiff base structures [60].

Ajaz et al. 2023 synthesized a novel amantadine based Schiff base ligand followed by the preparation of its transition metal complexes. In this study, the synthesized Schiff base acted as a coordinating ligand capable of binding different metal ions such as Co (II), Zn (II) etc. The study indicated that the introduction of Schiff base moiety not only modifies the chemical structure of amantadine but also allows the formation of biologically active metal complexes with improved pharmacological potential [61]. In another study Yang et al. 2014 presented a detailed study on the synthesis of amantadine-derived Schiff bases. In this study,

the authors synthesized two Schiff base ligands by reacting amantadine with halogenated salicylaldehydes. The primary amine group of amantadine reacted with the aldehyde group of the substituted salicylaldehydes to form imine (–C=N–) containing ligands. Their antibacterial activity of was evaluated against E. coli and B. Subtilis. This study showed that Schiff base formation provides an efficient synthetic strategy for modifying the amantadine scaffold and generating ligands capable of forming biologically active metal complexes [62].

Wang et al. 2011 synthesized three amantadine Schiff base derivatives; amantadine-salicylaldehyde, amantadine-5-chlorosalicylaldehyde, and amantadine-o-vanillin, by refluxing amantadine with the corresponding aldehydes in ethanol. The synthesized compounds were characterized and this study proposed a simple route for preparing amantadine Schiff base derivatives from salicylaldehyde type precursors [63].

Jin et al. 2017 synthesized Schiff base ligands derived from amantadine and 5-halogenated salicylaldehydes, specifically 5-chloro- and 5-bromosalicylaldehyde derivatives. These ligands were synthesized by refluxing adamantaneamine with the respective halogenated salicylaldehyde in anhydrous alcohol for 1 h. In the same study, these ligands were further reacted with copper (II) chloride dihydrate in methanol after deprotonation with NaOH to form copper (II) complexes. The findings showed that halogen substituted amantadine Schiff bases can also serve as suitable ligands for metal complex formation [64].

In another study, Jin et al. 2019 synthesized Schiff bases using salicylaldehyde or 4-methoxysalicylaldehyde.

The ligands were prepared by refluxing amantadine hydrochloride or rimantadine hydrochloride with KOH and the appropriate aldehyde in anhydrous ethanol for 1 h, then metal complex with manganese (II) was formed.

This study showed that the condensation strategy is adaptable to different adamantane based amines and substituted salicylaldehydes, allowing the synthesis of structurally varied bulky Schiff bases [65].

TABLE 2.1: Amantadine- aldehyde Schiff Bases and their bioactivities

Compound	Aldehyde	Type of complex	Bioactivities Evaluated	Ref
Amantadine	4-Methoxysalicylaldehyde	Schiff base ligand + Zn (II) complexes	Ligand was synthesized by condensation of adamantan-1-amine with 4-methoxysalicylaldehyde and later used for Zn (II) complex formation; structural characterization confirmed Schiff base formation and coordination behavior	[54]
Amantadine	3,5-Dihalosalicylaldehydes	Schiff base ligands + Cu (II) complexes	Ligands were synthesized by condensation with 3,5-dihalosalicylaldehydes and further coordinated with Cu (II); complexes were structurally characterized and their electrochemical properties were investigated	[55]
Amantadine	Phenolic azo aldehydes	Schiff base ligands	Compounds were reported as potent selective carbonic anhydrase II inhibitors and were evaluated by drug-likeness and binding analysis	[56]
Amantadine	Various aldehydes/ketones	Schiff base ligands + metal complexes	Review highlighted wide structural diversity, metal coordination behavior, and applications in coordination chemistry and advanced materials	[59]

Table 2.1 continued from previous page

Compound	Aldehyde	Type of complex	Bioactivities Evaluated	Ref
Amantadine	Various aromatic aldehydes and ketones	Schiff base ligands	Synthesized derivatives were evaluated for molecular docking, derivatization, characterization, and biological assays of amantadine analogs	[60]
Amantadine	5-Chlorosalicylaldehyde	Schiff base ligand + Cu (II) complex	Ligand synthesized from amantadine and used for Cu (II) complex formation; complexes were further studied electrochemically	[64]
Amantadine	5-Bromosalicylaldehyde	Schiff base ligand + Cu (II) complex	Ligand synthesized from amantadine and used for Cu (II) complex formation; complexes were further studied electrochemically	[64]
Amantadine	Salicylaldehyde	Schiff base ligand + Mn (II) complex	Amantadine-derived bulky Schiff base was used for Mn (II) complex synthesis; complexes showed magnetic properties	[65]
Rimantadine	4-Methoxysalicylaldehyde	Schiff base ligand + Mn (II) complex	Rimantadine-derived bulky Schiff base was used for Mn (II) complex synthesis; complexes showed magnetic properties	[65]

2.2 Synthesis of Acetylated Derivatives of Amantadine

Modification of primary amines through acylation reactions is an important strategy in medicinal chemistry for generating biologically active derivatives. Among these reactions, chloroacetylation using chloroacetyl chloride is used widely because it produces intermediates that can undergo further functionalization and widely used in the synthesis. Below are some studies adopting chloroacetylation for the synthesis of derivatives.

Balaji and Dalal et. al 2018 developed a method for the synthesis of chloroacetamide derivatives through the reaction of amines with acid chlorides under neutral conditions. In their study, primary amines were reacted with different acid chlorides to form the amides with high yields. Their protocol utilized phosphate buffer as the reaction medium and allowed rapid N-chloroacetylation within approximately 20 minutes. The findings demonstrated that chloroacetyl chloride can effectively convert amino compounds to produce chloroacetamides under metal-free conditions. They also proposed that conventional Schotten-Baumann conditions for chloroacetylation often require strong bases and longer reaction times, whereas their developed method achieved selective N-chloroacetylation efficiently in aqueous medium [66].

Liu et al. 2013 synthesized several novel amantadine derivatives using chloroacetylation as a key step. In their study, chloroacetyl chloride was first generated from chloroacetic acid and oxalyl chloride. The produced chloroacetyl chloride was then reacted with amantadine at low temperature (0–3 °C) to yield N-adamantyl-2-chloroacetamide as an intermediate. This chloroacetamide intermediate served as a key precursor for synthesizing additional derivatives through substitution reactions with phenolic compounds, producing several N-adamantyl-2-phenoxyacetamide derivatives. The synthesized derivatives were evaluated for antiviral activity against influenza A/H3N2 virus [67].

Onajole et al. synthesized a series of adamantane derivatives by modifying the amantadine scaffold through acylation reactions. In their study, the free amine of amantadine was reacted with chloroacetyl chloride to produce the corresponding chloroacetamide intermediate. This intermediate served as a key synthetic precursor for further functionalization. The resulting chloroacetylated amantadine was subsequently reacted with geranyl amine to yield new diamine derivatives. The synthesized derivatives showed improved antifungal and antibacterial properties compared with some reference compounds, demonstrating that modification of the amantadine amino group through chloroacetylation can be an effective strategy for generating biologically active derivatives [68].

Meng et al. (2025) formed amino acetamide derivatives through the acylation of amines using chloroacetyl chloride as the key acetylating reagent. In their study, various primary amines were first reacted with chloroacetyl chloride in the presence of potassium carbonate in dichloromethane to produce chloroacetamide intermediates in good yields. These intermediates were subsequently subjected to nucleophilic substitution with isoquinoline to generate a series of isoquinolinium-based acetamide derivatives. The synthetic strategy indicated that chloroacetyl chloride act as an efficient reagent for introducing the chloroacetamide moiety in amine-containing scaffolds. The synthesized compounds were later evaluated for biological activity, where several derivatives showed notable antifungal activity and acetylcholinesterase inhibitory potential [69].

Chapter 3

Materials and Methods

The materials used in this research consisted of analytical grade laboratory chemicals, organic solvents, analytical reagents for synthesis, purification, and characterization of the compounds. Glassware, laboratory instruments, and analytical equipment were thoroughly cleaned and prepared before use to minimize contamination.

Reagents were stored according to the manufacturers' recommendations and used under appropriate laboratory conditions throughout the study.

3.1 Materials

Analytical grade reagents and solvents were used throughout the study. No additional purification or pretreatment of the chemicals was carried out before their use.

3.1.1 Chemicals

The chemicals used in this study were 2-aminobenzothiazole, 3,4,5-trimethoxybenzaldehyde, 3-hydroxybenzaldehyde, 4-dimethylaminobenzaldehyde,

4-hydroxybenzaldehyde, amantadine, chloroform, ethanol, ethyl acetate, sulfuric acid, methanol, petroleum ether, were obtained from Sigma Aldrich while sulfadimidine, sulfamethoxypyridazine were gifted by a pharmaceutical industry.

3.2 Apparatus and Equipment

The experimental work used the analytical instruments available in the laboratory, glass wares including round bottom flasks, beakers, conical flasks, pipettes, petri dishes and test tubes were used during the synthesis and purification procedures. Analytical weighing balance was used for accurate measurement of chemicals, while magnetic stirrers and hot plates were used to facilitate mixing and heating of reaction mixtures. The Gallenkamp apparatus was used to determine melting point of synthesized compounds. The completion of the reaction was confirmed by TLC. The derivatives were characterized using Fourier Transform Infrared (FTIR) spectroscopy. Molecular docking studies were carried out using PyRx software, and the ligand–protein interactions were analyzed and visualized using Discovery Studio Visualizer.

3.3 Methods

3.3.1 General Reaction for the Synthesis of Schiff Bases

The Schiff base was synthesized by reacting amantadine with equimolar amounts of respective aldehyde (4-hydroxybenzaldehyde, 3-hydroxybenzaldehyde, vanillin, 3,4,5-trimethoxy benzaldehyde, 4-dimethylamino benzaldehyde) and amantadine. The 1 mmol (151.25 mg) amantadine was mixed in 15 ml of ethanol in a dry, clean round-bottom flask. It was then allowed to stir until dissolved completely, then respective aldehyde was added and further allowed to mix at the reflux assembly and was subjected to heat at 60 $^{\circ}$C. After adding 1-2 drops of sulfuric acid, the

mixture was agitated for three to four hours at room temperature. White precipitates were formed which indicated the completion of reaction, confirmed by TLC using 1:1 solvent mixture of ethyl acetate and petroleum ether. After that the precipitates were collected and dried. The product was air dried and stored for further analysis [59, 60].

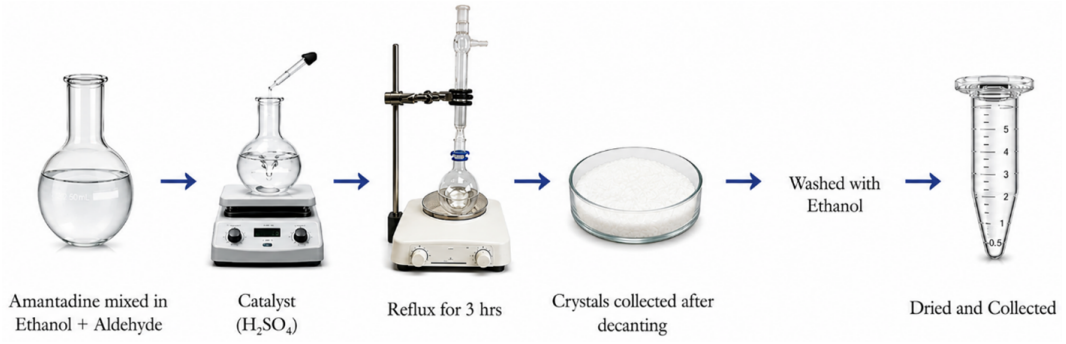

FIGURE 3.1: Schematic representation of Schiff base formation from amantadine and an aldehyde in ethanol using H_2SO_4 as an acid catalyst, followed by reflux for 3 hours. The resulting crystals were collected after decanting, washed with ethanol, dried, and collected as the final Schiff base derivative.

3.4 Synthesis Scheme for Schiff's Bases

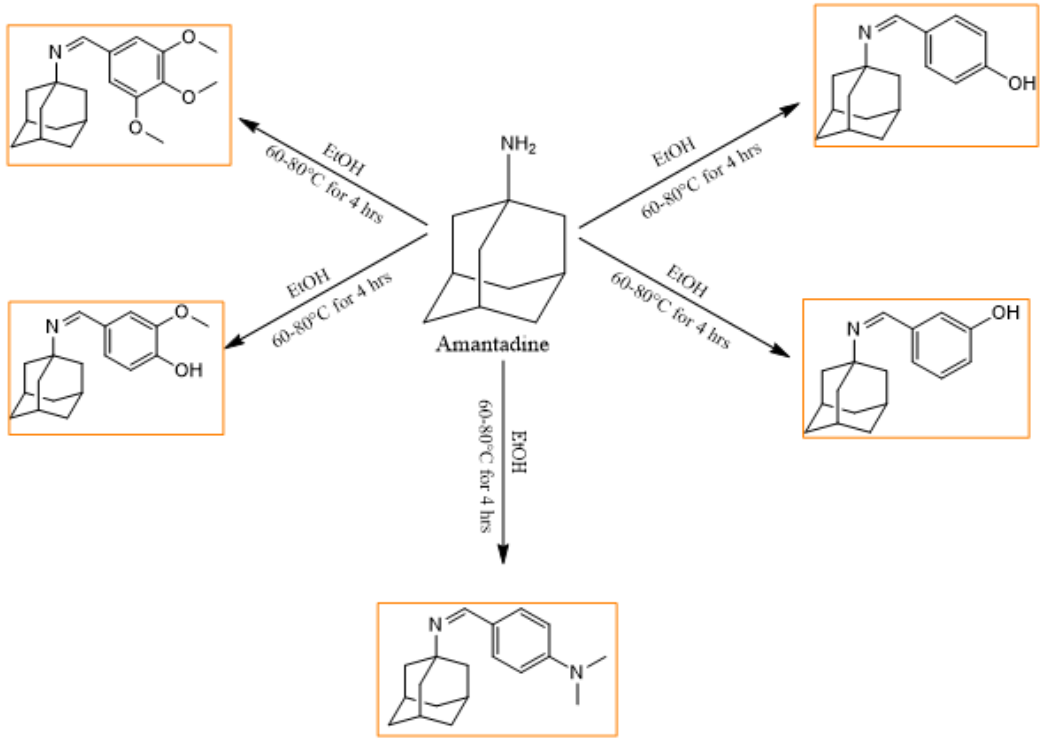

FIGURE 3.2: Synthesis scheme of schiff bases (1a, 2a, 4a, 5a, and 6a) obtained by condensation of amantadine with the corresponding aldehydes in ethanol under reflux conditions.

3.5 General Reaction for the Synthesis of Acetylated Amantadine Derivatives

Following the reported procedure, the acetylated derivative was prepared in two steps.

In the first step, amantadine (1 mmol, 151.25 mg) was dissolved in 3 mL of dichloromethane (DCM), followed by the addition of one equivalent of triethylamine (TEA) (1 mmol, 139 µL) to the resulting solution.

With the flask held in an ice bath, 2-chloroacetyl chloride (1.2 mmol, 95.6 µL) was introduced dropwise over one hour, after which stirring was continued overnight at room temperature. Reaction progress was tracked by TLC, using petroleum ether and acetone in a 0.3:0.7 ratio as the mobile phase.

Once the reaction reached completion, the mixture was concentrated, water was introduced, and the product was partitioned into the organic phase through three successive extractions with CH_2Cl_2.

The combined organic layer was then separated from the aqueous layer and left to air-dry, yielding a concentrated film of chloro-acetylated amantadine [70].

For the second step, the chloro-acetylated amantadine obtained above (1 mmol, 227.73 mg) was redissolved in 5 mL of CH_2Cl_2.

TEA (1.5 mmol, 209.1 µL) was added first, followed by potassium iodide (KI) (1.2 mmol, 199.2 mg). The mixture was stirred briefly before the corresponding amine (1 mmol) was introduced, and stirring was continued for 32 hours.

Reaction completion was again confirmed by TLC, after which the organic and aqueous layers were separated, and the organic phase was air-dried to yield the concentrated final product.

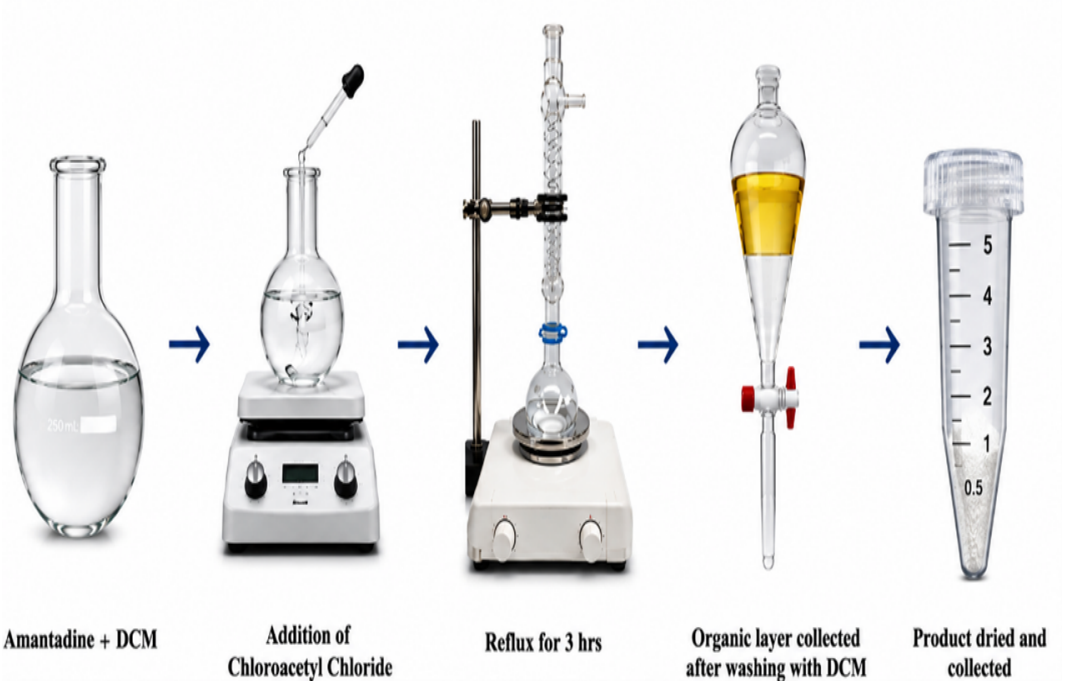

FIGURE 3.3: Schematic Representation of Acetylated Derivatives Formation Step 1 Amantadine in DCM was reacted with chloroacetyl chloride and refluxed for 3 hours; the organic layer was then washed, separated, and dried to yield the purified intermediate product.

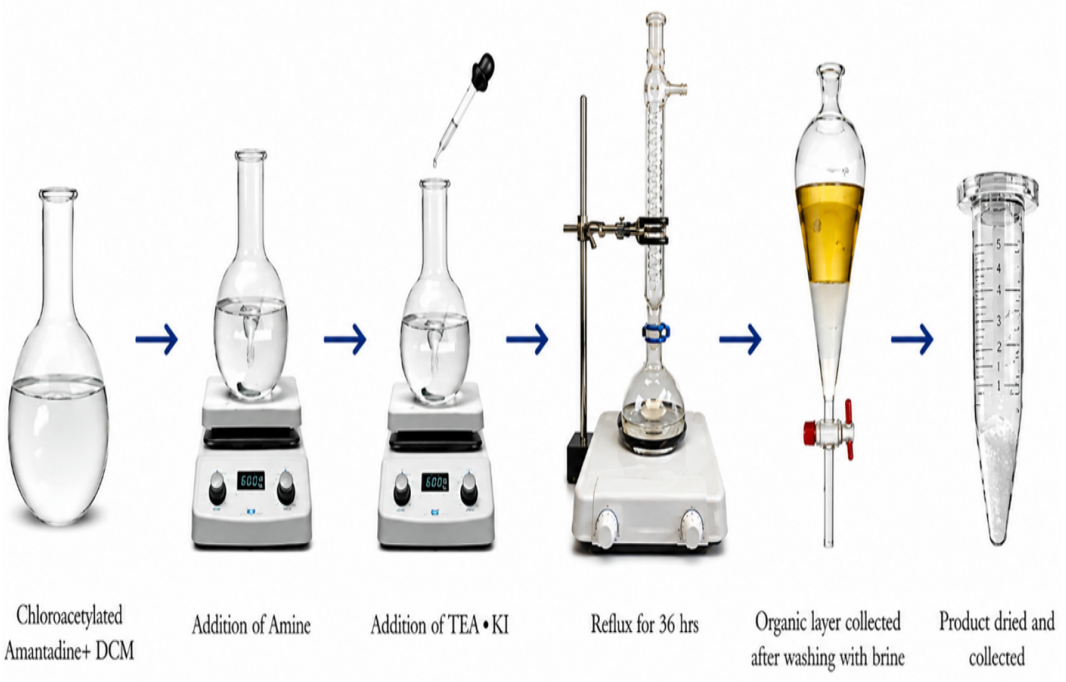

FIGURE 3.4: Schematic Representation of Acetylated Derivatives Formation Step 2. The chloroacetylated amantadine intermediate in DCM was treated with the appropriate amine, along with TEA and KI, and refluxed for 36 hours to facilitate nucleophilic substitution. The organic layer was then washed with brine, separated, and dried to afford the final acetylated derivative product.

3.6 Synthesis Scheme for Acetylated Amantadine Derivatives

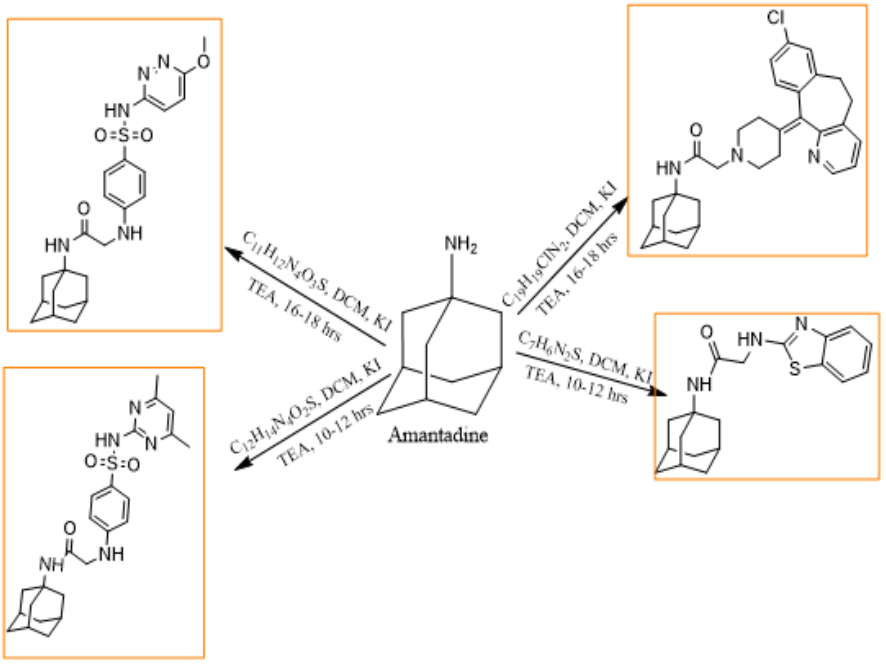

FIGURE 3.5: Synthesis Scheme of Acetylated Amantadine Derivatives (3a, 7a) (3a, 7a–9a). Amantadine was reacted with different amine reagents in DCM using TEA and KI under reflux to yield the corresponding acetylated derivatives.

3.7 Purification of Synthesized Compounds Through Recrystallization

Following synthesis, the crude compounds were purified by the recrystallization method to remove unreacted starting materials and other impurities. An appropriate solvent was selected based on the solubility characteristics of the synthesized compounds. The product was dissolved in a minimum volume of solvent to obtain a clear solution. The solution was cooled gradually to room temperature, which allowed crystal formation and the obtained crystals were dried at room temperature. Recrystallization improved the purity and appearance of the synthesized compounds, yielding well-defined crystalline products. The purified compounds

were then used for characterization by spectroscopic techniques and for further biological evaluation.

3.8 of Synthesized Compounds Characterization

3.8.1 Determination of Melting Point

Melting points were recorded using a Gallenkamp melting point apparatus. A small amount of powdered sample was loaded into a capillary tube sealed at one end and inserted into the apparatus, where it was heated at a gradual rate. The point at which the sample fully transitioned to a liquid state was noted as its melting point.

3.8.2 Solubility Testing

Each synthesized compound was tested for solubility across a panel of selected solvents. Small amounts of each compound were placed into individual Eppendorf tubes along with the corresponding solvent, mixed thoroughly, and gently agitated to promote dissolution. The tubes were then left undisturbed so any undissolved or precipitated material could be observed. Solubility outcomes were determined visually, based on whether the solution remained clear or retained residual solid.

3.8.3 Fourier Transform Infrared Analysis

FTIR spectroscopy was used to confirm different types of function groups present in the compounds. Spectra were acquired on a Bruker FTIR spectrometer across the 4000-400 cm^{-1} range, with samples prepared according to standard instrument protocols. The resulting absorption bands were then examined to verify that the expected functional groups and structural changes were present in each derivative.

3.9 *In-silico* Studies

To characterize how the synthesized compounds interact with the target protein, molecular docking studies were conducted to assess their binding behavior. These *in-silico* analyses aimed to estimate binding affinities and pinpoint the specific amino acid residues driving protein–ligand interactions. The docking results provided structural information through which the compounds may exert their biological activity and used in identifying candidates with favorable binding profiles for further investigation [71].

3.9.1 Molecular Docking profiling

3.9.1.1 Retrieval of Protein Structures

The 3-D structures of the target enzymes acetylcholinesterase (AChE), butyrylcholinesterase (BChE), and β-secretase-1 (BACE1) were downloaded Protein Data Bank (PDB) in PDB format. The receptor molecules used for docking corresponded to PDB entries 1F8U, 1P0Q, and 1W50, respectively.

3.9.1.2 Preparation of Protein Macromolecules

Protein preparation was carried out in PyRx using its integrated AutoDock Vina module, with water molecules, bound ligands, and other heteroatoms removed from each structure prior to docking. Structural quality of the prepared proteins was verified using Ramplot, while BIOVIA Discovery Studio 2025 was used to inspect the receptors and map out their active binding sites [72].

3.9.1.3 Ligand Preparation

Each synthesized amantadine derivative was converted into an energy-minimized, three-dimensional structure using PyRx version 0.8, with the Universal Force Field

(UFF) applied for energy minimization. The resulting optimized ligand structures were saved in PDBQT format in preparation for docking.

3.9.1.4 Ligand–Protein Docking

Docking runs were performed in PyRx version 0.8, powered by the AutoDock Vina engine. Each prepared ligand was docked against its corresponding receptor within a predefined active-site grid, and the resulting binding affinities (kcal/mol) were logged as a measure of interaction strength between the synthesized compounds and their targets. All docking runs used AutoDock Vina's default parameter settings [73].

3.9.1.5 Docking Analysis and Visualization

Resulting docking poses were evaluated by using DSV, allowing detailed inspection of protein–ligand interactions such as H-bonds, π–π stacking and hydrophobic contacts. Both 2D and 3D interaction diagrams were generated for each complex to map out non-covalent binding contacts and compare binding modes across the synthesized compounds [74].

3.9.2 ADMET Assessment

The PK profiling of the synthesized derivatives was predicted using the SwissADME web server. Parameters including GI absorption, BBB permeability, lipophilicity, aqueous solubility, oral bioavailability, and compliance with Lipinski's Rule of Five were evaluated. The BOILED-Egg model was also used to calculate brain penetration and GI absorption, allowing comparison of drug-likeness and pharmacokinetic profiles of the synthesized compounds [75, 76]. Toxicity prediction was performed using the ProTox-3.0 online platform. Predicted LD_{50} values, toxicity classes, and other toxicological endpoints were obtained according to the

methods described by Drwal et al. (2014) and Banerjee et al. (2018), providing a preliminary assessment of compound safety before biological evaluation [73, 77].

3.10 *In-vivo* Studies

3.10.1 Experimental Animals

All procedures in which the animals were used was performed accordance with National Institutes of Health (NIH) guidelines for laboratory animal use and received ethical clearance from the Bioethical Committee at Capital University of Science and Technology (CUST), Islamabad, Pakistan (Approval No. REC CUST/DERC/PH/ERF/PG/2026/017).

The study used female albino mice, aged 3–4 weeks and weighing between 20 and 30 g. Prior to the start of experiments, the animals were acclimatized under controlled housing conditions, maintained at 22±2°C with 50–60% humidity and a 12-hour light/dark cycle.

Throughout the study period, animals had unrestricted access to standard pellet feed and drinking water.

3.10.2 Reagents and Chemicals

Scopolamine hydrobromide, donepezil and dimethyl sulfoxide (DMSO) of analytical grade were used in the study.

Biochemical analysis was carried out using a commercially available COX-2 ELISA kit purchased from Nanjing Pars Biochem Co., Ltd. For administration, the synthesized compounds were first dissolved in 2% DMSO and then diluted with sterile 0.9% normal saline to obtain the required dosing concentrations.

3.10.3 Animal Grouping

Following acclimatization, the animals were divided into six groups, containing seven mice (n = 7) in each group. The treatment allocation was designed to include a normal control group, a disease-induced group, a standard treatment group, and three test groups receiving different doses of the synthesized compound.

3.10.4 Dose Administration

The dosing regimen employed in the present study was done by using already published protocols in which the dose of donepezil is within the range of 0.1–15 mg/kg in experimental models of AD [78]. To investigate the possible dose-dependent effects of the synthesized derivatives, three dose levels (1, 5, and 10 mg/kg) were selected. Donepezil was used as the reference standard. Prior to administration, both the standard drug and synthesized compounds were dissolved in 2% DMSO and subsequently diluted with normal saline. Cognitive impairment was induced by intraperitoneal injection of scopolamine (1 mg/kg), administered 30 minutes after treatment each day throughout the seven-day study period. All treatments were administered according to the designated experimental protocol. Individual doses were given according to the body weight of each animal to ensure accurate drug delivery and uniformity among treatment groups.

TABLE 3.1: Drug Administration Schedule

Groups	**Treatment**
Normal Control	Vehicle administered once a day for 7 days (i.p.)
Negative Control	Scopolamine (1 mg/kg) once daily for 7 days (i.p.)
Positive Control	Donepezil (5 mg/kg) once daily for 7 days (i.p.)
Test Group I	compound 7a (1 mg/kg, i.p.) 30 mints before scopolamine
Test Group II	compound 7a (5 mg/kg, i.p.) 30 mints before scopolamine
Test Group III	compound 7a (10 mg/kg, i.p.) 30 mints before scopolamine

3.10.5 Experimental Design

Behavioral assessments were conducted under uniform laboratory conditions in a temperature-controlled room maintained between 20 and 22°C. Cognitive effects of the treatments were evaluated using the MWM and Y-Maze tests. During the study period, mice underwent training sessions in the MWM, and behavioral testing was performed 30 minutes following drug administration. Escape latency time was recorded during each trial as an indicator of spatial learning and memory acquisition. On the seventh day, a probe trial was conducted to determine retention of memory, while spontaneous alternation behavior was determined using the Y-Maze test. Following completion of behavioral evaluations, animals were sacrificed using spinal dislocation, and brain tissues were carefully removed for further biochemical analysis. The collected tissues were homogenized in phosphate lysis buffer, centrifuged to obtain the supernatant, and tissues were freezed at -80°C until further analysis [79].

3.10.5.1 Behavioral assessment

Behavioral performance was evaluated using MWM and Y-maze tests to determine effects of synthesized compounds on learning and memory. All behavioral experiments were conducted under standardized laboratory conditions with controlled lighting and minimal external disturbances. Cognitive performance was assessed after drug administration according to the experimental schedule, and the recorded behavioral parameters were used for subsequent statistical analysis.

3.10.5.2 Morris Water Maze Test

The memory retention was determined using MWM test, and the apparatus of this test consists of a circular water tank containing an escape platform submerged below the water surface. Mice underwent an acclimatization period followed by daily training sessions in which they were allowed to freely swim and locate the hidden platform within a specified time. Escape latency was recorded throughout

the training period. The probe trial was conducted on final day, by removing the platform and the time spent in the target quadrant was observed to determine memory retention and number of times the animal has crossed the platform was calculated [80–82].

3.10.5.3 Y-Maze Test

The Y-maze test was used to determine memory through spontaneous alternation behavior. Mice were placed one by one in the maze and it explored all the arms without restriction. The sequence of arm entries was recorded, and spontaneous alternation percentage was calculated using the standard formula. Higher alternation percentages were considered indicative of improved working memory performance. The maze was cleaned between trials to eliminate odor cues [82, 83].

$$\text{Alternation} = \left[\frac{\text{Number of actual alternations}}{\text{Total number of arm entries} - 2}\right] \times 100$$

FIGURE 3.6: Y-maze apparatus for memory assessment

3.10.5.4 Determination of COX-2 Levels by ELISA

Following behavioral assessments, hippocampal tissues were isolated and homogenized for biochemical analysis. Cyclooxygenase-2 (COX-2) levels was measured using mouse COX-2 ELISA kit (Pars Biochem, Catalogue No: PRS-20648Mo, Lot

No: 202511) according to the published protocols. The 96 well plate was used for the determination of calibration curve at 450 nm. The obtained values were expressed as pg/mL and used to evaluate neuroinflammatory changes among the experimental groups [84].

3.10.5.5 Histopathological Evaluation Using Hematoxylin and Eosin Staining

10 % formalin solution was used to preserve brain tissues in H and E brain staining. The brain tissues are then enclosed in paraffin and then cut at 5 µm thickness. The tissues were stained with eosin and hematoxylin using standard protocols. The stained slides were then observed using light microscope and to study histological changes in the hippocampal region, and representative photomicrographs were captured for comparison among the treatment groups [85].

3.10.6 Statistical Analysis

GraphPad Prism 10.4.2 was used for statistical analysis, and experimental data was presented as mean ± standard deviation (SD). Tukey's post hoc and one-way analysis of variance (ANOVA) was used to measure the differences between experimental groups.

Chapter 4

Results

4.1 FTIR Spectral Data of Synthesized Compounds

The amantadine derivatives were synthesized by following previously reported literature methods, with good yields. The synthesized molecules were further characterized using FTIR spectroscopy to identify the characteristic functional groups and confirm the structural features of the obtained compounds.

4.1.1 FTIR Spectrum of 4-((E)-(((3s,5s,7s)-adamantan-1-yl) imino) methyl) phenol (1a)

The FTIR spectra of the synthesized compound is shown in Figure 4.1. A sharp peak is observed at 1650 cm^{-1} which is characteristic of the azomethine or imine (C=N) stretching vibration, confirming the formation of the Schiff base through condensation of amantadine with 4-hydroxybenzaldehyde. The band at 1455.48 cm^{-1} is of the aromatic C=C skeletal stretching vibration, confirming the aromatic benzene ring within the structure. The absorption band is observed at 1372.31 cm^{-1} which refers to the in-plane bending vibration of the phenolic O–H group.

TABLE 4.1: Spectral data of compound 1a

Functional Group	**Observed Wave number** (cm^{-1})
C=N	1522.63
Aromatic C=C	1455.48
C–N	1372.31
O–H	1315.35

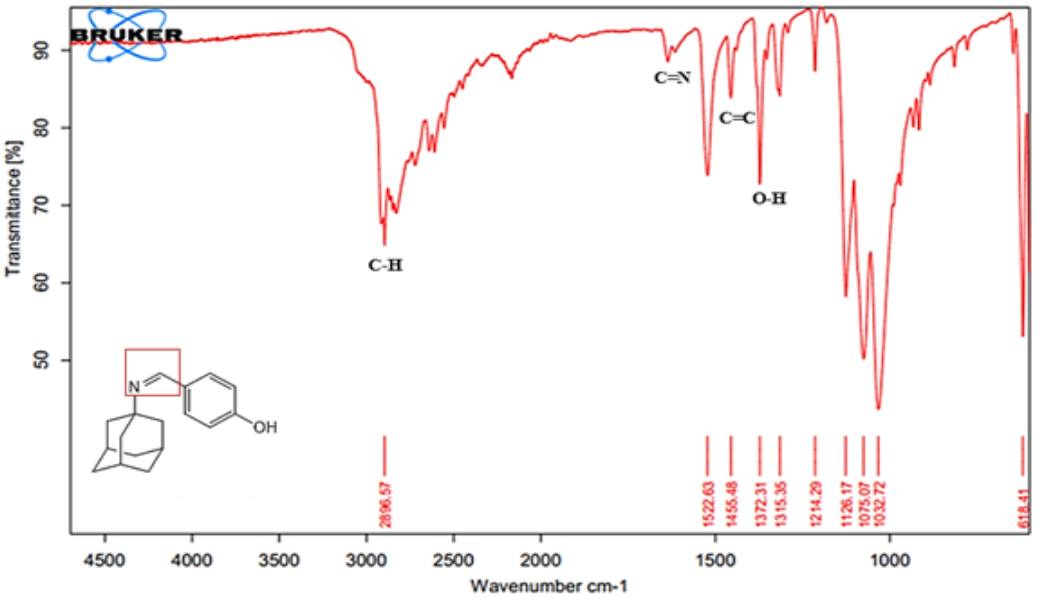

FIGURE 4.1: FTIR of compound 1a

4.1.2 FTIR Spectrum of 3-((E)-(((3s,5s,7s)-adamantan-1-yl) imino) methyl) phenol (2a)

The spectra of the synthesized compound is presented in Figure 4.2. A characteristic absorption band observed at 1650 cm^{-1} is of azomethine (C=N) group stretching vibration.

The absorption band at 1455.29 cm^{-1} is due to the aromatic C=C skeletal stretching vibration, confirming the presence of the substituted benzene ring. The absorption band observed at 1372 cm^{-1} is assigned to the in-plane bending vibration of the phenolic O-H group.

TABLE 4.2: Spectral data of compound 2a

Functional Group	**Observed Wave number** (cm^{-1})
C=N	1521.43
C=C	1455.29
C–N	1372.01
O–H	1315.10

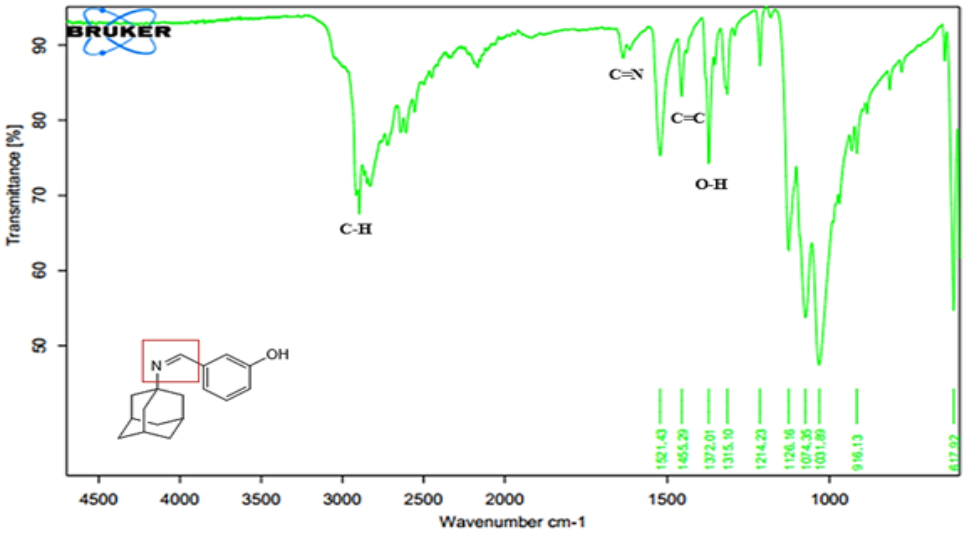

FIGURE 4.2: FTIR Spectral data of 2a

4.1.3 FTIR Spectrum of N-((3s,5s,7s)-adamantan-1-yl)-2-(benzothiazol-2-ylamino) acetamide (3a)

The spectrum of the synthesized compound is presented in Figure 4.3. The FTIR spectrum has a characteristic absorption at 3300 cm^{-1}, related to N–H stretching vibration, confirming the presence of an amine N–H group in the structure. The band at 1445.62 cm^{-1} refers to C–H bending vibrations, indicative of aliphatic C–H bonds within the molecule. Additionally, a strong absorption at 1640.28 cm ^{1} is assigned to the C=O stretching vibration, confirming the presence of a carbonyl (amide) functional group. Together, these peaks support the successful formation of the proposed amide-linked structure

TABLE 4.3: Spectral data of compound 3a

Functional Group	**Observed Wave number** (cm^{-1})
N–H stretching	2500–3000
C–H	2905.64
C=O	1640.28
C=C	1445.62
N–H bending	1531.67

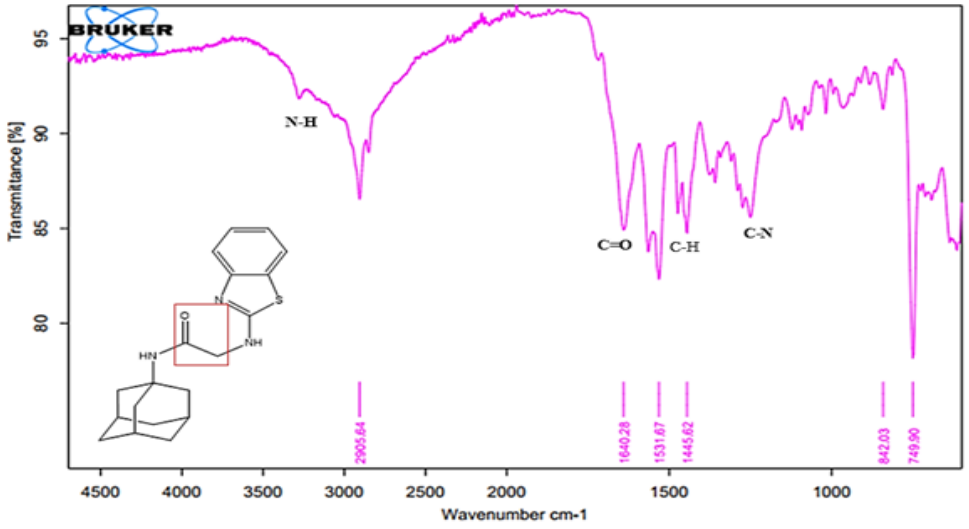

FIGURE 4.3: FTIR FTIR spectrum of 3a

4.1.4 FTIR spectrum of (Z)-N-((3s,5s,7s)-adamantan-1-yl)-1-(3,4,5-trimethoxyphenyl) methanimine (4a)

The spectrum shown in Figure 4.4 confirms the synthesis of the target Schiff base derivative through the presence of azomethine (C=N) stretching band at 1650 cm^{-1}, indicating the condensation of primary amino group of amantadine with aldehyde group of 3,4,5-trimethoxybenzaldehyde. The absorption observed in the 2900 cm^{-1} region is due to the aliphatic C–H stretching vibrations of the amantadine ring, confirming that the rigid hydrocarbon framework remained intact throughout the synthetic process. The band appeared at 1455.35 cm^{-1} indicates

the aromatic C=C skeletal stretching vibration, verifying the presence of the substituted aromatic ring. The O-H bending vibration appearing at 1372.31 cm^{-1} is due to the formation of imine linkage.

TABLE 4.4: FTIR spectrum of compound 4a

Compound	**Wave number** (cm^{-1})
Aliphatic C–H stretching	2800–3000
C=N	1523.15
C=C	1455.35
C–N stretching	1372.31

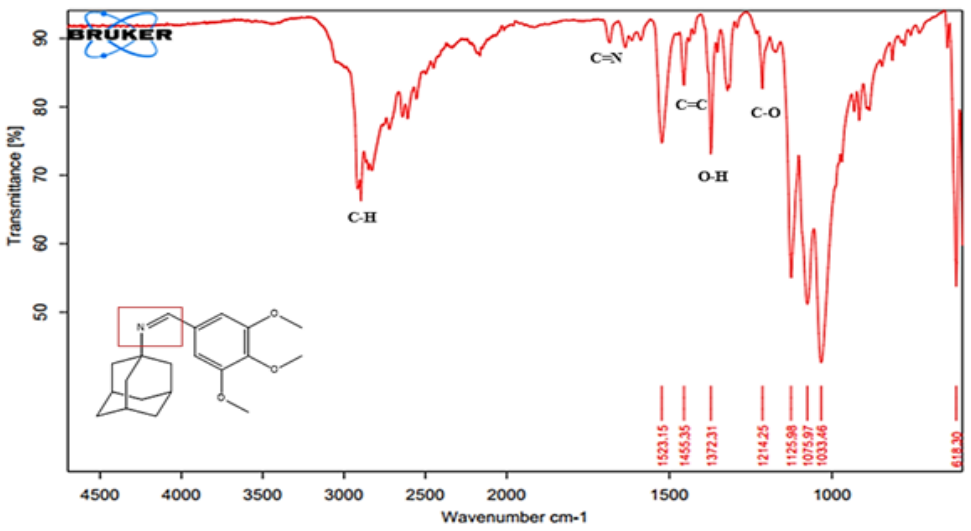

FIGURE 4.4: FTIR spectra of compound 4a

4.1.5 FTIR spectrum of 4-((Z)-(((3s,5s,7s)-adamantan-1-yl) imino) methyl)-2-methoxyphenol (5a)

The FTIR specta of the synthesized compound is presented in Figure 4.5. A characteristic absorption peak observed at 1650 cm^{-1} indicates the C=N stretching vibration of azomethine. The peak appeared at 2916.28 cm^{-1} is indicates the aliphatic carbon–hydrogen stretching vibrations of the amantadine ring. The band observed at 1455.38 cm^{-1} is due to the aromatic C=C skeletal stretching vibration,

which confirms the presence of the substituted aromatic ring. The peak at 1320.49 cm^{-1} is due to the in-plane bending vibration of the phenolic O–H group.

TABLE 4.5: FTIR spectrum of compound 5a

Compound	**Wave number** (cm^{-1})
C–H	2916.28
C=N stretching	1522.16
C=C	1455.38
C–N stretching	1372.19
O–H	1320.49

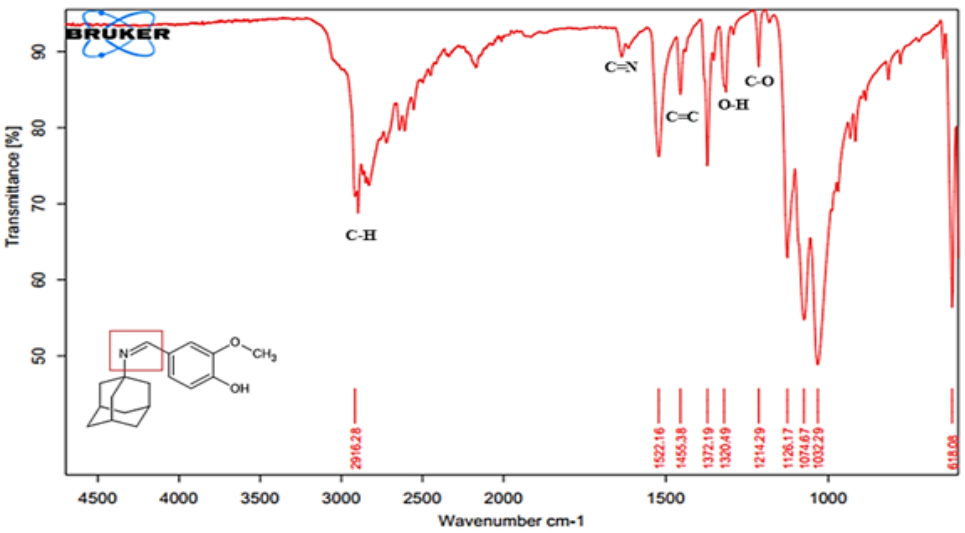

FIGURE 4.5: FTIR spectrum of compound 5a

4.1.6 FTIR spectrum of 4-((Z)-(((3s,5s,7s)-adamantan-1-yl) imino) methyl)-N, N-dimethylaniline (6a)

The spectrum of the synthesized compound is presented in Figure 4.6. An absorption band observed at 1650 cm^{-1} confirm the C=N stretching vibration of azomethine, which is the indication for the formation of Schiff base. The band observed at 1450 cm^{-1} is due to the aromatic C=C skeletal stretching vibration, which confirms the presence of the substituted aromatic ring. The absorption

band appearing at 1372.33 cm^{-1} is associated with the C–N stretching vibration of the imine linkage, providing further evidence for Schiff base formation. The absorption observed in the 2850–2950 cm^{-1} region is associated with the aliphatic carbon–hydrogen stretching vibrations of the amantadine ring.

TABLE 4.6: FTIR spectra of compound 6a

Compound	**Wave number** (cm^{-1})
C=N stretching	1523.13
C–N stretching (Imine)	1372.33
Aliphatic C–H stretching	2850–2950

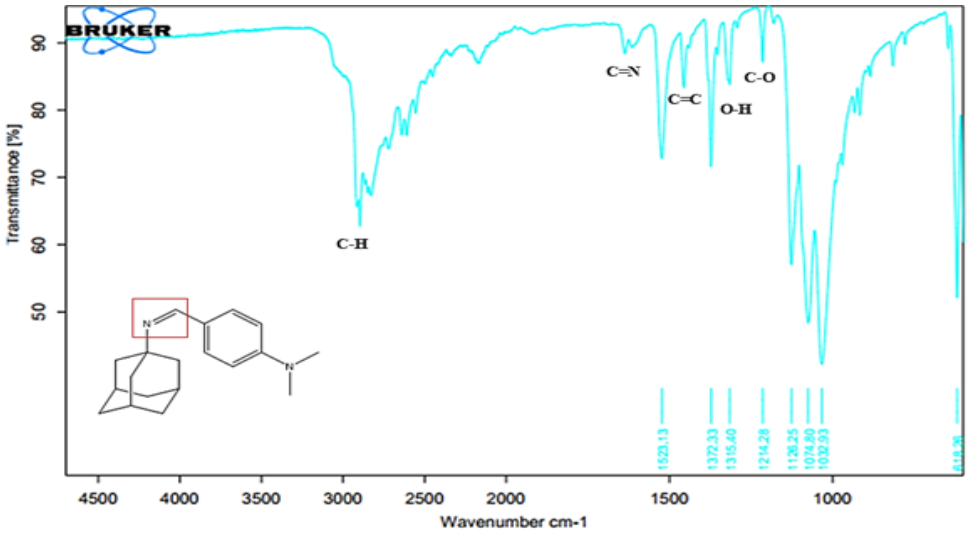

FIGURE 4.6: FTIR spectrum of compound 6a

4.1.7 FTIR spectrum of N-(adamantan-1-yl)-2-(4-(8-chloro-5,6-dihydro-11H-benzo [5, 6] cyclohepta [1, 2] pyridin-11-ylidene) piperidin-1-yl) acetamide (7a)

The spectrum of the synthesized compound is presented in Figure 4.7. The broad peak observed at 3500.35 cm^{-1} is associated with the secondary amide group nitrogen–hydrogen stretching vibrations. The peak appeared at 1434.73 cm^{-1} might be due to the aliphatic C–H bending vibrations of the amantadine ring.

A strong and sharp peak observed at 1680 cm^{-1} is associated with the amide carbonyl (C=O) stretching vibration, confirming the successful formation of the acetamide linkage.

TABLE 4.7: FTIR spectra of compound 7a

Compound	**Wave number** (cm^{-1})
N–H stretching	3500.35
Aliphatic C–H stretching	2922.52
C=O stretching	1724.65
C=C stretching	1434.73
C–N stretching	1145.11

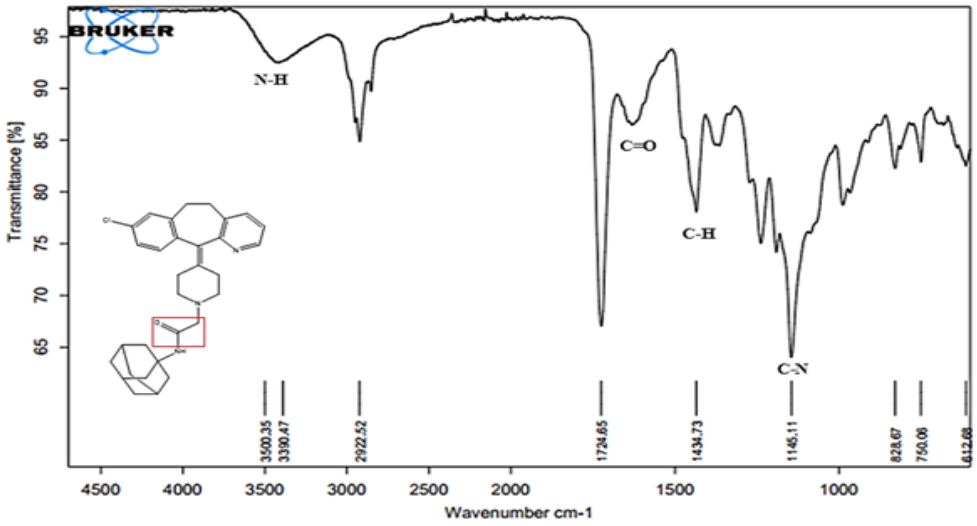

FIGURE 4.7: FTIR spectra of compound 7a

4.1.8 FTIR spectrum of N-((3s,5s,7s)-adamantan-1-yl)-2-((4-(N-(4,6-dimethylpyrimidin-2-yl) sulfamoyl) phenyl) amino) acetamide (8a)

The spectrum of the synthesized compound is presented in Figure 4.8. The broad absorption band at 1469.06 cm^{-1} indicate the nitrogen–hydrogen bending vibrations of the amide group, confirming the presence of functional group within the

synthesized compound. The absorption band at 1700 cm^{-1} represents the aliphatic carbon–hydrogen stretching vibrations of the amantadine ring. A prominent absorption band at 1628.89 cm^{-1} which shows the presence of the amide carbonyl (C=O) group. The absorption at 1085.96 cm^{-1} confirms the stretching vibration of carbon-nitrogen moieties.

TABLE 4.8: FTIR spectra of compound 8a

Compound	**Wave number** (cm^{-1})
N–H stretching	3480.64
C–H	2908.98
C=O	1628.89
C=N	1595.47
C=C	1502.92
S=O	1299.67
C–N stretching	1085.96
C–S	676.92

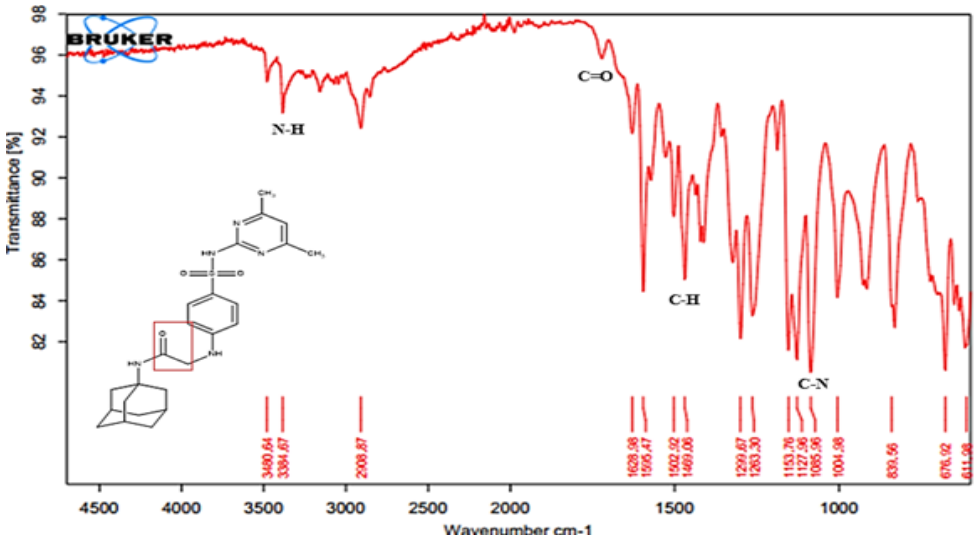

FIGURE 4.8: FTIR spectrum of compound 8a

4.1.9 FTIR spectrum of N-((3s,5s,7s)-adamantan-1-yl)-2-((4-(N-(6-methoxypyridazin-3-yl) sulfamoyl) phenyl) amino) acetamide (9a)

The spectrum of the synthesized compound is presented in Figure 4.9. The broad absorption bands at 3500.35 cm^{-1} indicate the N-H stretching vibrations of the amide group.

The absorption band at 1434.73 cm^{-1} represents the aliphatic C-H bending vibrations of the amantadine ring. A strong absorption band at 1700 cm^{-1} confirms the presence of amide carbonyl group, indicating the formation of the acetamide linkage.

The absorption band at 1145.11 cm^{-1} indicates the C-N stretching vibration of sulfonamide group, confirming the incorporation of the sulfonyl functionality into the synthesized molecule.

TABLE 4.9: FTIR spectra of compound 9a

Compound	**Wave number** (cm^{-1})
N–H stretching	3500.35
C–H	1434.73
C=O	1700
C=C	1434.73
C-N stretching	1145.11
C–S	612.68

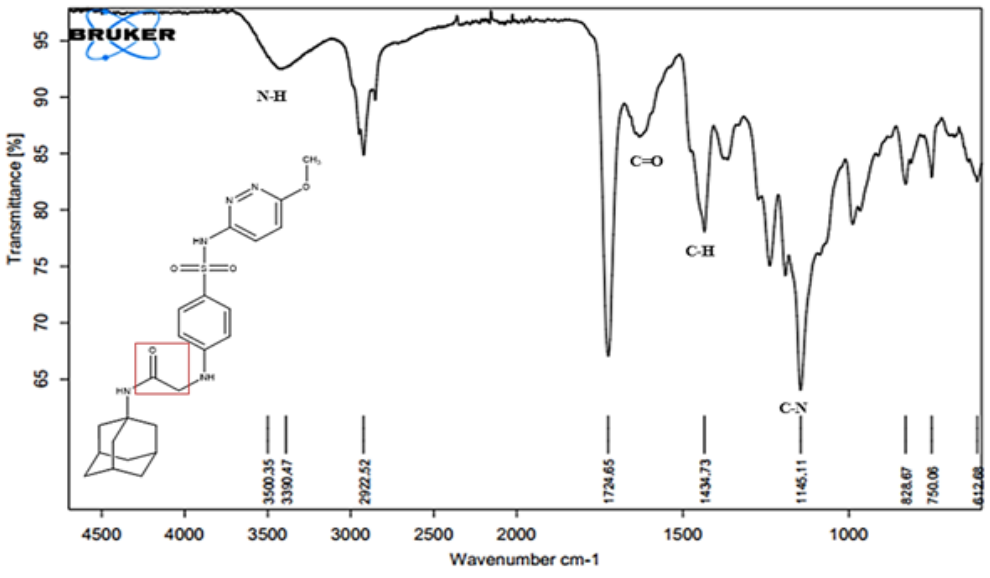

FIGURE 4.9: FTIR spectra of compound 9a

4.2 Physiochemical Evaluation

The physical evaluation of synthesized compounds including molecular formula, molecular weight (g/mol), melting point, physical states, color, percentage yield, solubility given in Table 4.10.

The physicochemical profile of synthesized derivatives (1a–9a) were calculated using SwissADME, and the obtained values were compared with the drug-likeness criteria, such as Veber's rules, Lipinski's Rule of Five, and predicted human intestinal absorption (HIA) parameters. According to Lipinski's Rule of Five, the molecular weight should be less than 500 Da for optimal oral bioavailability.

4.2.1 Pharmacokinetics Evaluation

The pharmacokinetic profile of the compounds were assessed such as blood-brain barrier (BBB) permeability, gastrointestinal (GI) absorption, and predicted oral bioavailability using online tool Swiss ADME.

According to standard ADME criteria, compounds with favorable physicochemical properties are expected to show high GI absorption for optimal oral bioavailability. The PK evaluations showed that none of the compounds showed inhibitory activity against Cytochrome 1A2 (CYP1A2).

Inhibition of CYP2C19 was predicted for compounds 4a and 9a, whereas only 3a showed inhibition of CYP2C9. All synthesized derivatives were predicted to inhibit CYP2D6. In contrast, inhibition of CYP3A4 was observed for compounds 3a, 4a, 5a, 7a, and 8a.

The BOILED-Egg (Brain or Intestinal Estimated permeation) model was used to evaluate the passive HIA and BBB permeability of the designed compounds (1a-9a). The model is based on two physicochemical descriptors that are, topological polar surface area (TPSA) and lipophilicity (WLOGP). In this model, white region shows high gastrointestinal absorption, while the yellow region of yolk indicates a high probability of BBB penetration (Figure 4.10).

TABLE 4.10: Bioavailability and pharmacokinetic evaluation of the synthesized derivatives (1a–9a), including GI absorption, BBB permeability, P-gp substrate status, CYP450 isoenzyme inhibition profiles, and bioavailability scores.

Compound	**Molecular formula**	**Molecular weight (g/mol)**	**Melting point (°C)**	**Physical state**	**Color**	**Percentage Yield (%)**	**Solubility**
1a	$C_{17}H_{21}NO$	255.36	290	Solid	White	65	Chloroform
2a	$C_{17}H_{21}NO$	255.36	275	Solid	White	58	Chloroform
3a	$C_{19}H_{23}N_3OS$	341.47	298	Solid	Canary Yellow	53	Dichloromethane
4a	$C_{20}H_{27}NO_3$	329.44	282	Solid	White	61	Chloroform
5a	$C_{18}H_{23}NO_2$	285.39	292	Solid	White	75	Chloroform
6a	$C_{19}H_{26}N_2$	282.21	286	Solid	White	73	Chloroform
7a	$C_{31}H_{36}ClN_3O$	502.10	250	Semisolid	Rust-brown	68	Dichloromethane
8a	$C_{24}H_{31}N_5O_3S$	469.60	293	Solid	White	52	Chloroform
9a	$C_{23}H_{29}N_5O_4$	471.58	295	Solid	White	55	Chloroform

Table 4.11: Physiochemical property of derivatives calculated with SwissADME

S. No	**Molecular Formula**	MW	nHA	nAHA	F-Csp3	nRB	nHBA	nHBD	MR	TPSA (A ° 2)
1a	$C_{17}H_{21}NO$	**255.35**	**19**	**6**	**0.59**	**2**	**2**	**1**	**78.88**	**32.59**
2a	$C_{17}H_{21}NO$	**255.35**	**19**	**6**	**0.59**	**2**	**2**	**1**	**78.88**	**32.59**
3a	$C_{19}H_{23}N_3OS$	**341.47**	**24**	**9**	**0.58**	**5**	**2**	**2**	**98.5**	**82.26**
4a	$C_{20}H_{30}N_4$	**329.43**	**24**	**6**	**0.65**	**5**	**4**	**0**	**96.34**	**40.05**
5a	$C_{31}H_{36}ClN_3O$	**502.09**	**36**	**12**	**0.55**	**4**	**3**	**1**	**149.95**	**45.23**
6a	$C_{18}H_{23}NO_2$	**285.38**	**21**	**6**	**0.61**	**3**	**3**	**1**	**85.37**	**41.82**
7a	$C_{24}H_{31}N_5O_3S$	**469.6**	**33**	**12**	**0.54**	**8**	**5**	**3**	**127.96**	**121.46**
8a	$C_{24}H_{31}N_5O_3S$	**471.57**	**33**	**12**	**0.52**	**9**	**6**	**3**	**124.52**	**130.69**
9a	$C_{19}H_{26}N_2$	**282.42**	**21**	**6**	**0.63**	**3**	**1**	**0**	**91.07**	**15.6**

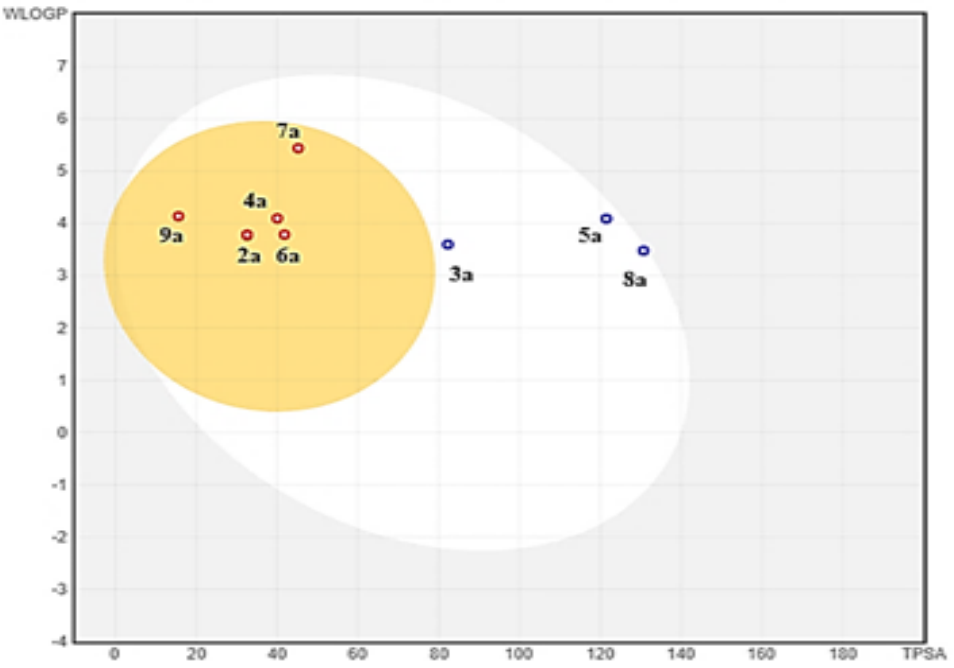

FIGURE 4.10: BOILED-Egg Analysis via SwissADME, showing predicted BBB permeability (yolk) and GI absorption (white) for compounds.

4.2.2 Drug Likeness Assessment

The drug-likeness characteristics of synthesized amantadine derivatives were predicted using established drug-likeness filters. Evaluation of the synthesized derivatives against the established drug-likeness filters showed that compounds 1a–4a and 6a-9a complied with all the assessed criteria, including Lipinski, Muegge rules, Ghose Egan, and Veber rule. In contrast, compound 5a showed two Lipinski violations, three Ghose violations, and one Muegge violation. No Veber or Egan rule violations were observed for any of the synthesized compounds.

4.2.3 Medicinal Chemistry

The alerts and synthetic accessibility scores of the synthesized derivatives were predicted using Swiss ADME. None of the synthesized compounds showed any PAINS alerts. Brenk analysis identified one imine alert for compounds 1a, 2a, 4a,

6a, and 9a, whereas compounds 3a, 5a, 7a, and 8a showed no Brenk alerts. Lead-likeness evaluation indicated a single XLOGP3 > 3.5 violation for compounds 1a, 2a, 3a, 4a, 6a, and 9a. Compound 5a showed two lead-likeness violations, the predicted synthetic accessibility scores ranged from 4.39 to 6.38, with compound 1a having the lowest score of 4.39 and compound 5a the highest of 6.38.

All synthesized compounds showed no PAINS alerts, indicating the absence of potentially problematic substructures. Brenk alerts were identified in compounds 1a, 2a, 4a, 6a, and 9a, each exhibiting a single alert, whereas compounds 3a, 5a, 7a, and 8a showed no Brenk alerts. Analysis of lead-likeness revealed that compounds 1a, 2a, 3a, 4a, 6a, and 9a each showed one violation, while compounds 5a, 7a, and 8a showed two violations. The synthetic accessibility scores ranged from 4.39 to 6.38, with compound 1a having the lowest score and 5a the highest, indicating that all derivatives possess moderate synthetic feasibility.

4.2.4 Lipophilicity

The lipophilicity of Compounds 1a–9a was evaluated using Swiss ADME, including iLOGP, XLOGP3, WLOGP, MLOGP, and Silicos-IT LogP, to ensure robustness and cross-validation of predictions.

Table 4.12: Calculated lipophilic parameters

Compd.	iLOGP	XLOGP3	WLOGP	MLOGP	Silicos-IT Log P
1a	2.62	3.79	3.78	3.21	4.03
2a	2.78	3.79	3.78	3.21	4.03
3a	3.06	4.72	3.6	3.12	3.94
4a	3.6	4.15	4.1	2.71	4.62
5a	4.23	6.99	5.44	4.7	6.24
6a	3.34	3.97	3.79	2.83	4.05
7a	2.8	2.96	4.09	1.57	2.38
8a	2.49	3	3.48	1.66	1.4
9a	3.37	4.27	4.14	3.68	4.15

4.2.5 Predicted Water Solubility

The water solubility of compounds 1a-9a was assessed by using computational models such as ESOL, Ali Log S, and SILICOS-IT. According to the ESOL model, compounds 1a and 2a were predicted to be soluble, compounds 3a, 4a, 6a, 7a, 8a, and 9a were moderately soluble, whereas 5a was poorly soluble. Based on the Ali model, compounds 1a, 2a, 4a, 6a, 7a, 8a, and 9a were classified as moderately soluble, while compounds 3a and 5a were predicted to be poorly soluble. According to the Silicos-IT model, compounds 1a and 2a were soluble, compounds 3a, 4a, 6a, and 9a were moderately soluble, and compounds 5a, 7a, and 8a were predicted to be poorly soluble.

4.3 Toxicological Evaluation

The toxicity profiles of the synthesized Compounds (1a–9a) were evaluated using in-silico acute oral toxicity prediction tool ProTox-3.0 expressed as LD_{50} values (mg/kg) and categorized according to the Globally Harmonized System (GHS) of Classification and Labelling of Chemicals. The results indicate that Compounds 1a, 2a, 4a, 6a, and 9a had predicted LD_{50} values of 3080 mg/kg, 3080 mg/kg, 3080 mg/kg, 3080 mg/kg, and 2670 mg/kg, respectively. These compounds fall within GHS toxicity Class 5, which are the substances that may be harmful if swallowed but generally possess relatively low acute toxicity.

Table 4.13: Acute Toxicity and Toxicity Class

Compd.	**LD50 (mg/kg)**	**GHS Toxicity Class**	**Toxicity Interpretation**
1a	3080	5	Might be harmful if swallowed
2a	3080	5	Might be harmful if swallowed

Table 4.13 continued from previous page

Compounds	LD50 (mg/kg)	GHS Toxicity Class	Toxicity Interpretation
3a	300	3	Toxic if swallowed
4a	3080	5	May be harmful if swallowed
5a	657	4	Harmful if swallowed
6a	3080	5	May be harmful if swallowed
7a	25000	6	Non-toxic
8a	1700	4	Harmful if swallowed
9a	2670	5	May be harmful if swallowed

4.3.1 Predicted Organ Toxicity

The potential organ toxicity of the synthesized ligands (1a–9a) was predicted using the ProTox-3.0 toxicity prediction platform, which predicts the probability of compounds causing toxicity to major organs, including the nervous system, liver, respiratory system, kidneys, and cardiovascular system.

In ProTox-3.0 predictions, toxicity is expressed as a probability score ranging from 0 to 1. According to the standard interpretation criteria, a probability value $\geq$0.50 is considered active (toxic), whereas a probability value $<$0.50 is classified as inactive (non-toxic).

Toxicity prediction indicated that all synthesized compounds (1a–9a) were inactive for hepatotoxicity, nephrotoxicity, and cardiotoxicity. Neurotoxicity was predicted to be active for compounds 1a, 2a, 3a, 4a, 5a, 6a, and 9a, while compounds 7a and 8a were predicted to be inactive.

4.3.2 Systemic and Genetic Toxicity

The systemic and genetic toxicity profiles of the designed compounds (1a–9a) were evaluated using in-silico toxicity prediction. The endpoints analyzed included carcinogenicity, immunotoxicity, mutagenicity, cytotoxicity, and clinical toxicity. Systemic and genetic toxicity prediction indicated that carcinogenicity was predicted to be active for compounds 4a, 6a, and 9a, while the remaining compounds were inactive. Immunotoxicity was predicted to be active for compounds 4a and 6a and inactive for all other derivatives. All compounds were predicted to be inactive for both mutagenicity and cytotoxicity. Clinical toxicity was predicted to be active for compounds 3a, 5a, and 8a, whereas the remaining compounds were inactive.

4.4 Structural Analysis of Target Proteins

4.4.1 Acetylcholinesterase PDB ID: 1F8U

The crystal three-dimensional structure of Acetylcholinesterase (AChE) was obtained from the Protein Data Bank in order to perfom molecular docking studies. The selected protein (PDB ID: 1F8U) structure was determined using X-ray crystallography with a resolution of 2.90 Å, indicating a reliable structural accuracy suitable for molecular docking analysis. The prepared structure was then used as the receptor for docking simulations to evaluate the binding interactions of the designed amantadine derivatives.

The Ramachandran plot generated for AChE, PDB ID: 1F8U, was used to evaluate the stereochemical property of the protein to assess the distribution of dihedral angles, namely psi (ψ), phi (ϕ) and of amino acid residues. The plot indicated that the majority of residues are clustered within the most favoured regions, that the overall backbone conformation of the protein is stereochemically acceptable and consistent with a well-refined crystal structure [83].

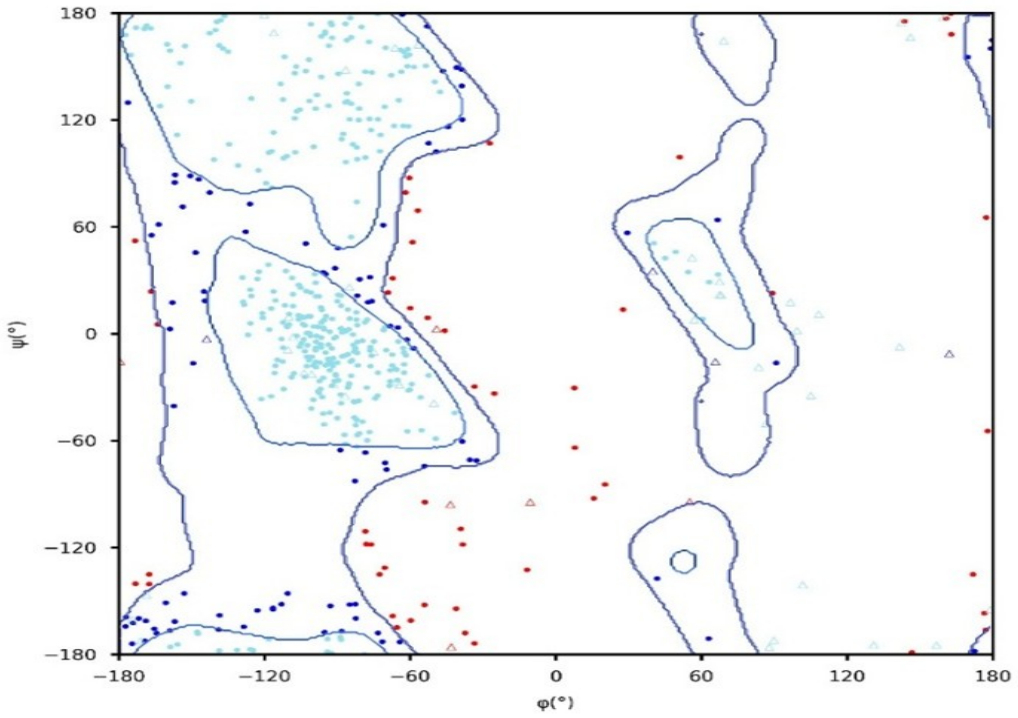

FIGURE 4.11: Ramachandran plot for the AChE crystal structure (PDB ID: 1F8U), showing distribution of backbone φ/ψ dihedral angles used for protein structure validation prior to molecular docking.

The interaction of ligands with AChE with PDB ID 1F8U are given below. It includes the binding affinities (kcal/mol), bonding interactions, and the types of intermolecular bonds responsible for stabilizing the protein-ligand complexes.

4.4.2 Evaluation of Binding Affinity and Molecular Interactions with Acetylcholinesterase

The binding affinity of the synthesized compounds were evaluated against AChE using molecular docking. The obtained docking scores ranged from -6.1 to -8.9 kcal/mol, demonstrate favorable interactions of the designed derivatives within the catalytic gorge of the enzyme. For comparison, the standard Alzheimer's drug Donepezil demonstrated a binding affinity of -6.8 kcal/mol under the same docking conditions.

Table 4.14: Docking analysis of synthesized compounds within 1F8U

Compound	Binding Affinity	Bonding Interaction	Interacting amino acid residues	Bond Type with
1a	-7.3	Conventional Hydrogen Bond, C-H Bond, Pi–Anion, Pi–Alkyl	TYR A:72, SER A:125, ASP A:74, TRP A:86, TYR A:337, PHE A:338	OH, C–H, C6H6, CH3
2a	-6.6	Pi–Pi Stacked, Alkyl	TYR B:61, LYS B:32	C6H6, CH3
3a	-8.0	Conventional Hydrogen Bond, Pi-Anion, Pi-Cation, Pi-Alkyl, and Alkyl bond	ASP A:400, ARG A:525, LYS A:332, GLU A:396, ASP A:333, VAL A:429	NH, C6H6, CH3
4a	-6.1	C-H Bond, Pi–Pi Stacked, Alkyl, and Pi–Alkyl	TYR B:61, LYS B:32, SER A:347	C6H6, CH3, C–H
5a	-8.9	Pi–Sigma, Pi–Alkyl and Alkyl	LYS B:32, TYR A:341, LEU A:76, TYR B:61	C6H6, CH3

Table 4.14 continued from previous page

Compound	Binding Affinity	Bonding Interaction	Interacting amino acid residues	Bond Type with
6a	-6.7	Conventional Hydrogen Bond and Alkyl bond	SER A:347, LYS B:32	OH, CH3
7a	-7.2	Conventional Hydrogen Bond, Pi-Pi Stacked, Pi-Sulfur, and Pi-Alkyl	ARG B:24, TYR A:77, SER A:347, LYS B:32, ALA A:343, TYR A:77, TYR B:61	NH, C6H6, S, CH3
8a	-7.0	Conventional Hydrogen Bond, C-H Bond, Amide-Pi Stacked, Pi-Pi T-shaped and Pi-Alkyl	TYR A:77, ARG B:24, GLY A:345, ASP A:349, TYR A:341, TYR A:341, TYR A:77, TYR B:61, LYS B:32	OH, NH, C–H, C6H6, CH3
9a	-6.4	Conventional Hydrogen Bond and Pi-Pi Stacked	SER A:347, TYR B:61	NH, C6H6

4.4.3 Butyrylcholinesterase PDB ID: 1P0Q

The crystal structure of butyrylcholinesterase (BChE) used in this study PDB ID: 1P0Q, was retrieved from RCSB Protein Data Bank (PDB), determined by X-ray diffraction and is considered suitable for molecular docking analysis due to its structural quality and refinement statistics. The structure has a resolution of 2.43 A ° which tells that the coordinates of the amino acid residues are sufficiently well defined for docking and binding analysis. The Ramachandran plot generated for BChE, PDB ID: 1P0Q, was used to evaluate the stereochemical property of the protein by assessing the backbone dihedral angles distribution, namely phi (ϕ) and psi (ψ), of the amino acid residues [83].

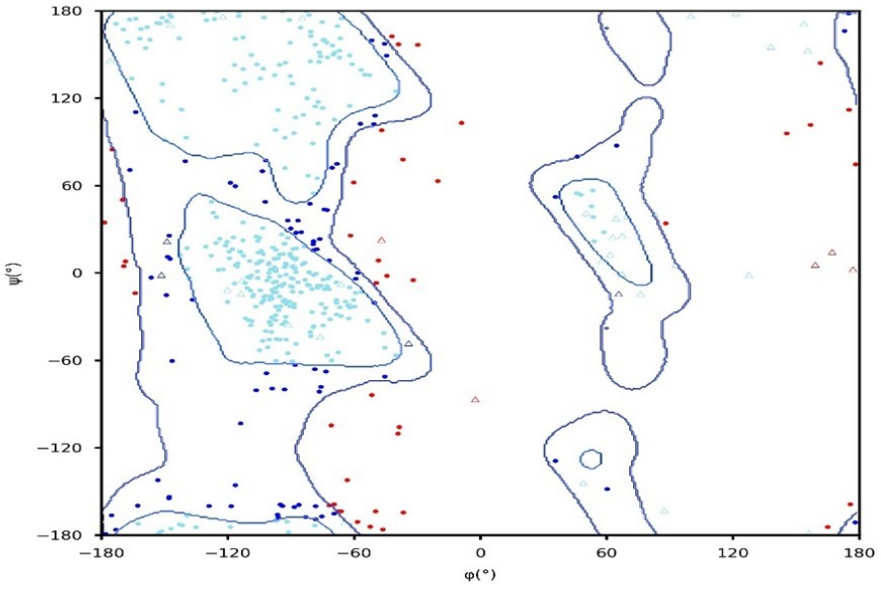

FIGURE 4.12: Ramachandran plot for the BChE crystal structure (PDB ID: 1P0Q), showing distribution of backbone φ/ψ dihedral angles used for protein structure validation prior to molecular docking.

The following table summarizes the molecular docking interactions of synthesized compounds with BChE with PDB ID 1P0Q. It includes the binding affinities (kcal/mol), the major bonding interactions observed, the amino acid residues interaction, and the corresponding types of intermolecular bonds responsible for stabilizing the protein-ligand complexes.

Table 4.15: Docking analysis of synthesized compounds within 1P0Q

Compound	Binding Affinity	Bonding Interaction	Interacting Amino acid residue	Bond Type with
1a	-8.4	Conventional Hydrogen Bond, Pi-Sigma bond, Pi-Pi T-shaped, Amide-Pi Stacked, Alkyl and Pi-Alkyl	GLU A:197, TRP A:82, GLY A:115, ALA A:328, PHE A:329	OH, C6H6, CH3
2a	-8.0	Conventional Hydrogen Bond, Pi-Pi T-shaped, Pi-Sigma, Alkyl, and Pi-Alkyl bond	GLU A:197, TYR A:128, TRP A:82, GLY A:115, GLY A:116, ALA A:328, PHE A:329, TYR A:332	OH, C6H6, CH3
3a	-10.2	Conventional Hydrogen Bond, Pi-Donor Hydrogen Bond, Pi-Sulfur, Pi-Sigma, Pi-Pi T-shaped, Alkyl and Pi-Alkyl Interaction	GLY A:116, THR A:120, SER A:198, TRP A:82, HIS A:438, PHE A:329, LEU A:286, ALA A:328, TRP A:430	NH, S, C6H6, CH3

Table 4.15 continued from previous page

Compound	Binding Affinity	Bonding Interaction	Interacting Amino acid residue	Bond Type with
4a	-8.0	Conventional Hydrogen Bond, C-H Bond, Pi–Sigma, Pi–Pi Stacked and Alkyl bond	THR A:120, TRP A:82, PHE A:329, LEU A:125, GLU A:197	OH, C6H6, CH3, C–H
5a	-10.9	Conventional Hydrogen Bond, Amide-Pi Stacked, Pi-Sigma, , Alkyl and Pi-Alkyl	THR A:120, GLY A:116, PHE A:398, LEU A:286, TRP A:231, PHE A:329, MET A:437, TRP A:430, GLY A:117, ALA A:328, TRP A:82	NH, C6H6, CH3
6a	-8.2	Conventional Hydrogen Bond, C-H Bond, Alkyl, Amide-Pi Stacked and Pi-Alkyl	HIS A:438, SER A:198, THR A:120, GLY A:116, ALA A:328, TRP A:82, PHE A:329, TYR A:332	OH, C–H, C6H6, CH3

Table 4.15 continued from previous page

Compound	Binding Affinity	Bonding Interaction	Interacting Amino acid residue	Bond Type with
7a	-10.4	Conventional Hydrogen Bond, Pi–Sigma Interaction, Amide–Pi Stacked and Alkyl Interaction,	LEU A:286, THR A:120, GLY A:116, GLY A:115, ALA A:328	NH, C6H6, CH3
8a	-10.2	Conventional Hydrogen Bond, Pi–Pi Stacked, Pi–Pi T-shaped, Alkyl and Pi–Alkyl	TRP A:82, TYR A:128, PHE A:329, ALA A:328, LEU A:125	S=O, O–H, C6H6, CH3
9a	-8.2	Carbon-Hydrogen Bond, Pi-Sigma, , Amide-Pi Stacked, Alkyl, Pi-Pi Stacked, Pi-Alkyl Interaction	SER A:198, LEU A:286, THR A:120, TRP A:231, GLY A:116, PHE A:329, ALA A:328, TRP A:82, TYR A:332, HIS A:438, PHE A:398	C–H, C6H6, CH3

4.4.4 Evaluation of Binding Affinity and Molecular Interactions with Butyrylcholinesterase

The binding affinity of designed compounds were evaluated against BChE, PDB ID: 1P0Q using molecular docking analysis.

The docking scores ranged from -8.0 to -10.4 kcal/mol, indicating interactions of the designed derivatives with the amino acid residues.

For comparison, the standard anti-Alzheimer drug Donepezil demonstrated a binding affinity of -9.7 kcal/mol under same docking conditions.

4.4.5 BACE (Beta Secretase) PDB ID: 1W50

The crystal structure of β-secretase (BACE-1) used in this study was retrieved from the PDB ID: 1W50.

BACE-1 is a well-established therapeutic target in Alzheimer's disease because it catalyzes the initial cleavage of Amyloid Precursor Protein (APP), leading to the formation of amyloid-β peptides.

The 1W50 structure was determined by X-ray diffraction at a resolution of 1.75 A$^\circ$, indicating a reliable and well-resolved 3-D model suitable for molecular docking and interaction studies.

The stereochemical feature of selected target protein PDB ID 1W50 was evaluated using a Ramachandran plot, which analyzes the backbone dihedral and psi (ψ) of amino acid residues and angles phi (ϕ) in the protein structure. The plot shows that the majority of residues are clustered within the most favoured and additionally allowed regions, indicating that the protein is stereochemically acceptable and consistent with a well-refined crystal structure [83].

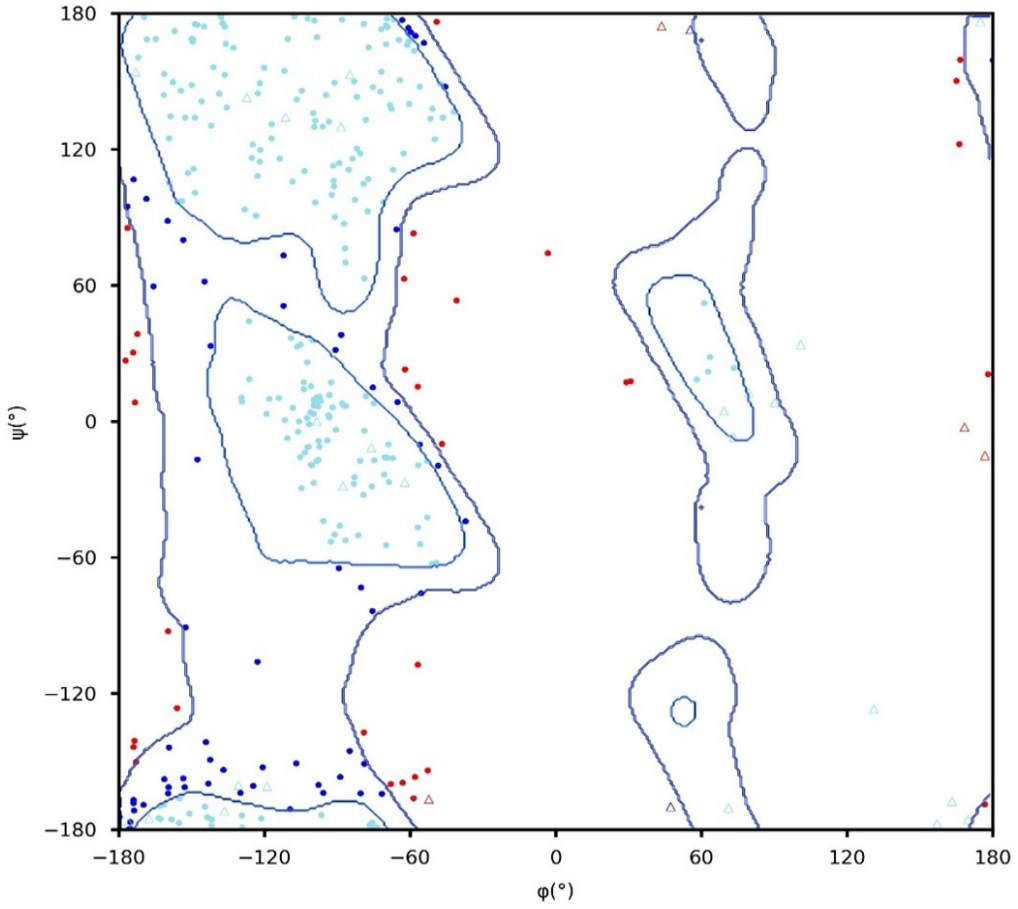

FIGURE 4.13: Ramachandran plot for the BACE-1 crystal structure (PDB ID: 1W50), showing distribution of backbone φ/ψ dihedral angles used for protein structure validation prior to molecular docking.

4.4.6 Evaluation of Binding Affinity and Molecular Interactions Against BACE-1

Molecular docking analysis was carried out to evaluate the binding behavior of the synthesized compounds (1a–9a) within the active site of BACE-1 PDB ID: 1W50. The docking results revealed binding affinity values were from -6.5 to -8.9 kcal/mol, indicating moderate to strong interactions of the tested ligands with the target enzyme. These values were compared with the standard drug donepezil, which showed a binding affinity of -7.5 kcal/mol under the same docking conditions.

TABLE 4.16: Docking analysis of compounds in 1W50: Binding affinity, interaction residues and bond types

Compound	Binding Affinity	Bonding Interaction	Interacting Amino acid residue	Bond Type with
1a	-6.9	Conventional Hydrogen Bond, Alkyl Interaction and Pi-Anion,	GLY A:34, ASP A:32, LEU A:30	OH, C6H6, CH3
2a	-6.6	Conventional Hydrogen Bond, Amide-Pi Stacked and Pi-Alkyl Interaction	THR A:231, GLY A:34, TYR A:71	OH, C6H6, CH3
3a	-7.8	Conventional Hydrogen Bond, Amide-Pi Stacked, Alkyl/Pi-Alkyl Interaction	THR A:231, GLY A:230, TYR A:198, VAL A:332, LEU A:30	S, C6H6, CH3
4a	-7.0	C-H Bond, Pi–Anion, Pi–Sigma, , Alkyl and Pi–Alkyl interaction	ASP A:32, SER A:35, ASN A:37, GLY A:34, TYR A:71, TRP A:76, ILE A:118, TYR A:198, ILE A:126, PHE A:108	C6H6, C-H, CH3
5a	-8.9	C-H Bond, Alkyl and Pi-Alkyl Interaction	SER A:35, VAL A:332, TYR A:198	C–H, C6H6, CH3

Table 4.16 continued from previous page

Compound	Binding Affinity	Bonding Interaction	Interacting Amino acid residue	Bond Type with
6a	-6.6	Conventional Hydrogen Bond, C-H Bond, Amide-Pi Stacked, Pi-Pi T-shaped, Alkyl and Pi-Alkyl bond	ARG A:128, TYR A:198, GLY A:34, GLY A:230, TYR A:71, ILE A:126	OH, C–H, NH, C6H6, CH3
7a	-8.1	Conventional Hydrogen Bond, Pi-Pi T-shaped, Alkyl and Pi-Alkyl Interaction	THR A:231, TYR A:71, ILE A:126, TYR A:198, ILE A:118, PHE A:108	O, C6H6, CH3
8a	-8.1	Conventional Hydrogen Bond, Carbon-Hydrogen Bond, Pi-Pi T-shaped, Pi-Alkyl Interaction	ASP A:32, LYS A:107, THR A:329, GLY A:230, TYR A:71, TYR A:198, PHE A:108	NH, C–H, C6H6, CH3
9a	-6.5	Pi-Sigma, Pi-Anion, Pi-Alkyl Interaction	TYR A:71, ASP A:32, PHE A:108, TYR A:198	C6H6, CH3

4.4.7 CYCLOOXYGENASE 2 PDB ID: 5 IKQ

The crystal structure of Cyclooxygenase 2 (COX-2) used in this study was retrieved from the PDB ID: 5IKQ. COX-2 is a key inducible enzyme in the arachidonic acid pathway, catalyzing the conversion of arachidonic acid to prostaglandin H_2, which is a process central to the inflammatory response implicated in neuroinflammation associated with Alzheimer's disease. The 5IKQ structure represents human COX-2, determined by X-ray diffraction at a resolution of 2.41 Å, indicating a reliable and well-resolved 3-D model suitable for molecular docking and interaction studies.

The stereochemical feature of selected target protein PDB ID 5IKQ was evaluated using a Ramachandran plot, which analyzes the backbone dihedral and psi (ψ) of amino acid residues and angles phi (ϕ) in the protein structure. The plot shows that the majority of residues are clustered within the most favored and additionally allowed regions, indicating that the protein is stereochemically acceptable and consistent with a well-refined crystal structure [81].

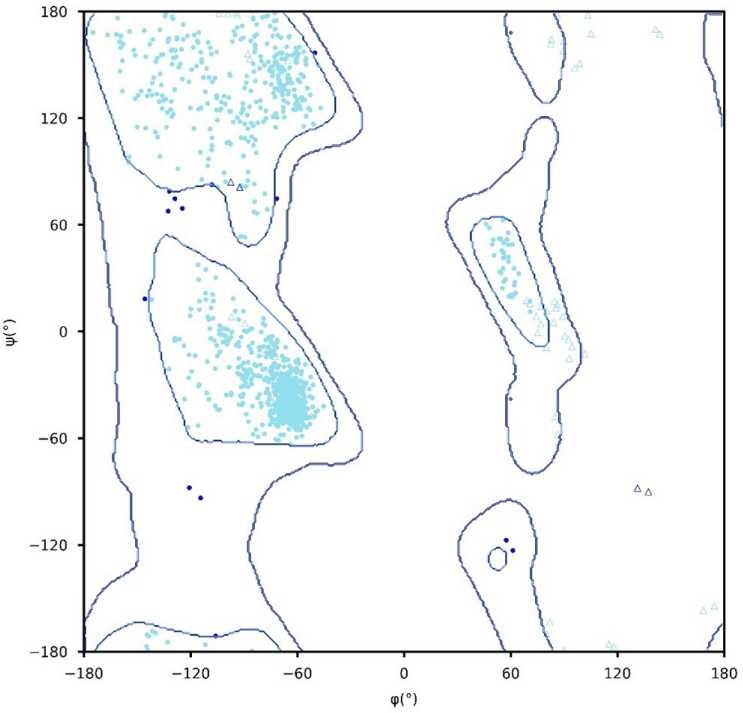

FIGURE 4.14: Ramachandran plot for the COX-2 crystal structure (PDB ID: 5IKQ), showing distribution of backboneφ/ψ dihedral angles used for protein structure validation prior to molecular docking.

4.4.8 Evaluation of Binding Affinity and Molecular Interactions Against COX-2

Molecular docking analysis was carried out to evaluate the binding behavior of the synthesized compounds (1a–9a) within the active site of COX-2 (PDB ID: 5IKQ.

The docking results revealed binding affinity values were from -7.2 to -10.6 kcal/mol, indicating moderate to strong interactions of the tested ligands with the target enzyme. These values were compared with the standard drug donepezil, which showed a binding affinity of -7.9 kcal/mol under the same docking conditions.

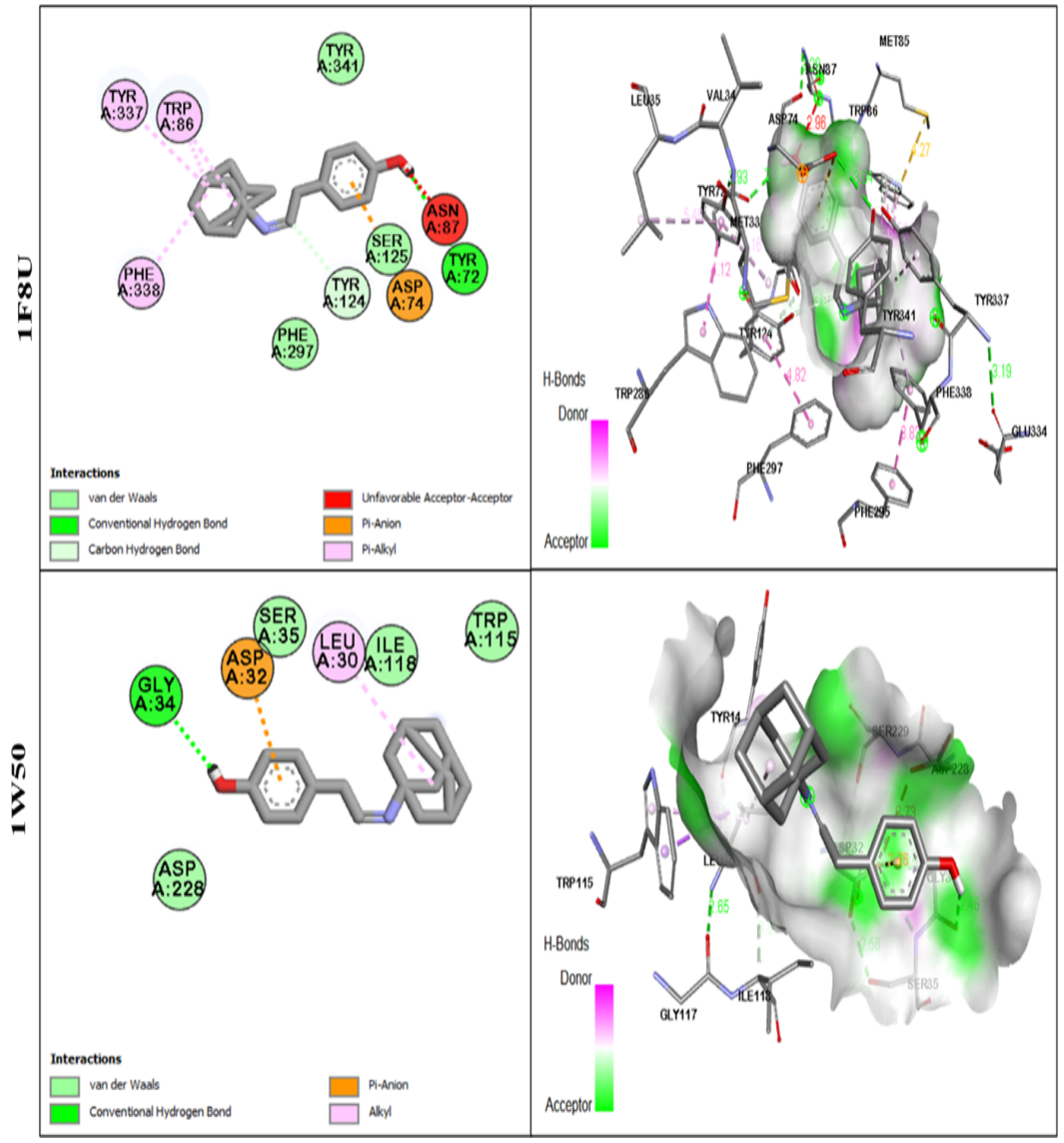

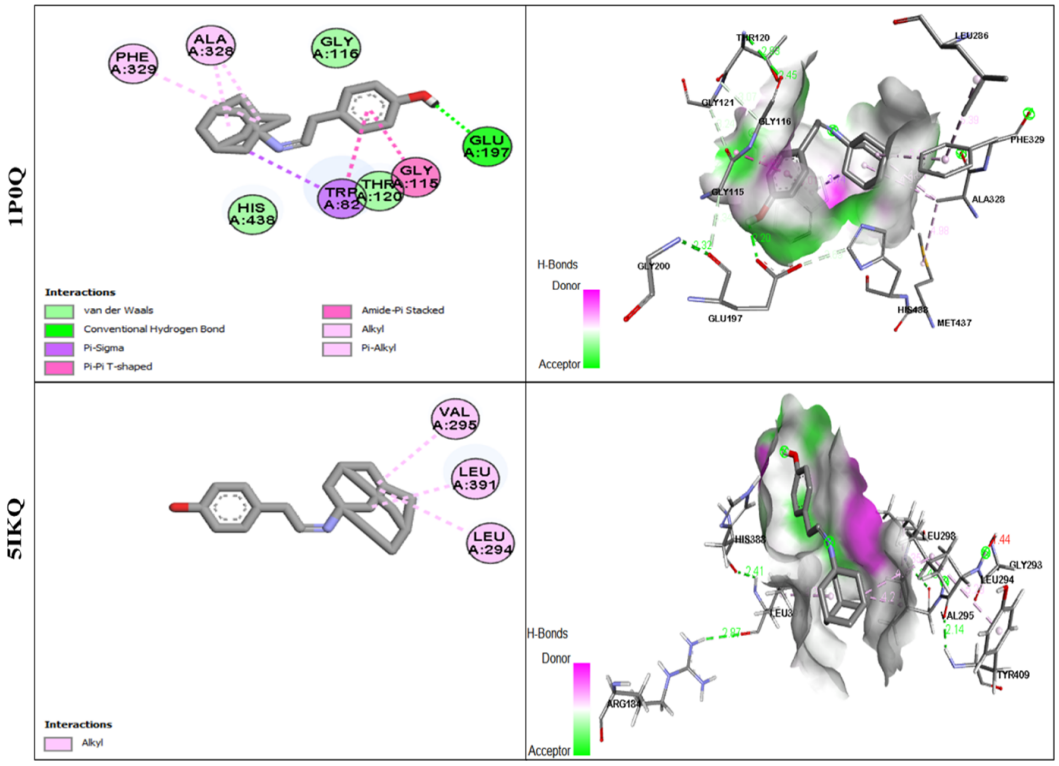

FIGURE 4.15: 2D and 3D molecular docking interaction diagrams of compound 1a within the binding pockets of 1F8U, 1P0Q, 1W50, and 5IKQ. 2D panels depict residue-level interactions and 3D panels show the corresponding docked pose within the respective binding site along with the hydrogen bond donor acceptor surface map.

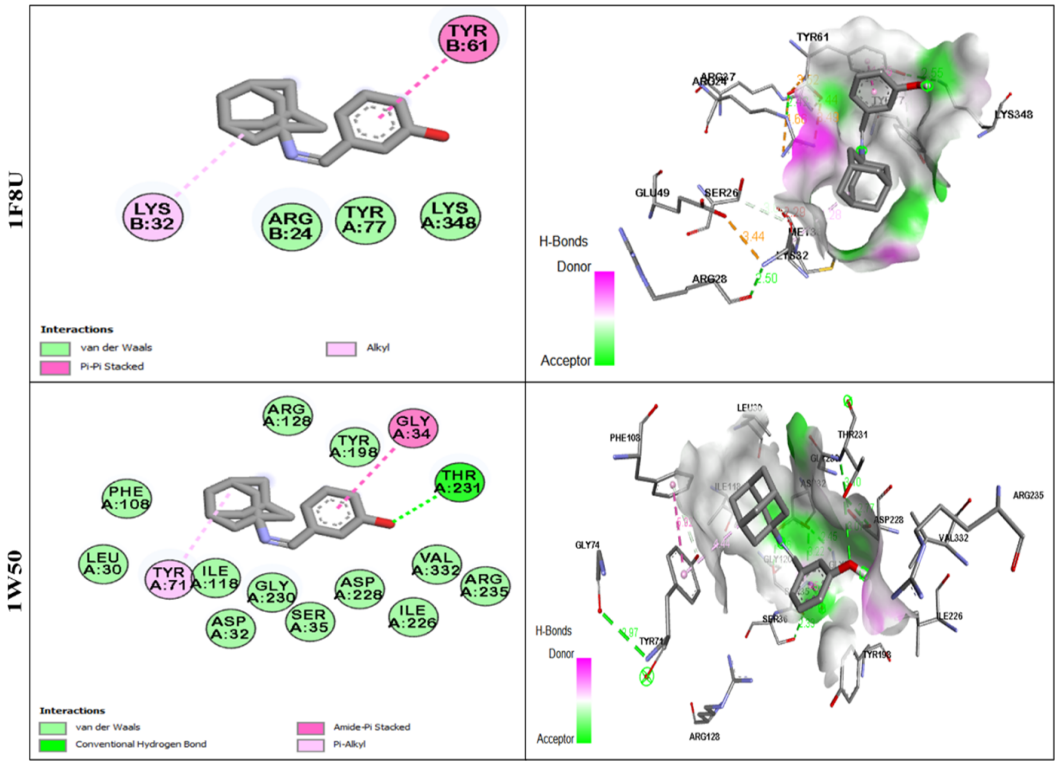

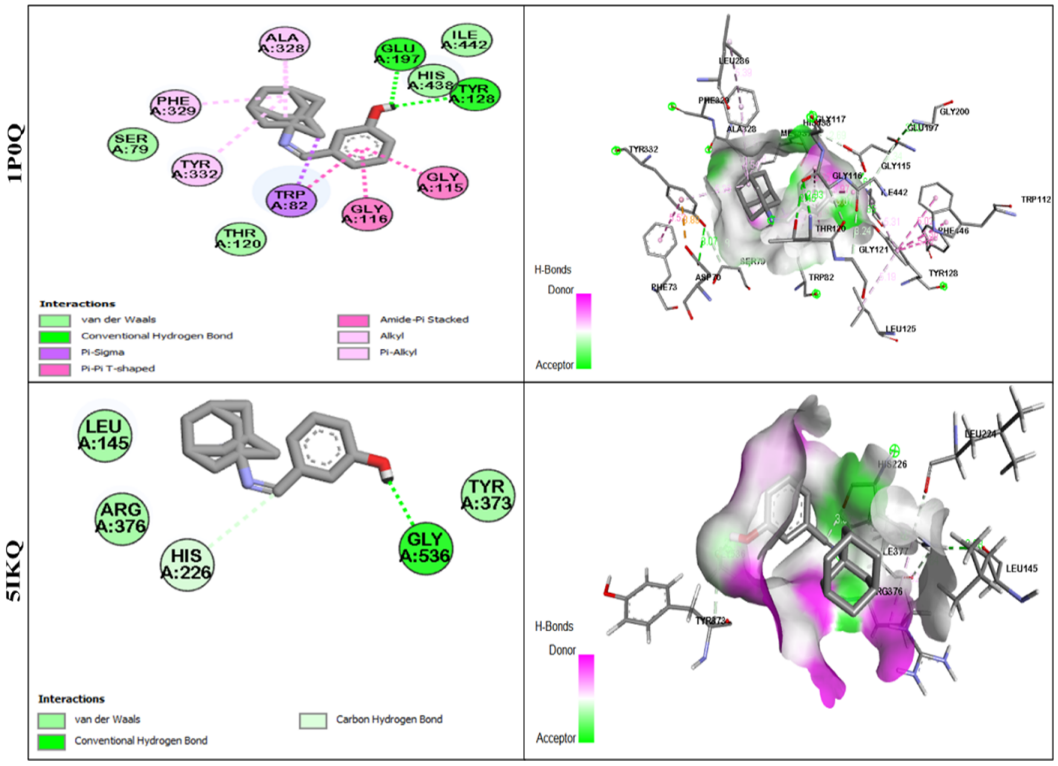

FIGURE 4.16: 2D and 3D molecular docking interaction diagrams of compound 2a within the binding pockets of 1F8U, 1P0Q, 1W50, and 5IKQ. 2D panels depict residue-level interactions and 3D panels show the corresponding docked pose within the respective binding site along with the hydrogen bond donor acceptor surface map.

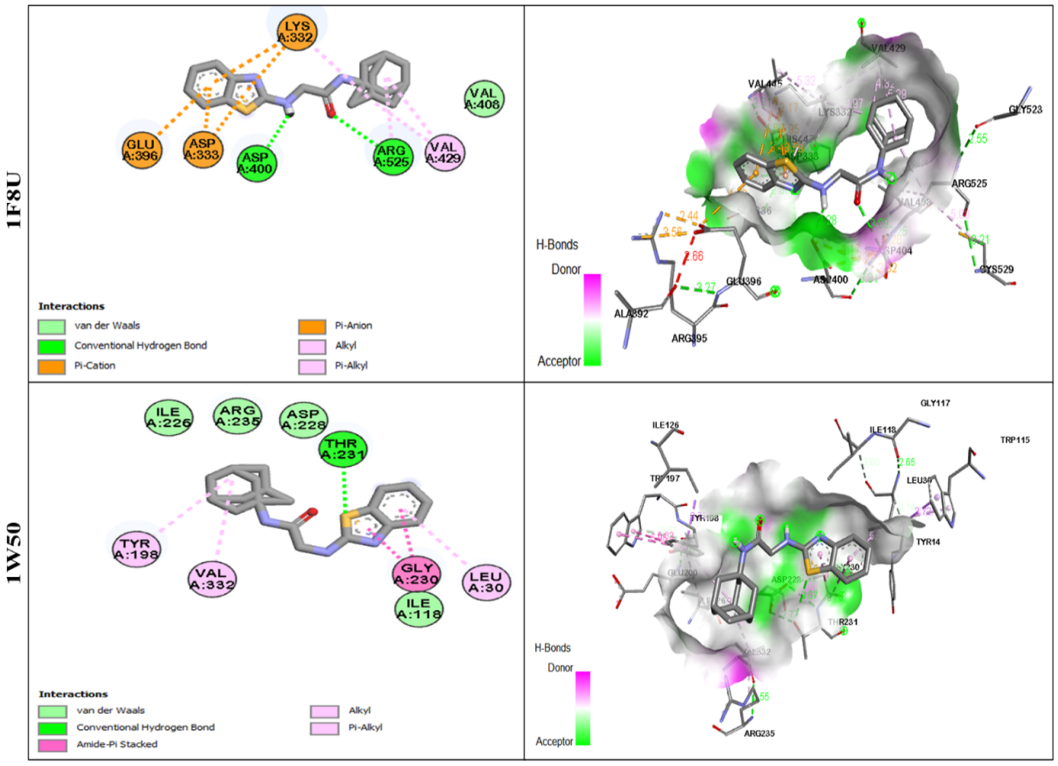

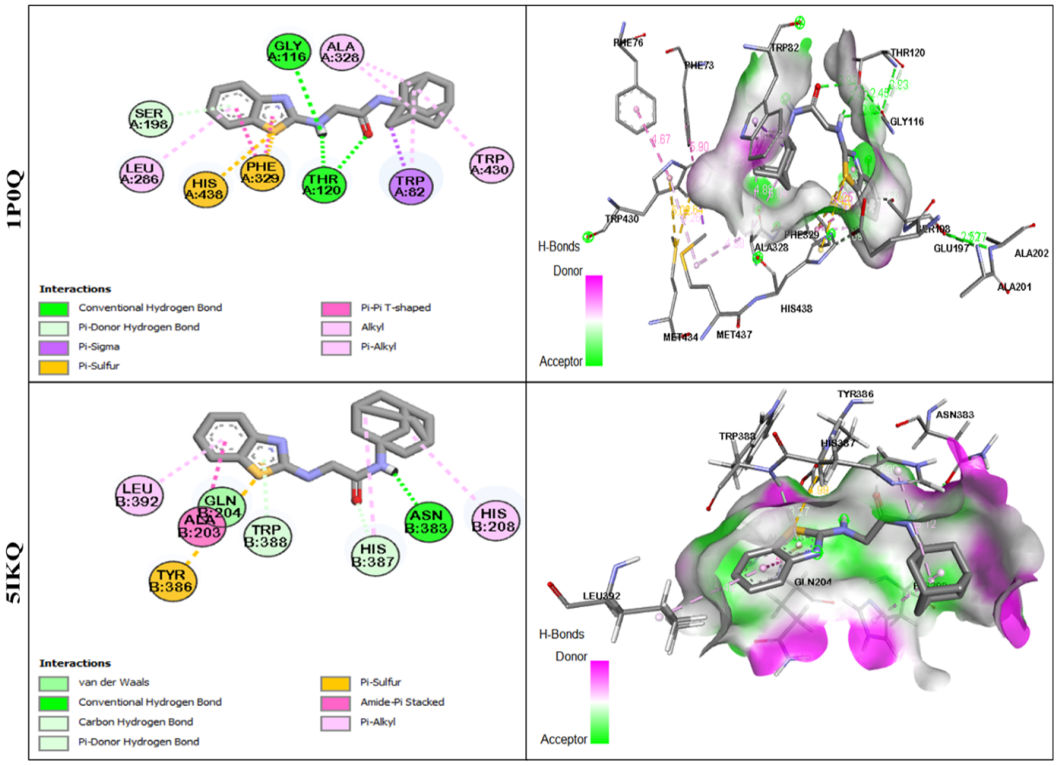

FIGURE 4.17: 2D and 3D molecular docking interaction diagrams of compound 3a within the binding pockets of 1F8U, 1P0Q, 1W50, and 5IKQ. 2D panels depict residue-level interactions and 3D panels show the corresponding docked pose within the respective binding site along with the hydrogen bond donor acceptor surface map.

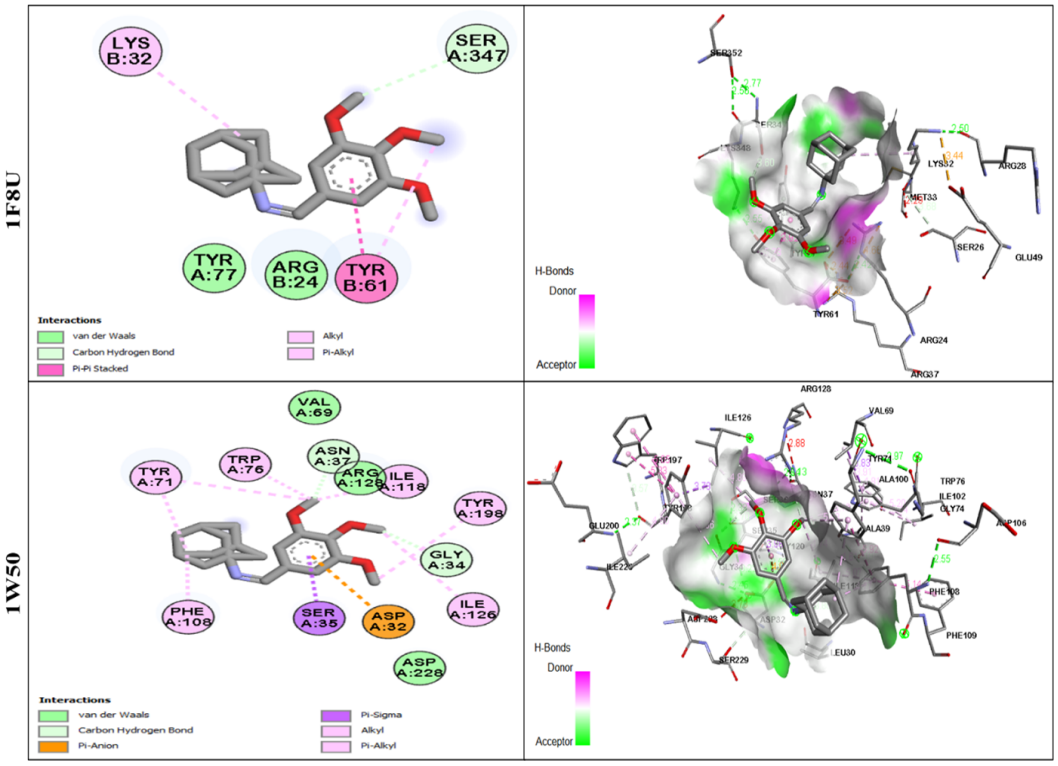

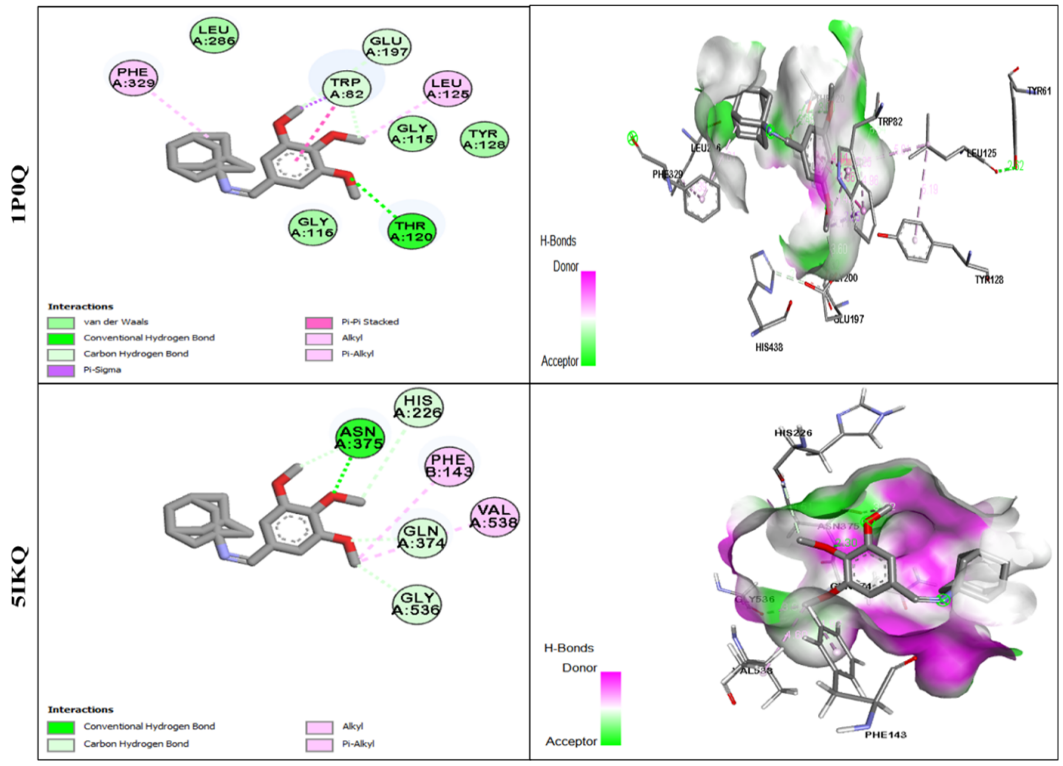

FIGURE 4.18: 2D and 3D molecular docking interaction diagrams of compound 4a within the binding pockets of 1F8U, 1P0Q, 1W50, and 5IKQ. 2D panels depict residue-level interactions and 3D panels show the corresponding docked pose within the respective binding site along with the hydrogen bond donor acceptor surface map.

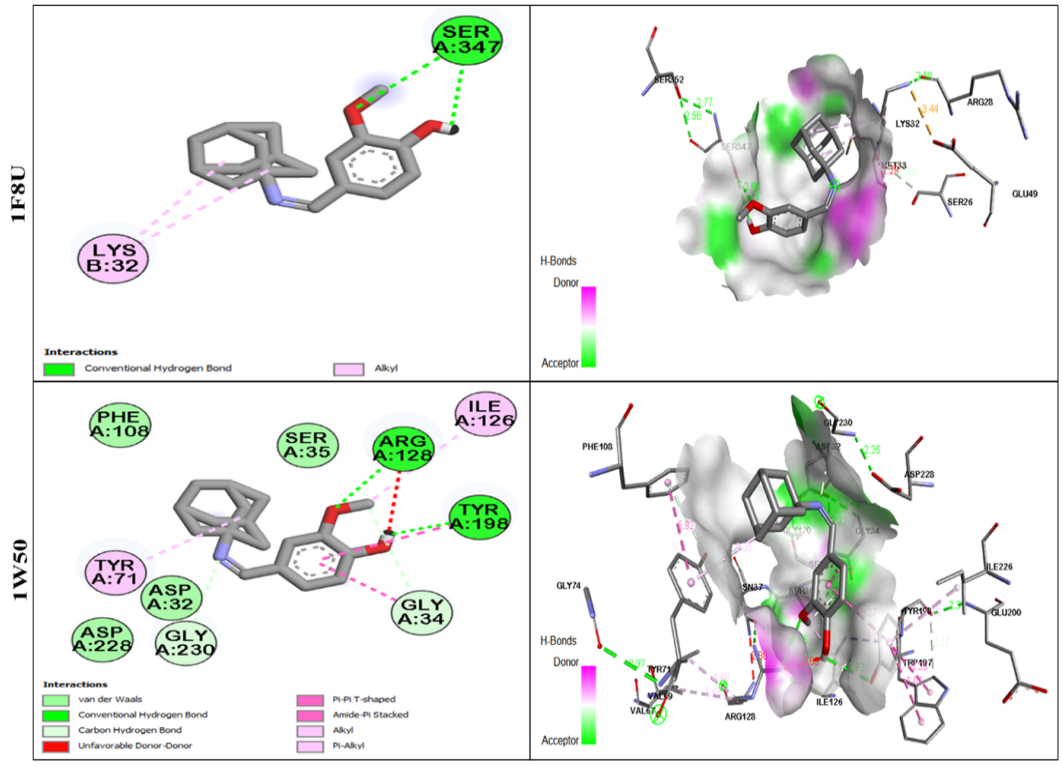

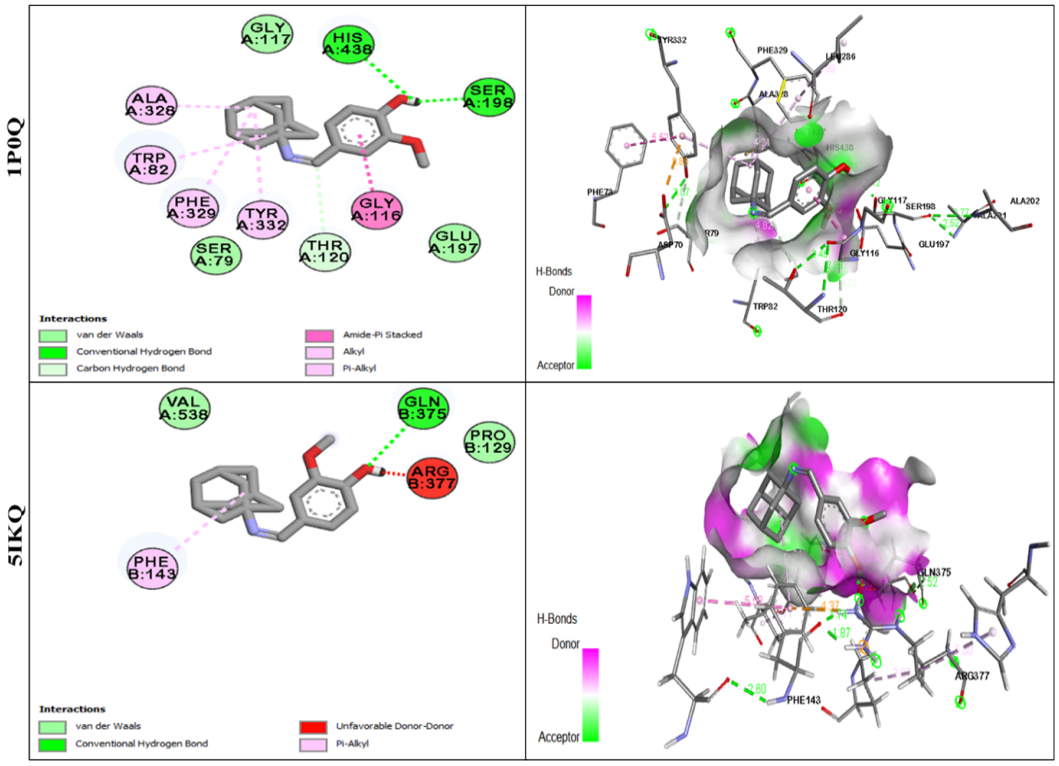

FIGURE 4.19: 2D and 3D molecular docking interaction diagrams of compound 5a within the binding pockets of 1F8U, 1P0Q, 1W50, and 5IKQ. 2D panels depict residue level interactions and 3D panels show the corresponding docked pose within the respective binding site along with the hydrogen bond donor acceptor surface map.

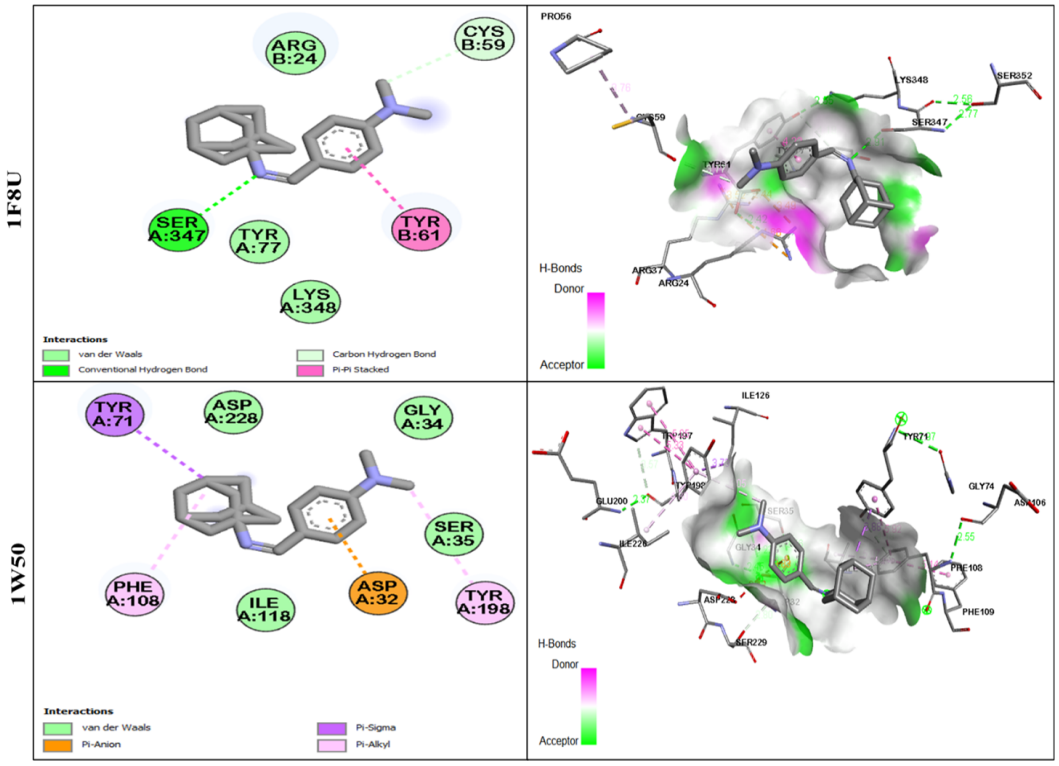

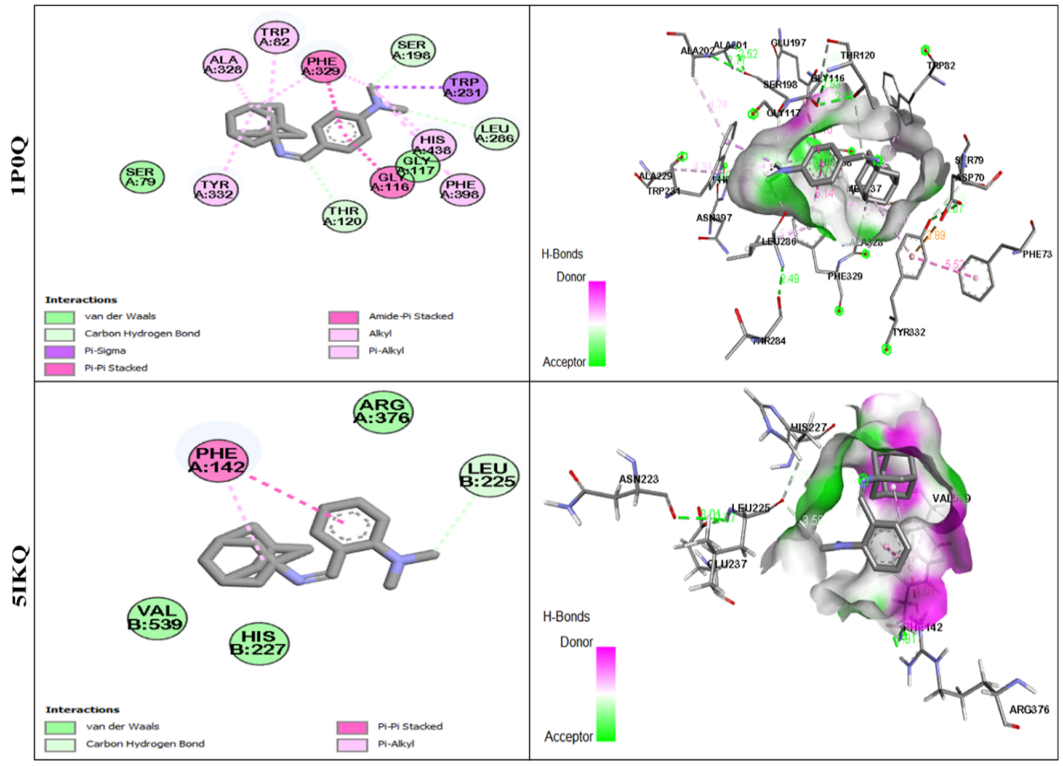

FIGURE 4.20: 2D and 3D molecular docking interaction diagrams of compound 6a within the binding pockets of 1F8U, 1P0Q, 1W50, and 5IKQ. 2D panels depict residue level interactions and 3D panels show the corresponding docked pose within the respective binding site along with the hydrogen bond donor acceptor surface map.

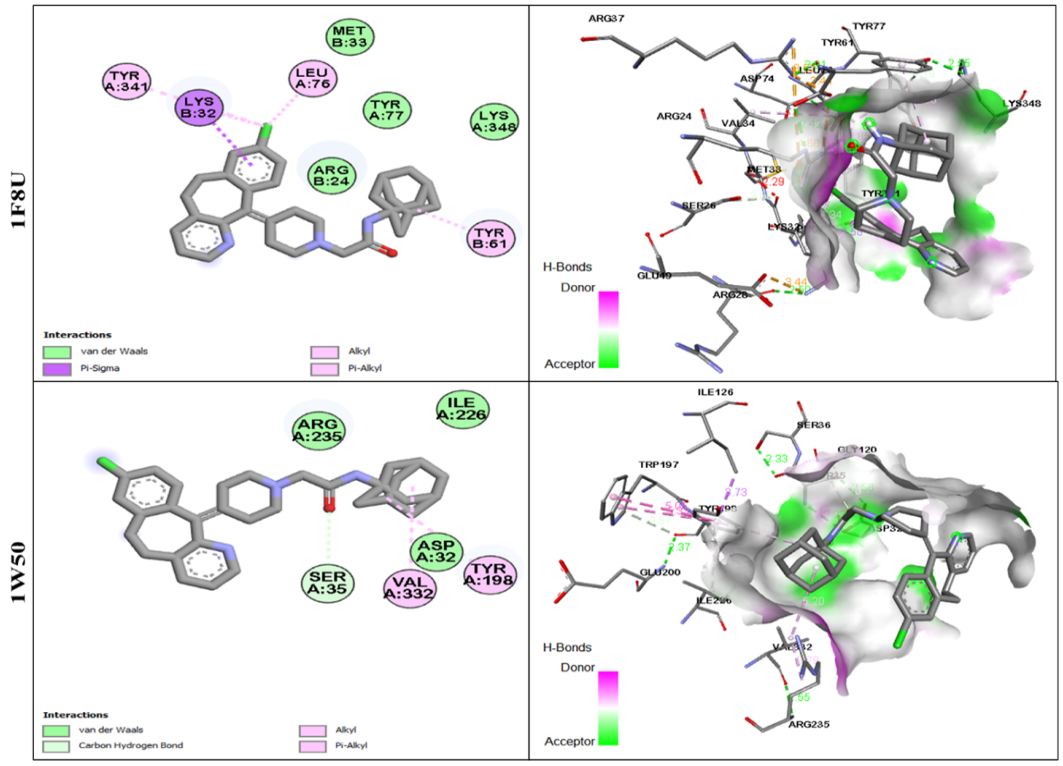

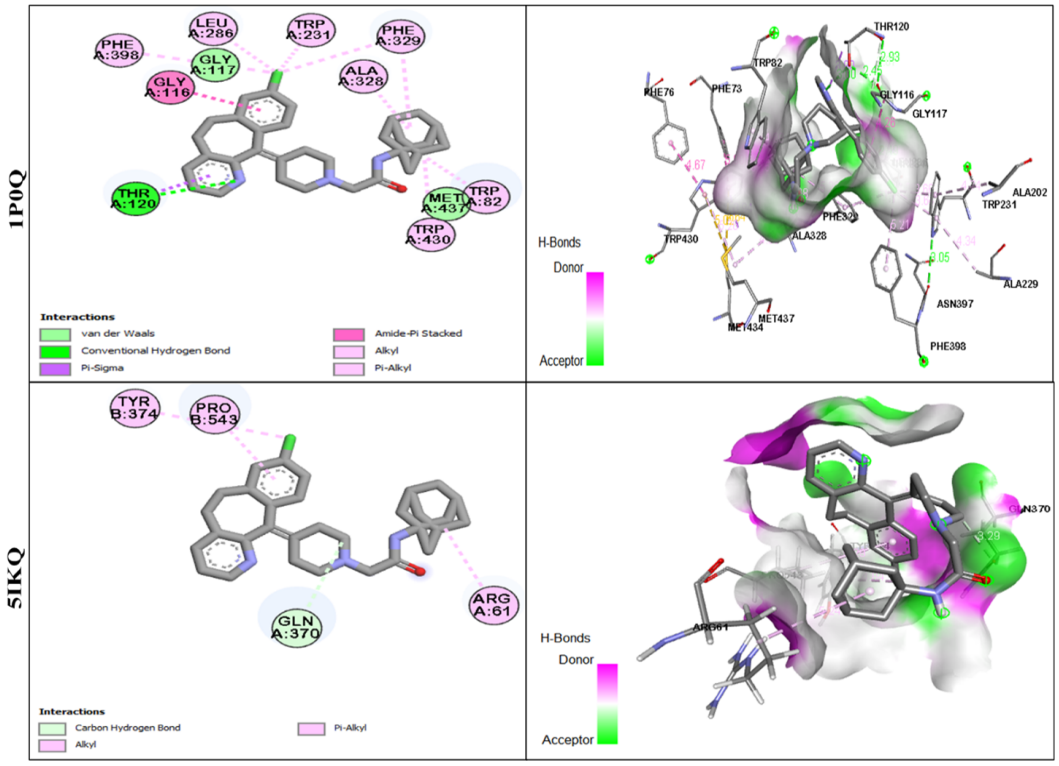

FIGURE 4.21: 2D and 3D molecular docking interaction diagrams of compound 7a within the binding pockets of 1F8U, 1P0Q, 1W50, and 5IKQ. 2D panels depict residue level interactions and 3D panels show the corresponding docked pose within the respective binding site along with the hydrogen bond donor acceptor surface map.

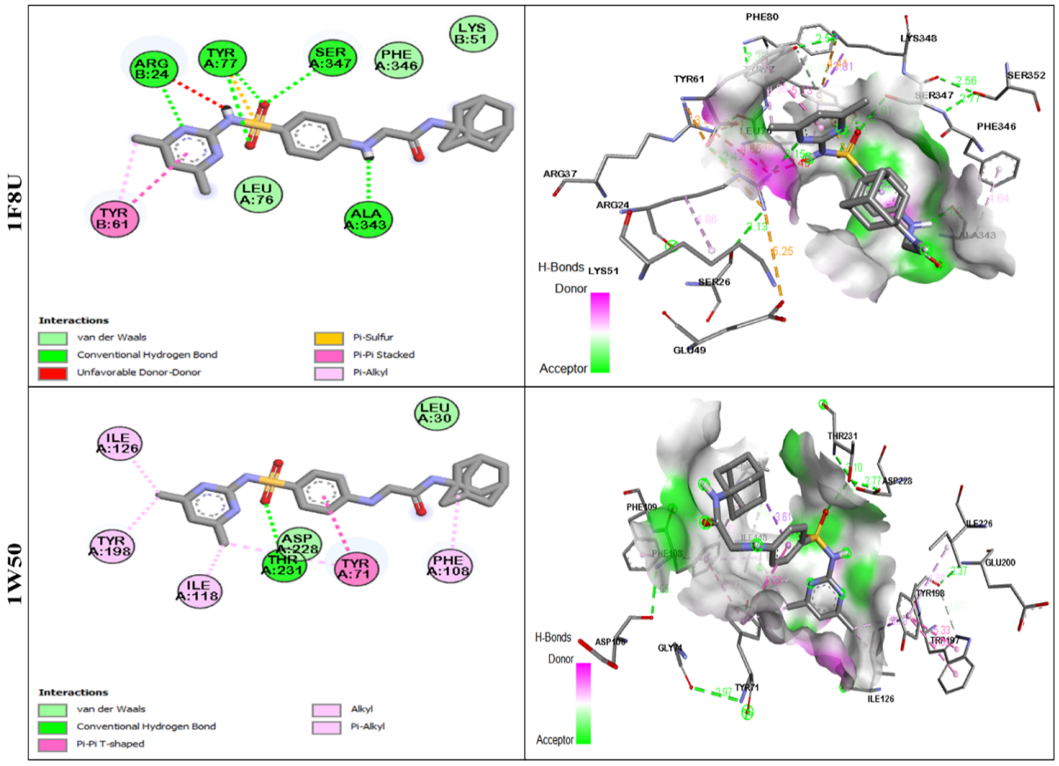

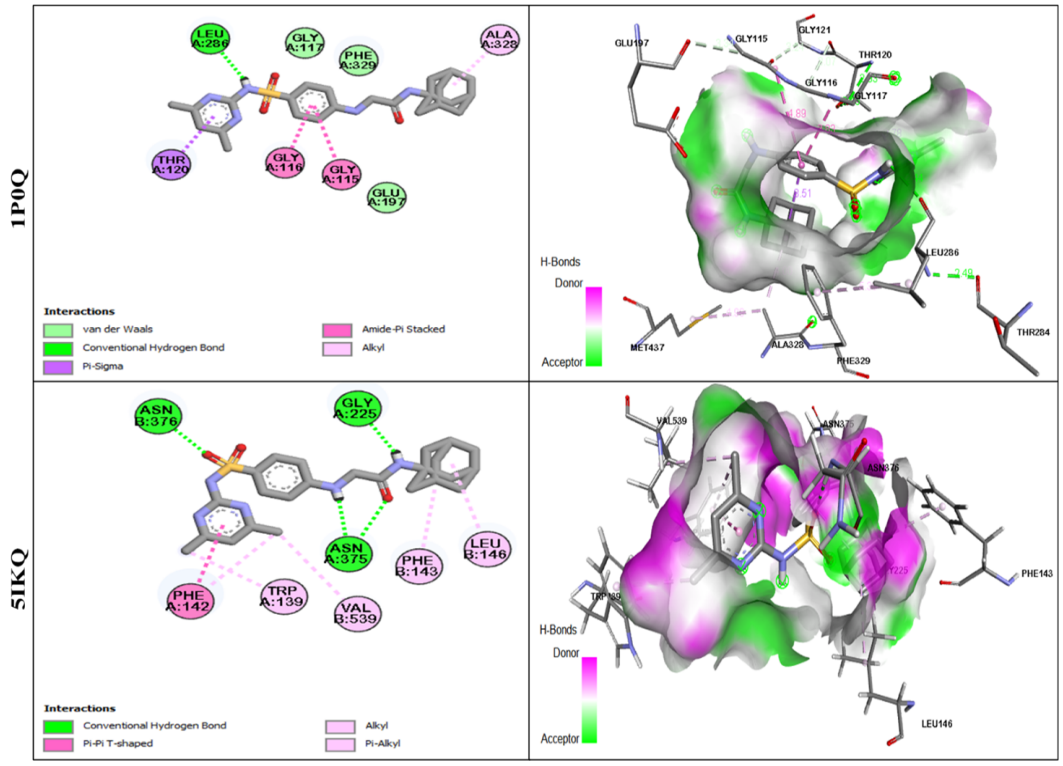

FIGURE 4.22: 2D and 3D molecular docking interaction diagrams of compound 8a within the binding pockets of 1F8U, 1P0Q, 1W50, and 5IKQ. 2D panels depict residue level interactions and 3D panels show the corresponding docked pose within the respective binding site along with the hydrogen bond donor acceptor surface map.

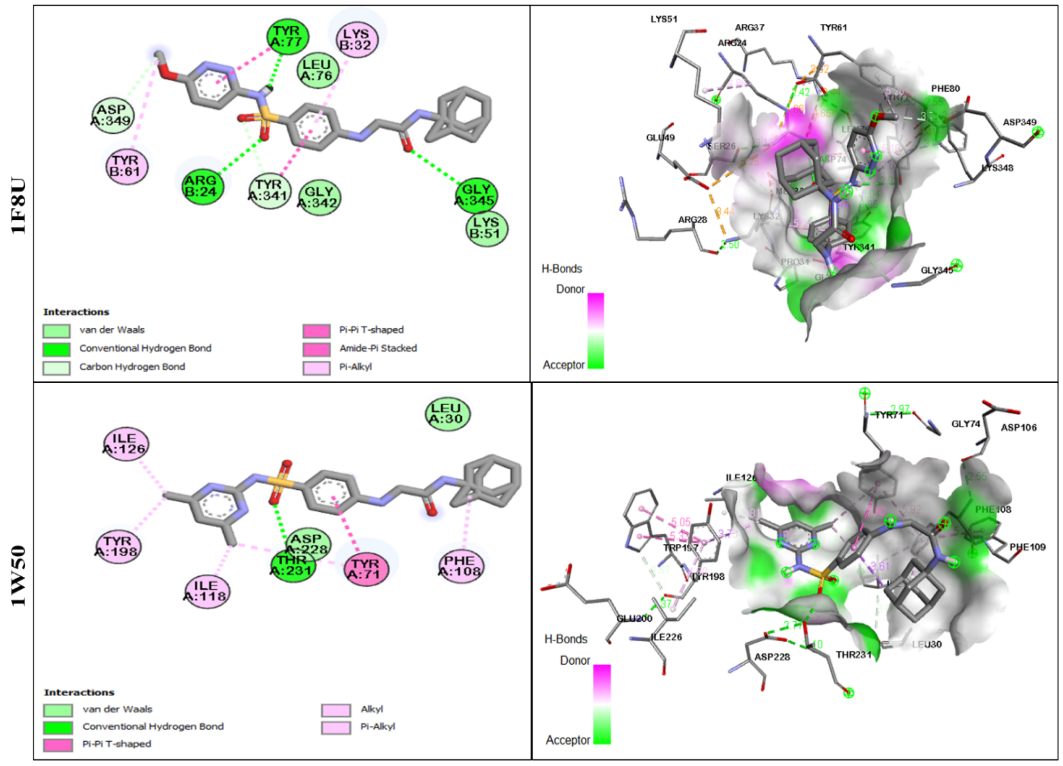

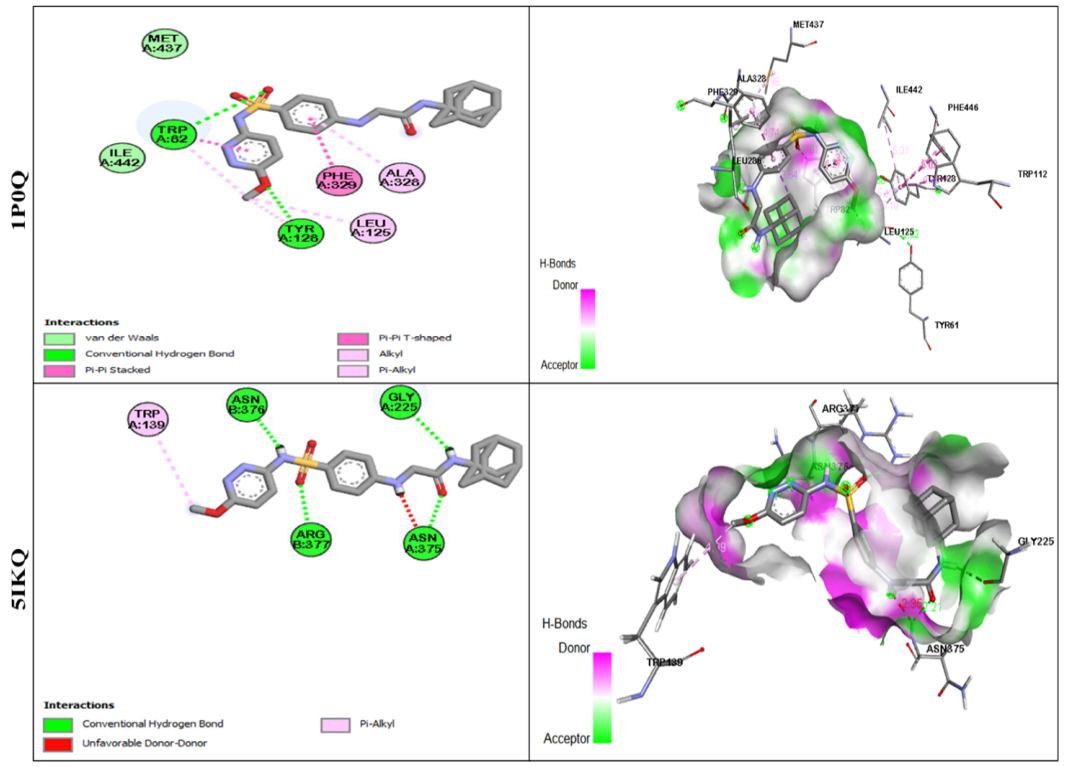

FIGURE 4.23: 2D and 3D molecular docking interaction diagrams of compound 9a within the binding pockets of 1F8U, 1P0Q, 1W50, and 5IKQ. 2D panels depict residue level interactions and 3D panels show the corresponding docked pose within the respective binding site along with the hydrogen bond donor acceptor surface map.

4.5 *In-vivo* Evaluation

4.5.1 Behavioral Evaluation

4.5.1.1 Effect of Test Compound on Spatial Memory Deficit in MWM Test

The effect of test compound 7a on spatial memory was evaluated by using MWM probe trial, that how much time is spent by mice in target quadrant (Figure 4.17). Scopolamine significantly reduced target quadrant retention compared with the normal control group (adjusted $p < 0.001$), indicating impaired spatial memory. Donepezil (5 mg/kg) significantly reversed this deficit. Treatment with the synthesized compound at 1 mg/kg produced a non-significant improvement, whereas

5 mg/kg and 10 mg/kg significantly increased the time spent in the target quadrant compared with the scopolamine-treated group (adjusted $p < 0.001$). The higher doses showed effects comparable to donepezil, indicating a dose-dependent improvement in spatial memory.

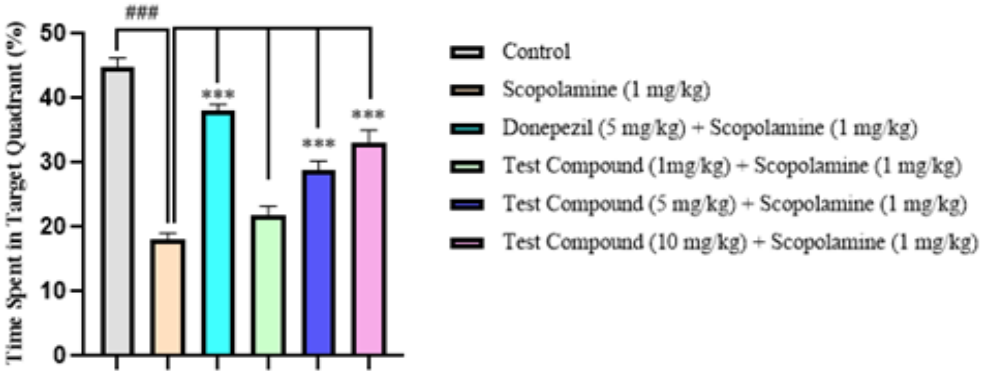

FIGURE 4.24: Effect of test compound 7a on the percentage of time spent in the target quadrant during the probe trial of the MWM test. Groups included control, scopolamine (1 mg/kg), donepezil (5 mg/kg, standard drug) + scopolamine (1 mg/kg), and compound 7a (1, 5, or 10 mg/kg) + scopolamine (1 mg/kg). Data are expressed as mean ± SEM (n = 7/group) and analyzed by one-way ANOVA followed by Tukey's post hoc test. $p < 0.001$ vs. control; ***$p < 0.001$ vs. scopolamine.

4.5.1.2 Effect of Test Compound on Spatial Memory Deficit in Y-Maze Test

The effect of the treatments on spatial working memory was evaluated using the Y-maze spontaneous alternation test. Scopolamine significantly reduced spontaneous alternation compared with the Normal Control group ($p < 0.001$), confirming cognitive impairment, while the Positive Control significantly improved memory performance. Test Group 1 showed no significant improvement compared with the Negative Control. In contrast, Test Groups 2 and 3 significantly increased spontaneous alternation, with Test Group 3 producing the greatest improvement and showing performance comparable to the Positive Control. These results indicate a dose-dependent enhancement of spatial working memory by the test compound.

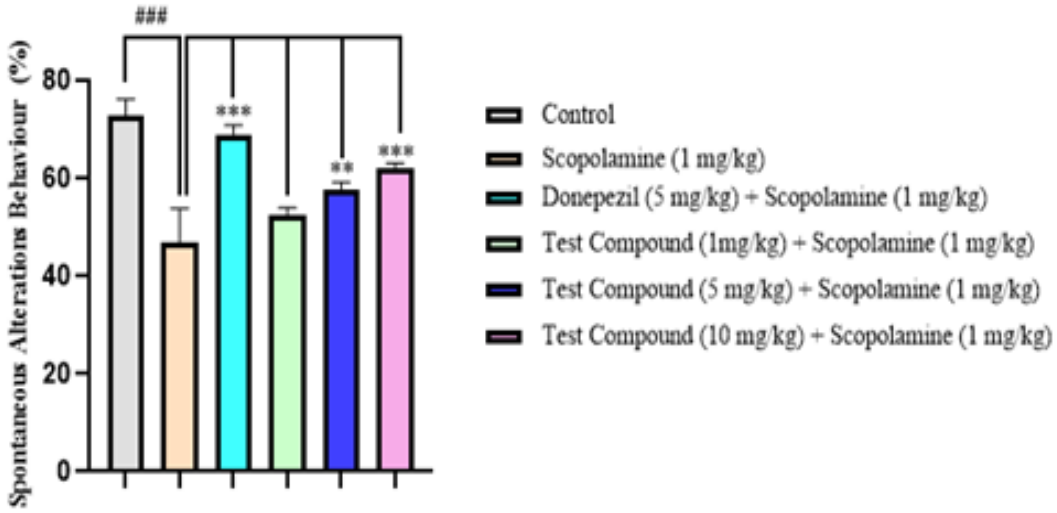

FIGURE 4.25: Effect of test compounds on the percentage of spontaneous alternation behavior in the Y-maze test. Groups included control, scopolamine (1 mg/kg), donepezil (5 mg/kg, standard drug) + scopolamine (1 mg/kg), and compound 7a (1, 5, or 10 mg/kg) + scopolamine (1 mg/kg). Data are expressed as mean ± SEM (n = 6/group) and analyzed by one-way ANOVA followed by Tukey's post hoc test. $p < 0.001$ vs. control; $^{**}p < 0.01$ and $^{***}p < 0.001$ vs. scopolamine.

4.5.1.3 Effect of Test Compound on COX-2 Expression in Hippocampus Assessed by ELISA

The effect of the treatments on hippocampal COX-2 levels was determined by ELISA. Scopolamine significantly increased COX-2 expression compared with the Normal Control group, indicating marked neuroinflammation, whereas the Positive Control restored COX-2 levels close to normal.

Test Group 1 produced a significant reduction in COX-2 levels but remained significantly different from the Normal Control, suggesting partial suppression of inflammation.

In contrast, Test Groups 2 and 3 significantly reduced COX-2 expression, with no significant difference from the Normal or Positive Control groups. Among the treatment groups, Test Group 3 showed the greatest reduction in COX-2 levels, demonstrating efficacy comparable to the Positive Control.

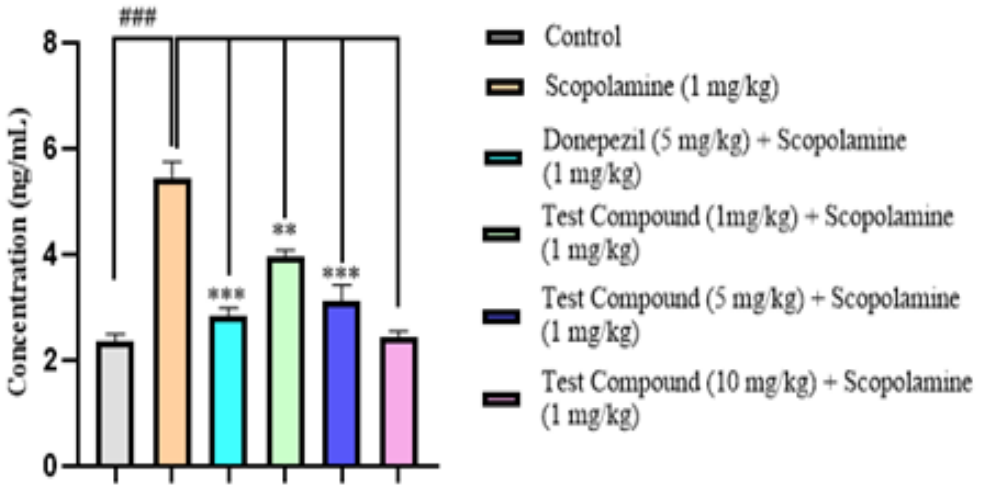

FIGURE 4.26: Groups included control, scopolamine (1 mg/kg), donepezil (5 mg/kg, standard drug) + scopolamine (1 mg/kg), and compound 7a (1, 5, or 10 mg/kg) + scopolamine (1 mg/kg). Data are expressed as mean ± SEM (n = 6/group) and analyzed by one-way ANOVA followed by Tukey's post hoc test. $p < 0.001$ vs. control; ***$p < 0.001$ vs. scopolamine.

4.5.1.4 Effects of Test Compound on Neuronal Survival Assessed by H and E Staining

H and E staining of hippocampal sections showed normal neuronal structure with intact Cornu Ammonis CA1, CA3, and Dentate Gyrus (DG) regions in the Normal Control group.

In contrast, the Scopolamine-treated Negative Control group showed marked neuronal degeneration, including reduced neuronal density, pyknotic cells, vacuolation, and disruption of hippocampal layers. Treatment with Donepezil markedly attenuated these histopathological changes.

The test compound produced dose-dependent neuroprotection, with 1 mg/kg showing partial improvement, 5 mg/kg demonstrating moderate restoration of neuronal architecture, and 10 mg/kg showing near-normal hippocampal morphology comparable to the Positive Control. Overall, the findings indicate that the test compound effectively protected against hippocampal damage caused by scopolamine.

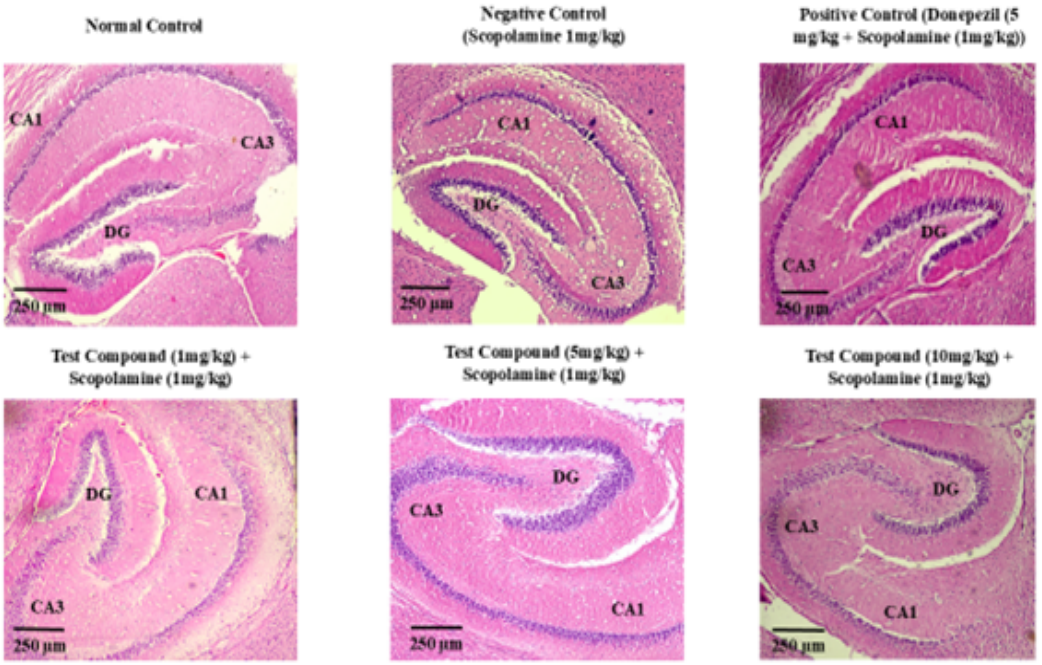

FIGURE 4.27: Effect of test compounds on neuronal survival in the hippocampus assessed by Hematoxylin and Eosin (HE) staining. Panels show normal control, negative control (scopolamine 1 mg/kg), positive control (donepezil 5 mg/kg + scopolamine 1 mg/kg), and compound 7a (1, 5, or 10 mg/kg) + scopolamine (1 mg/kg) groups. Red arrows indicate pyknotic nuclei and black arrows indicate vacuolation in the CA1, CA3, and dentate gyrus (DG) regions. Scale bar = 250 m.

Chapter 5

Discussion

The present study was designed to explore amantadine based Schiff bases and acetylated derivatives (1a–9a) as potential multi-target therapeutic agents for AD. Amantadine was selected as a parent scaffold due to its known central nervous system activity and ability to cross the blood–brain barrier.

Structural modifications were introduced to enhance pharmacological potential, where Schiff base formation introduced an azomethine (–C=N–) linkage to improve receptor interactions [86], while acetylation was employed to modulate lipophilicity and pharmacokinetic behavior [70]. These modifications were done to improve binding affinity towards cholinesterase and amyloid-related targets involved in neurodegeneration.

All synthesized derivatives were evaluated using SwissADME and multiple drug-likeness filters. Most compounds followed Lipinski's rule of five, showing molecular weight $\leq$500 Da, hydrogen bond donors $\leq$5, hydrogen bond acceptors $\leq$10, and logP $\leq$5. Only compound 5a slightly violated this rule with a molecular weight of 502.09 Da and elevated lipophilicity [87]. Veber's rule was followed by all compounds, with topological polar surface area (TPSA) values $\leq$140 Å^2 and rotatable bonds ranging from 2 to 9, indicating favorable oral bioavailability[88].

All compounds had high gastrointestinal absorption, indicating favorable oral uptake potential. BBB permeability analysis revealed that compounds 1a, 2a, 4a,

5a, 6a, and 9a were BBB permeant, whereas compounds 3a, 7a, and 8a were non-permeant. P-glycoprotein analysis showed that compounds 4a, 5a, 6a, and 9a were non-substrates, suggesting improved CNS retention. CYP450 inhibition profiling indicated multiple enzyme interactions, particularly CYP2D6 inhibition in most compounds, along with selective CYP3A4, CYP2C19, and CYP2C9 inhibition in specific derivatives, highlighting potential drug–drug interaction risks [76].

All compounds satisfied Ghose, Egan, Veber, and Muegge drug-likeness filters except compound 5a, which showed multiple violations due to higher molecular weight, lipophilicity, and molar refractivity [89].

Fsp^3 values for all compounds were below 0.42, and consistent with synthetic CNS-active drug space [90, 91]. Lipophilicity analysis showed XLOGP3 values ranging from 2.96 to 4.72 for most compounds, while compound 5a showed significantly higher values up to 6.99, indicating excessive hydrophobicity that may negatively affect solubility and absorption [90].

Solubility prediction using ESOL, Ali, and SILICOS-IT models indicated that most compounds showed moderate aqueous solubility. ESOL Log S values ranged from -3.91 to -7.34. Compounds 1a and 2a showed the highest solubility (-3.91), while compound 5a was poorly soluble (-7.34). Similar trends were observed in Ali and SILICOS-IT models, where compounds 3a and 5a consistently showed reduced solubility, whereas most other derivatives maintained moderate solubility profiles suitable for oral drug development [92].

GHS classification indicated that compounds 1a, 2a, 4a, 6a, and 9a belonged to Class 5 toxicity, compounds 5a and 8a to Class 4, compound 3a to Class 3, and compound 7a to Class 6. Organ toxicity prediction showed that all compounds were non-hepatotoxic, non-nephrotoxic, and non-cardiotoxic. However, respiratory toxicity alerts were observed across all compounds. Neurotoxicity was predicted in most derivatives except 7a and 8a. Carcinogenicity prediction indicated potential risk in compounds 4a, 6a, and 9a, while all compounds were non-mutagenic and non-cytotoxic, suggesting overall genetic safety [93].

Docking against AChE showed that donepezil showed a binding energy of -7.2 kcal/mol. Among the synthesized derivatives, compound 5a showed the highest binding affinity (-8.9 kcal/mol), followed by compound 3a (-8.0 kcal/mol), compound 1a (-7.3 kcal/mol), and compound 7a (-7.2 kcal/mol). Compound 2a (-6.6 kcal/mol), 4a (-6.1 kcal/mol), 6a (-6.7 kcal/mol), 8a (-7.0 kcal/mol), and 9a (-6.4 kcal/mol) showed moderate binding affinities.

Compound 5a formed stabilizing π–sigma and alkyl interactions with LYS B:32, TYR A:341, LEU A:76, and TYR B:61. Compound 3a showed conventional hydrogen bonding, π-cation, π-anion, and π-alkyl interactions with ASP A:400, ARG A:525, LYS A:332, GLU A:396, and ASP A:333. Compound 1a formed hydrogen bonding, carbon–hydrogen bonding, π-anion, and π-alkyl interactions with TYR A:72, SER A:125, ASP A:74, TRP A:86, and TYR A:337.

Compound 7a showed hydrogen bonding, π-sulfur, π–π stacking, and alkyl interactions with ARG B:24, TYR A:77, SER A:347, LYS B:32, ALA A:343, and TYR B:61, while compound 8a interacted with TYR A:77, ARG B:24, GLY A:345, ASP A:349, and TYR B:61 through hydrogen bonding and π–π T-shaped interactions [94].

Docking against BChE showed significantly stronger binding than donepezil (-7.2 kcal/mol). Compound 5a showed the highest binding affinity (-10.9 kcal/mol), followed by compound 7a (-10.4 kcal/mol), compounds 3a and 8a (-10.2 kcal/mol), compound 1a (-8.4 kcal/mol), compound 4a (-8.0 kcal/mol), compound 6a (-8.2 kcal/mol), compound 9a (-8.2 kcal/mol), and compound 2a (-8.0 kcal/mol). Compound 5a formed extensive interactions with THR120, GLY116, PHE398, LEU286, TRP231, PHE329, MET437, TRP430, ALA328, and TRP82, with strong aromatic stacking at TRP82, PHE329, TRP231, and TRP430. Compound 7a interacted with LEU286, THR120, GLY116, ALA328, and GLY117. Compound 8a showed π–π stacking and alkyl interactions with TRP82, TYR128, PHE329, ALA328, and LEU125. Compound 3a interacted with GLY116, THR120, SER198, TRP82, HIS438, PHE329, LEU286, and ALA328, notably involving catalytic residues SER198 and HIS438. Compound 9a showed interactions with SER198, LEU286,

THR120, TRP231, GLY116, PHE329, and HIS438 but with comparatively weaker binding [94].

Docking against BACE-1 showed that compound 5a showed the strongest binding (-8.9 kcal/mol), followed by compounds 7a and 8a (-8.1 kcal/mol), compound 3a (-7.8 kcal/mol), and compound 4a (-7.0 kcal/mol), while others ranged from -6.5 to -6.9 kcal/mol. Compound 5a interacted with SER35, VAL332, and TYR198, while compound 3a formed interactions with THR231, GLY230, TYR198, VAL332, LEU30, and ASP32. Compound 7a interacted with THR231, TYR71, ILE126, TYR198, PHE108, and ASP32, whereas compound 8a was stabilized by ASP32, LYS107, THR239, GLY230, TYR71, and PHE108. Compound 9a showed weaker binding involving TYR71, ASP32, PHE108, and TYR198 [94].

The results from the in-silico and in-vitro phases of the present study provided an initial and pharmacological basis for the potential neuroprotective effects of the test compound. Molecular docking and computational analysis provided favorable binding interactions with key target proteins implicated in neurodegenerative processes, particularly those associated with cholinergic dysfunction and cognitive decline. These results were further supported by *in-vitro* assessments, which showed acceptable biological activity. Therefore, to validate and extend these findings under physiologically relevant conditions, *in-vivo* behavioral studies were conducted using well-established animal models of cognitive impairment.

In scopolamine-induced Alzheimer's models, significant cognitive impairment was observed in both MWM and Y-maze tests. Donepezil significantly restored performance. In the Morris Water Maze, 1 mg/kg showed minimal improvement, while 5 mg/kg and 10 mg/kg doses significantly improved target quadrant time, with the highest dose comparable to donepezil. In the Y-maze, test group 3 (10 mg/kg) showed the highest spontaneous alternation, significantly greater than lower doses and comparable to the positive control [80–82]. Scopolamine significantly increased COX-2 expression, confirming neuroinflammation. Donepezil and higher doses of the test compound significantly reduced COX-2 levels. Test groups 2 and 3 restored COX-2 close to normal control levels, with test group 3 showing

the strongest anti-inflammatory effect [84]. Hippocampal sections showed severe degeneration in scopolamine-treated animals, including neuronal loss and pyknosis in CA1, CA3, and DG regions. Donepezil provided partial protection. The 1 mg/kg dose showed mild improvement, while 5 mg/kg significantly restored neuronal architecture. The 10 mg/kg dose nearly normalized hippocampal structure, closely resembling control animals [85].

Among all synthesized derivatives, compound 7a was identified as the most balanced and most suitable lead candidate, demonstrating strong binding affinity across all targets AChE, BChE, BACE-1 with binding energies -7.2 kcal/mol, -10.4 kcal/mol, -8.1 kcal/mol respectively, along with a more favorable pharmacokinetic and safety profile.

Notably, compound 7a showed a Class 6 GHS safety classification LD_{50} of 25,000 mg/kg, absence of predicted neurotoxicity, no CYP3A4 inhibition, acceptable blood–brain barrier permeability, and overall balanced physicochemical properties. These characteristics collectively indicate that compound 7a provides an optimal balance between efficacy, safety, and drug-likeness compared to other derivatives.

The interpretation of the present findings is further supported by comparison with the established pharmacological characteristics of the parent compound, amantadine. Amantadine functions primarily as a low-to-moderate affinity, uncompetitive NMDA receptor antagonist, a mechanism it shares with memantine, which is structurally a dimethylated derivative of amantadine [7]. This mechanism is particularly relevant to AD, in which dysregulated glutamatergic neurotransmission and NMDA receptor-mediated excitotoxicity have been implicated in neuronal dysfunction and cognitive decline [8]. Amantadine is also capable of entering the brain through carrier-mediated transport mechanisms at the blood–brain barrier, supporting its suitability as a CNS-directed parent molecule [9]. However, its established pharmacological profile is relatively narrow in comparison with the multiple pathological mechanisms involved in AD. Therefore, the use of amantadine as a starting scaffold provides an opportunity to retain its favorable CNS characteristics while exploring structural modifications that may introduce additional

biological activities. Previous literature describing neuroprotective and cognition-related effects of amino-adamantanes further supports the rationale for investigating amantadine-derived compounds in neurodegenerative disorders [10, 11].

Overall, the results indicate that the synthesized derivatives showed strong multi-target neuroprotective potential, with compound 7a standing out as the most balanced candidate for further exploration and advanced preclinical evaluation in AD. Therefore the present study provides a comprehensive multi-level evaluation of newly designed amantadine-based Schiff base and acetylated derivatives (1a–9a) for their potential application in AD.

Chapter 6

Conclusion

In the present study a series of novel amantadine-based Schiff base and acetylated derivatives (1a–9a) were designed, synthesized, and evaluated as potential multi-target candidates for the management of AD. A total of nine derivatives were successfully synthesized and characterized using spectroscopic techniques, confirming the formation of the intended chemical structures. *In-silico* evaluation showed that most compounds had favorable drug-likeness properties in accordance with Lipinski, Veber, Egan, Ghose, and Muegge criteria with acceptable pharmacokinetic behavior, including gastrointestinal absorption and BBB permeability.

Molecular docking studies showed strong binding affinities against AChE, BChE, and BACE-1 with several compounds showing stronger interactions. ADMET and toxicity profiling indicated that while most compounds showed acceptable safety and pharmacokinetic profiles certain derivatives showed limitations in solubility, lipophilicity, and cytochrome P450 interactions. Importantly, compound 7a showed the most balanced overall profile, combining strong multi-target binding affinity with favorable pharmacokinetic properties, low predicted toxicity, absence of neurotoxicity, and acceptable CNS permeability, making it the most suitable lead candidate among the series. The *in-vivo* studies using scopolamine-induced cognitive impairment models MWM and Y-maze tests, which further validated the computational studies. The test compounds produced significant dose-dependent

improvements in learning and memory, with higher doses restoring cognitive performance comparable to donepezil. Biochemical analysis showed significant reduction in COX-2 expression, while histopathological evaluation confirmed preservation of hippocampal structure, indicating neuroprotective effects and neuroinflammation. Overall, the integrated results from computational, biochemical, and behavioral studies shows that structural modification of amantadine can yield biologically active derivatives with multi-target neuroprotective potential. Among the synthesized compounds, compound 7a demonstrated the most favorable balance between efficacy, safety, and drug-likeness, supporting its selection as a lead candidate for further development in AD therapy.

Bibliography

[1] S. Sinha and D. Vohora, "Drug discovery and development: An overview," *Pharmaceutical Medicine and Translational Clinical Research*, pp. 19–32, 2018.

[2] S. M. Paul and et al., "How to improve r&d productivity: The pharmaceutical industry's grand challenge," *Nature Reviews Drug Discovery*, vol. 9, no. 3, pp. 203–214, 2010.

[3] J. P. Hughes and et al., "Principles of early drug discovery," *British Journal of Pharmacology*, vol. 162, no. 6, pp. 1239–1249, 2011.

[4] O. J. Wouters, M. McKee, and J. Luyten, "Estimated research and development investment needed to bring a new medicine to market, 2009–2018," *JAMA*, vol. 323, no. 9, pp. 844–853, 2020.

[5] E. Lionta and et al., "Structure-based virtual screening for drug discovery: Principles, applications and recent advances," *Current Topics in Medicinal Chemistry*, vol. 14, no. 16, pp. 1923–1938, 2014.

[6] A. Lavecchia, "Machine-learning approaches in drug discovery: Methods and applications," *Drug Discovery Today*, vol. 20, no. 3, pp. 318–331, 2015.

[7] J. Vamathevan and et al., "Applications of machine learning in drug discovery and development," *Nature Reviews Drug Discovery*, vol. 18, no. 6, pp. 463–477, 2019.

[8] A. Zhavoronkov, "Artificial intelligence for drug discovery, biomarker development, and generation of novel chemistry," *Molecular Pharmaceutics*, vol. 15, no. 10, pp. 4311–4313, 2018.

[9] M. Békés, D. R. Langley, and C. M. Crews, "Protac targeted protein degraders: The past is prologue," *Nature Reviews Drug Discovery*, vol. 21, no. 3, pp. 181–200, 2022.

[10] M. Schapira and et al., "Targeted protein degradation: Expanding the toolbox," *Nature Reviews Drug Discovery*, vol. 18, no. 12, pp. 949–963, 2019.

[11] J. Vamathevan and et al., "Applications of machine learning in drug discovery and development," *Nature Reviews Drug Discovery*, vol. 18, no. 6, pp. 463–477, 2019.

[12] J. Cummings and et al., "Alzheimer's disease drug development pipeline: 2021," *Alzheimer's & Dementia: Translational Research & Clinical Interventions*, vol. 7, no. 1, p. e12179, 2021.

[13] O. Rascol, M. Fabbri, and W. Poewe, "Amantadine in the treatment of parkinson's disease and other movement disorders," *The Lancet Neurology*, vol. 20, no. 12, pp. 1048–1056, 2021.

[14] A. Mata-Bermudez and et al., "Amantadine prevented hypersensitivity and decreased oxidative stress by nmda receptor antagonism after spinal cord injury in rats," *European Journal of Pain*, vol. 25, no. 8, pp. 1839–1851, 2021.

[15] J. Kirschbaum, "Amantadine," in *Analytical Profiles of Drug Substances*, pp. 1–36, Elsevier, 1983.

[16] I. F. M. Raupp-Barcaro and et al., "Involvement of dopamine d2 and glutamate nmda receptors in the antidepressant-like effect of amantadine in mice," *Behavioural Brain Research*, vol. 413, p. 113443, 2021.

[17] B. Ossola and et al., "Amantadine protects dopamine neurons by a dual action: Reducing activation of microglia and inducing expression of gdnf in astroglia," *Neuropharmacology*, vol. 61, no. 4, pp. 574–582, 2011.

[18] T. Suzuki and et al., "Involvement of a proton-coupled organic cation antiporter in the blood–brain barrier transport of amantadine," *Biopharmaceutics & Drug Disposition*, vol. 37, no. 6, pp. 323–335, 2016.

[19] T. A. Blanpied, R. J. Clarke, and J. W. Johnson, "Amantadine inhibits nmda receptors by accelerating channel closure during channel block," *Journal of Neuroscience*, vol. 25, no. 13, pp. 3312–3322, 2005.

[20] Y. E. Kadernani and et al., "Adamantane amine derivatives as dual acting nmda receptor and voltage-gated calcium channel inhibitors for neuroprotection," *MedChemComm*, vol. 5, no. 11, pp. 1678–1684, 2014.

[21] A. Ahmed and et al., "Exploring amantadine derivatives as urease inhibitors: Molecular docking and structure–activity relationship (sar) studies," *Molecules*, vol. 26, no. 23, p. 7150, 2021.

[22] D. S. Knopman and et al., "Alzheimer disease," *Nature Reviews Disease Primers*, vol. 7, no. 1, p. 33, 2021.

[23] P. Scheltens and et al., "Alzheimer's disease," *The Lancet*, vol. 397, no. 10284, pp. 1577–1590, 2021.

[24] C. R. Jack Jr. and et al., "Nia-aa research framework: Toward a biological definition of alzheimer's disease," *Alzheimer's & Dementia*, vol. 14, no. 4, pp. 535–562, 2018.

[25] M. A. DeTure and D. W. Dickson, "The neuropathological diagnosis of alzheimer's disease," *Molecular Neurodegeneration*, vol. 14, no. 1, p. 32, 2019.

[26] Z. Breijyeh and R. Karaman, "Comprehensive review on alzheimer's disease: Causes and treatment," *Molecules*, vol. 25, no. 24, p. 5789, 2020.

[27] J. M. Long and D. M. Holtzman, "Alzheimer disease: An update on pathobiology and treatment strategies," *Cell*, vol. 179, no. 2, pp. 312–339, 2019.

[28] L. C. Dos Santos Picanco and et al., "Alzheimer's disease: A review from the pathophysiology to diagnosis, new perspectives for pharmacological treatment," *Current Medicinal Chemistry*, vol. 25, no. 26, pp. 3141–3159, 2018.

[29] A. Atri, "The alzheimer's disease clinical spectrum: Diagnosis and management," *Medical Clinics of North America*, vol. 103, no. 2, pp. 263–293, 2019.

[30] S. Safiri and et al., "Alzheimer's disease: A comprehensive review of epidemiology, risk factors, symptoms, diagnosis, management, caregiving, advanced treatments and associated challenges," *Frontiers in Medicine*, vol. 11, p. 1474043, 2024.

[31] E. Nichols and et al., "Estimation of the global prevalence of dementia in 2019 and forecasted prevalence in 2050: An analysis for the global burden of disease study 2019," *The Lancet Public Health*, vol. 7, no. 2, pp. e105–e125, 2022.

[32] C. A. Lane, J. Hardy, and J. M. Schott, "Alzheimer's disease," *European Journal of Neurology*, vol. 25, no. 1, pp. 59–70, 2018.

[33] D. J. Selkoe and J. Hardy, "The amyloid hypothesis of alzheimer's disease at 25 years," *EMBO Molecular Medicine*, vol. 8, no. 6, pp. 595–608, 2016.

[34] M. A. Busche and B. T. Hyman, "Synergy between amyloid-β and tau in alzheimer's disease," *Nature Neuroscience*, vol. 23, no. 10, pp. 1183–1193, 2020.

[35] M. T. Heneka, D. T. Golenbock, and E. Latz, "Innate immunity in alzheimer's disease," *Nature Immunology*, vol. 16, no. 3, pp. 229–236, 2015.

[36] X.-X. Zhang and et al., "The epidemiology of alzheimer's disease modifiable risk factors and prevention," *The Journal of Prevention of Alzheimer's Disease*, vol. 8, no. 3, pp. 313–321, 2021.

[37] J. M. Ranson and et al., "Modifiable risk factors for dementia and dementia risk profiling. a user manual for brain health services—part 2 of 6," *Alzheimer's Research & Therapy*, vol. 13, no. 1, p. 169, 2021.

[38] Y.-S. Liu and et al., "Research progress on the etiology and pathogenesis of alzheimer's disease from the perspective of chronic stress," *Aging and Disease*, vol. 14, no. 4, p. 1292, 2023.

[39] J. Zhang and et al., "Pathological mechanisms and treatment progression of alzheimer's disease," *European Journal of Medical Research*, vol. 30, no. 1, p. 625, 2025.

[40] F. Khan and H. Qiu, "Amyloid-β: A potential mediator of aging-related vascular pathologies," *Vascular Pharmacology*, vol. 152, p. 107213, 2023.

[41] M. K. Singh and et al., "Comprehensive overview of alzheimer's disease: Etiological insights and degradation strategies," *International Journal of Molecular Sciences*, vol. 25, no. 13, p. 6901, 2024.

[42] X.-H. Qian and et al., "Inflammatory pathways in alzheimer's disease mediated by gut microbiota," *Ageing Research Reviews*, vol. 68, p. 101317, 2021.

[43] D. Chu and F. Liu, "Pathological changes of tau related to alzheimer's disease," *ACS Chemical Neuroscience*, vol. 10, no. 2, pp. 931–944, 2018.

[44] S. Manoharan and et al., "The role of reactive oxygen species in the pathogenesis of alzheimer's disease, parkinson's disease, and huntington's disease: A mini review," *Oxidative Medicine and Cellular Longevity*, vol. 2016, no. 1, p. 8590578, 2016.

[45] Y.-J. Cheng, C.-H. Lin, and H.-Y. Lane, "Involvement of cholinergic, adrenergic, and glutamatergic network modulation with cognitive dysfunction in alzheimer's disease," *International Journal of Molecular Sciences*, vol. 22, no. 5, p. 2283, 2021.

[46] S. B. Kim and et al., "The neuroprotective effects of dendropanax morbifera water extract on scopolamine-induced memory impairment in mice," *International Journal of Molecular Sciences*, vol. 24, no. 22, p. 16444, 2023.

[47] O. J. Olajide and et al., "Hippocampal degeneration and behavioral impairment during alzheimer-like pathogenesis involves glutamate excitotoxicity," *Journal of Molecular Neuroscience*, vol. 71, no. 6, pp. 1205–1220, 2021.

[48] L. Ning and et al., "Ampa receptors in alzheimer disease: Pathological changes and potential therapeutic targets," *Journal of Neuropathology & Experimental Neurology*, vol. 83, no. 11, pp. 895–906, 2024.

[49] K. Zhang and et al., "Nmda receptors in neurodegenerative diseases: Mechanisms and emerging therapeutic strategies," *Frontiers in Aging Neuroscience*, vol. 17, 2025.

[50] Q. Deng and et al., "Microglia and astrocytes in alzheimer's disease: Significance and summary of recent advances," *Aging and Disease*, vol. 15, no. 4, p. 1537, 2024.

[51] W. Liu and et al., "The role of n-methyl-d-aspartate glutamate receptors in alzheimer's disease: From pathophysiology to therapeutic approaches," *Progress in Neurobiology*, vol. 231, p. 102534, 2023.

[52] C. M. Da Silva and et al., "Schiff bases: A short review of their antimicrobial activities," *Journal of Advanced Research*, vol. 2, no. 1, pp. 1–8, 2011.

[53] E. Raczuk and et al., "Different schiff bases—structure, importance and classification," *Molecules*, vol. 27, no. 3, p. 787, 2022.

[54] X.-D. Jin and et al., "Synthesis, characterization, and crystal structure of two zinc (ii) complexes with a schiff base derived from amantadine," *Journal of Coordination Chemistry*, vol. 66, no. 22, pp. 3970–3978, 2013.

[55] X.-D. Jin and et al., "Synthesis, characterization, crystal structure, and electrochemical properties of three copper (ii) complexes with 3,5-dihalosalicylaldehyde schiff bases derived from amantadine," *Journal of Coordination Chemistry*, vol. 72, no. 14, pp. 2295–2309, 2019.

[56] D. Majumdar and et al., "Two adamantan-1-amine-based scaffolds: Synthesis, crystallographic synthons, td/dft calculations, in-depth molecular docking/adme/t simulations, and shedding light on antibacterial/fungal activities," *Results in Chemistry*, vol. 6, p. 101228, 2023.

[57] A. Ajaz and et al., "Synthesis of an amantadine-based novel schiff base and its transition metal complexes as potential alp, α-amylase, and α-glucosidase inhibitors," *RSC Advances*, vol. 13, no. 5, pp. 2756–2767, 2023.

[58] P. A. Channar and et al., "Extending the scope of amantadine drug by incorporation of phenolic azo schiff bases as potent selective inhibitors of carbonic anhydrase ii, drug-likeness and binding analysis," *Chemical Biology & Drug Design*, vol. 92, no. 3, pp. 1692–1698, 2018.

[59] M. S. Kostić and V. M. Leovac, "Complexes of adamantane-derived schiff bases," in *Advances in Analytical and Coordination Chemistry—Applications and Innovations*, IntechOpen, 2024.

[60] Z. Yasmeen and et al., "Molecular docking, derivatization, characterization and biological assays of amantadine," *Future Medicinal Chemistry*, vol. 16, no. 18, pp. 1853–1863, 2024.

[61] A. Ajaz and et al., "Synthesis, characterization and antidiabetic studies of novel amantadine-derived schiff base (ahb) and its zn (ii), co (ii), cr (iii) and vo (iv) complexes," *RSC Advances*, vol. 15, no. 23, pp. 18752–18765, 2025.

[62] Q. Yang and et al., "Synthesis, characterization, and antibacterial activity of two zinc (ii) complexes with schiff bases from halogenated salicylaldehyde and amantadine," *Russian Journal of Coordination Chemistry*, vol. 40, no. 9, pp. 634–642, 2014.

[63] Z. Wang and et al., "Spectroscopic analyses on interaction of amantadine-salicylaldehyde, amantadine-5-chloro-salicylaldehyde and amantadine-o-vanillin schiff bases with bovine serum albumin (bsa)," *Spectrochimica Acta Part A: Molecular and Biomolecular Spectroscopy*, vol. 83, no. 1, pp. 511–517, 2011.

[64] X. Jin and et al., "Synthesis, characterization, crystal structure, and electrochemical property of copper (ii) complexes with schiff bases derived from 5-halogenated salicylaldehyde and amantadine," *Russian Journal of Coordination Chemistry*, vol. 43, no. 11, pp. 787–794, 2017.

[65] X. Jin and et al., "Synthesis, crystal structure, and magnetic property of four manganese (ii) complexes with bulky schiff bases derived from amantadine and rimantadine," *Russian Journal of Coordination Chemistry*, vol. 45, no. 3, pp. 230–237, 2019.

[66] B. Balaji and N. Dalal, "An expedient and rapid green chemical synthesis of n-chloroacetanilides and amides using acid chlorides under metal-free neutral conditions," *Green Chemistry Letters and Reviews*, vol. 11, no. 4, pp. 552–558, 2018.

[67] D. Liu and et al., "Synthesis and antiviral activity of n-adamantyl-2-amino (or 2-phenoxy)-acylamides," *Chemical Research in Chinese Universities*, vol. 29, no. 4, pp. 706–709, 2013.

[68] O. K. Onajole and et al., "Sq109 analogues as potential antimicrobial candidates," *Medicinal Chemistry Research*, vol. 20, no. 8, pp. 1394–1401, 2011.

[69] Z. Meng and et al., "Design, synthesis, and biological activity of amide based on isoquinolinium salts," *Russian Journal of General Chemistry*, vol. 95, no. 2, pp. 518–524, 2025.

[70] J. G. Wise and et al., "Optimizing targeted inhibitors of p-glycoprotein using computational and structure-guided approaches," *Journal of Medicinal Chemistry*, vol. 62, no. 23, pp. 10645–10663, 2019.

[71] D. B. Kitchen and et al., "Docking and scoring in virtual screening for drug discovery: Methods and applications," *Nature Reviews Drug Discovery*, vol. 3, no. 11, pp. 935–949, 2004.

[72] J. Buannata, B. Wijianto, and I. Arief, "Molecular docking study of modified isoniazid compounds on mycolic acid synthase in the cell wall of mycobacterium tuberculosis," *Acta Chimica Asiana*, vol. 7, no. 2, pp. 471–477, 2024.

[73] O. Trott and A. J. Olson, "Autodock vina: Improving the speed and accuracy of docking with a new scoring function, efficient optimization, and multithreading," *Journal of Computational Chemistry*, vol. 31, no. 2, pp. 455–461, 2010.

[74] U. Baroroh and et al., "Molecular interaction analysis and visualization of protein-ligand docking using biovia discovery studio visualizer," *Indonesian Journal of Computational Biology*, vol. 2, no. 1, pp. 22–30, 2023.

[75] A. Daina and V. Zoete, "A boiled-egg to predict gastrointestinal absorption and brain penetration of small molecules," *ChemMedChem*, vol. 11, no. 11, pp. 1117–1121, 2016.

[76] A. Daina, O. Michielin, and V. Zoete, "Swissadme: A free web tool to evaluate pharmacokinetics, drug-likeness and medicinal chemistry friendliness of small molecules," *Scientific Reports*, vol. 7, no. 1, p. 42717, 2017.

[77] P. Banerjee and et al., "Protox-ii: A webserver for the prediction of toxicity of chemicals," *Nucleic Acids Research*, vol. 46, no. W1, pp. W257–W263, 2018.

[78] H. Dong and et al., "Effects of donepezil on amyloid-beta and synapse density in the tg2576 mouse model of alzheimer's disease," *Brain Research*, vol. 1303, pp. 169–178, 2009.

[79] S. Lee and et al., "Sulforaphane alleviates scopolamine-induced memory impairment in mice," *Pharmacological Research*, vol. 85, pp. 23–32, 2014.

[80] K. Bromley-Brits, Y. Deng, and W. Song, "Morris water maze test for learning and memory deficits in alzheimer's disease model mice," *Journal of Visualized Experiments*, no. 53, p. 2920, 2011.

[81] Z. Syed and et al., "Pharmacological mechanism of xanthoangelol underlying nrf-2/trpv1 and anti-apoptotic pathway against scopolamine-induced amnesia in mice," *Biomedicine & Pharmacotherapy*, vol. 150, p. 113073, 2022.

[82] H. Pei and et al., "Dihydromyricetin suppresses inflammatory injury in microglial cells to improve neurological behaviors of alzheimer's disease mice via

the tlr4/md2 signal," *International Immunopharmacology*, vol. 118, p. 110037, 2023.

[83] A.-K. Kraeuter, P. C. Guest, and Z. Sarnyai, "The y-maze for assessment of spatial working and reference memory in mice," in *Pre-Clinical Models: Techniques and Protocols*, pp. 105–111, Springer, 2018.

[84] S. Saral and et al., "Apelin-13 activates the hippocampal bdnf/trkb signaling pathway and suppresses neuroinflammation in male rats with cisplatin-induced cognitive dysfunction," *Behavioural Brain Research*, vol. 408, p. 113290, 2021.

[85] M. Shreejha and et al., "Analysis of histological features of the cerebral cortex and hippocampus of albino rats using haematoxylin & eosin stain: An observational study," *Journal of Pharmaceutical Research International*, vol. 33, no. 59A, pp. 53–64, 2021.

[86] K. Singh, M. S. Barwa, and P. Tyagi, "Synthesis, characterization and biological studies of co (ii), ni (ii), cu (ii) and zn (ii) complexes with bidentate schiff bases derived by heterocyclic ketone," *European Journal of Medicinal Chemistry*, vol. 41, no. 1, pp. 147–153, 2006.

[87] C. A. Lipinski, "Chapter 11: Filtering in drug discovery," *Annual Reports in Computational Chemistry*, vol. 1, pp. 155–168, 2005.

[88] C. A. Lipinski and et al., "Experimental and computational approaches to estimate solubility and permeability in drug discovery and development settings," *Advanced Drug Delivery Reviews*, vol. 23, no. 1–3, pp. 3–25, 1997.

[89] S. J. Teague and et al., "The design of leadlike combinatorial libraries," *Angewandte Chemie International Edition*, vol. 38, no. 24, pp. 3743–3748, 1999.

[90] A. Daina, O. Michielin, and V. Zoete, "ilogp: A simple, robust, and efficient description of n-octanol/water partition coefficient for drug design using the gb/sa approach," *Journal of Chemical Information and Modeling*, vol. 54, no. 12, pp. 3284–3301, 2014.

[91] C.-Y. Jia and et al., "A drug-likeness toolbox facilitates admet study in drug discovery," *Drug Discovery Today*, vol. 25, no. 1, pp. 248–258, 2020.

[92] Organisation for Economic Co-operation and Development, "Oecd guideline 420: Guideline for the testing of chemicals: Acute oral toxicity—fixed dose procedure," 2001.

[93] P. Banerjee and et al., "Protox 3.0: A webserver for the prediction of toxicity of chemicals," *Nucleic Acids Research*, vol. 52, no. W1, pp. W513–W520, 2024.

[94] P. F. Ayodele and et al., "Illustrated procedure to perform molecular docking using pyrx and biovia discovery studio visualizer: A case study of 10kt with atropine," *Progress in Drug Discovery & Biomedical Science*, vol. 6, no. 1, 2023.